Design Optimization and Plan Optimization for Particle Beam Therapy Systems

Yusuke Sakamoto

Design Optimization and Plan Optimization for Particle Beam Therapy Systems

Yusuke Sakamoto

Department of Mechanical Engineering and Science

Graduate School of Engineering

Kyoto University

I would like to dedicate this dissertation to my loving wife and son . . .

Acknowledgements

Yusuke Sakamoto
January, 2024

Table of contents

Chapter 1

General Introduction: Particle beam therapy system

1.1 Particle beam cancer therapy

For these decade, the numbers of those who are affected to and die of cancer are gradually increasing [1–5]. Currently there are various types of treatment for cancer patients, as shown in Fig. 1.1. Surgery and chemotherapy are the most popular options which have very high effectiveness and grate results as cancer treatment, while these method are basically invasive to the patients. Surgery physically removes not only the cancer tumor itself but also the surrounding volume to avoid metastasis, thus there are some disadvantages that there remains scar in the patient body or the functions of some organs are not completely recovered. Since chemotherapy also affects not only the tumor but also every healthy tissues in the body, it has negative side effects such as nausea, vomiting, diarrhea and hair loss. On the other hand, radiation therapy [6] can give a cancer treatment because of its ionization effect without physical nor chemical harm to the patient body. Nowadays, technology enables very high precision control of beam irradiation in which enough amount of beam is delivered to the timor while keeping the minimum affection to healthy tissues. Besides, radiation therapy sometimes enables the daily-visit treatment without admission to the hospital, which can enhance the quality of life (QOL) of the patient. Radiation therapy can further be classified into several types by the kind of beam and the way to be irradiated.

Among various types of radiation therapy of cancer, particle beam therapy [7–11] is taking an increasing interest as a cancer treatment method compared with other typical
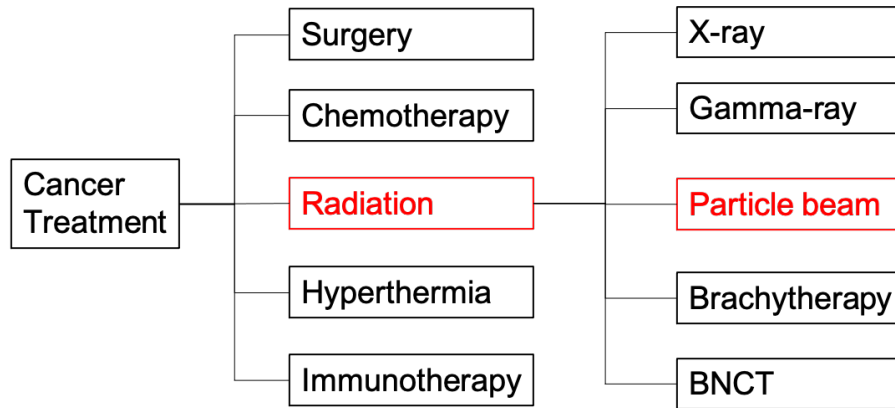
Fig. 1.1 Classifications of Cancer therapy and radiation therapy.

choices. With particle beam therapy, externally irradiated particle beam destroys the cancer cells with its ionization effect, as similar to other radiation therapy. The idea of using accelerated proton for cancer treatment was the first proposed by Wilson [12] in 1946 and the first 30 patients were treated from 1954 to 1957 at Lawrence Berkeley National Laboratory (LBL), California, US [13]. According to Particle Therapy Co-Operative Group (PTCOG) [14], more than 100 facilities of particle therapy had been constructed and more than 360, 000 cancer patients had been treated by particle therapy until 2022. Compared with X-ray radiation therapy, particle beam therapy is considered to be much less-invasive, as shown in Fig. 1.2 because of its very attractive physics properties as follows. First of all, the dose distribution in the depth direction when it is transported within the human body shows a sharp peak at a certain depth and very steep drop backward the peak, which is called as Bragg peak.

Fig. 1.3 shows the depth-dose distributions of various radiation beams. The doses of proton beam and carbon ion beam become maximum at the certain depth and decrease rapidly and significantly in the deeper range, while those of X-ray and gamma ray have blurred peak and gradually decrease in the deeper region. The dose distribution of carbon ion beam has much sharper peak than one of proton beam. On the other hand, at the back of the peak area, proton dose distribution decreases to almost zero dose while carbon ion gives low and near-flat dose, which is called fragmentation tail. Generally speaking, as can be seen above, the dose distribution of particle beams such as proton or carbon ion has a sharp peak rather than photon beams, such as X-ray or gamma ray. Furthermore, the dose distribution of particle beams shows a sharp edge also in the lateral direction to the beam path without collimation. Thus, particle beam can reduce the unnecessary dose to outside

the tumor compared with X-ray. In particle beam therapy, proton, which is the positive charged hydrogen nucleus, is most widely used all over the world while several treatment facilities uses carbon ion beam. Carbon nucleus is almost twelves times heavier than proton and has much sharper Bragg peak and lateral edge in its dose distribution, while much larger apparatus and facility building is required to generate higher energy therapeutic carbon beam.

The next two sections describe more details in the equipment configuration and the irradiation methods of particle beam therapy.
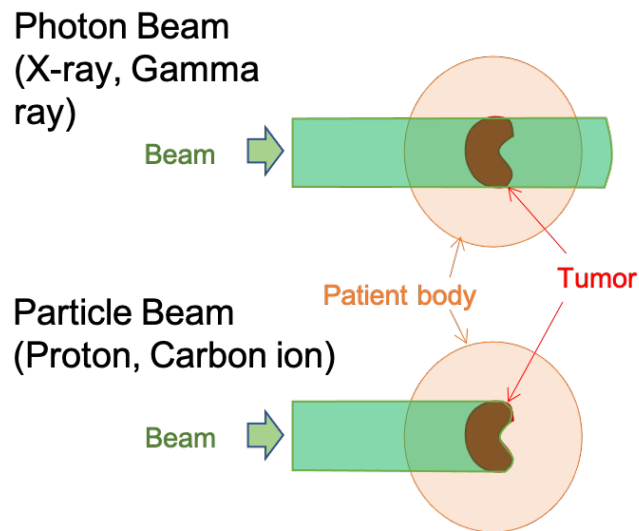
Fig. 1.2 A schematic of the difference in physical properties between photon beam and particle beam irradiated to the cancer patient.

1.2 Equipments configuration

1.2.1 Overview of treatment facility

Figure 1.4 is a schematic of the apparatuses in Heavy Ion Medical Accelerator in Chiba (HIMAC) [15, 16] as an example of the treatment facility. The facility contains the particle beam line which generate, accelerate and transport the particle beam and the treatment rooms in which the beams are irradiated to the patients. The particle beam line normally consists of an ion source, a pre-injector [17], a main accelerator and beam transport lines. In the treatment room, a rotational gantry and a beam irradiation nozzle are equipped at the end of the particle beam line. In this section, we overview the main accelerator, the rotational
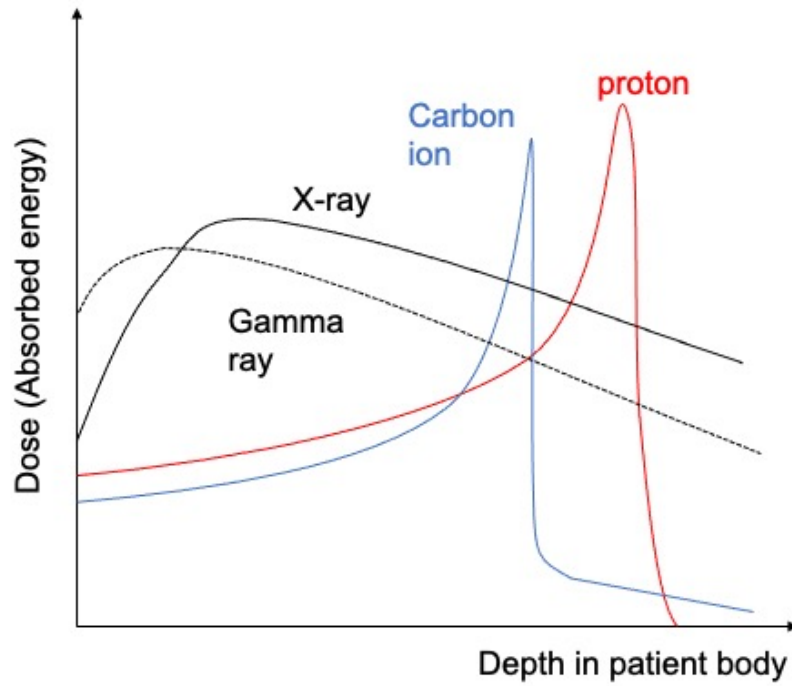
Fig. 1.3 Comparison of depth dose distributions of proton beam, carbon ion beam, X-ray and Gamma-ray in the patient body.

gantry and the beam irradiation nozzle which may contribute the size minimization and high precision irradiation, which are main points of this research
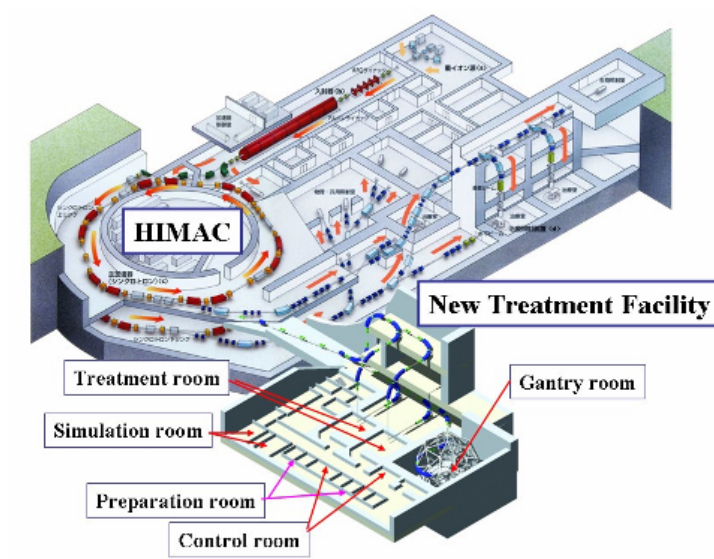
Fig. 1.4 A schematic view of the particle beam treatment facility. [16]

1.2.2   Synchrotron

For cancer treatment, the energy of the particle beam is increased up to approximately 235 mega electron volts (MeV) and 400 MeV/u with proton and carbon, respectively, by using the main accelerator. The beam range of these energies correspond to the depth of prostate cancer tumor from the human body surface, which is the largest range required for cancer therapy. While there are some types of main accelerators, such as synchrotron [18, 19], cyclotron [20, 21], or synchro-cyclotron [22], this research focuses on synchrotron because it has the highest beam intensity and the highest precision in beam irradiation, which is clinically the best suitable to cancer therapy [23]. On the other hand, synchrotron is the largest in its size among three above accelerator types and requires large facility area, thus the technologies for down-sizing the apparatus is in strong demand. Synchrotron consists of several bending electromagnets and usually one acceleration cavity. An acceleration cavity generates a high frequency electric field where the phase is synchronized with the beam passing timing in order to accelerate it. A beam bending electromagnet generates a magnetic field which can bend the beam traveling direction based on Lorentz force,

$$f = qv \times B, \tag{1.1}$$

where q and v shows the electric charge and velocity of the particle. If the beam velocity is constant and the relativistic effects can be ignored, the bending radius R of the beam trajectory can be expressed by

$$R = \frac{mv}{qB}, \tag{1.2}$$

which is known as Larmor radius. The magnetic field density B should be modulated corresponding the beam velocity v in order to make the beam bending radius become constant. If the apparatus can generate higher magnetic field, the size of the synchrotron can be smaller.

1.2.3   Rotational gantry

The particle beam should be irradiated as avoiding the important tissues, thus the beam irradiation angle are often limited. The optimum beam irradiation angle depends on case by case of the patients. To provide the best beam irradiation angle every patient, rotational gantries [24] are often installed in particle therapy facilities. This structure can mechanically rotate 360 degrees around the patient on the couch with the rotational axis along the longitudinal
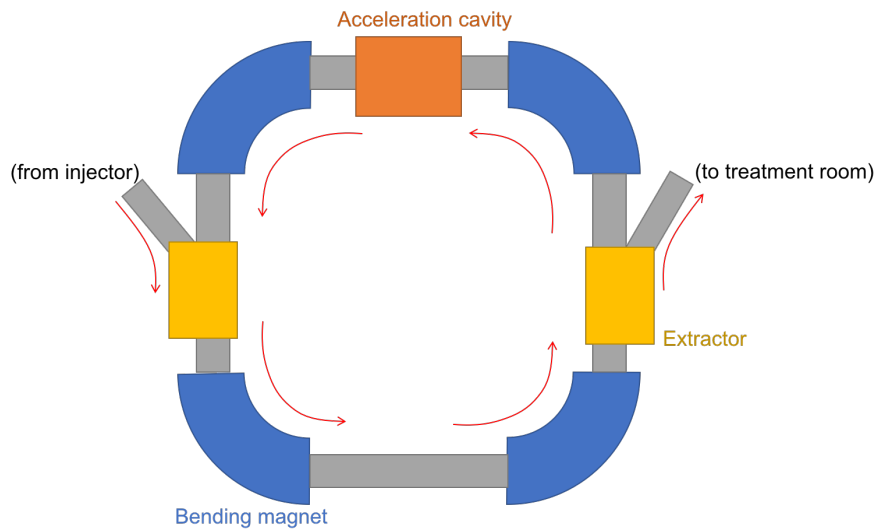
Fig. 1.5 A schematic of Synchrotron accelerator.

direction. The combination of the rotational gantry and the movable patient couch enables the particle beam delivery to the patient from arbitral direction. The beam line contained in the rotational gantry consists of several beam bending magnets and beam focusing magnets. The irradiation nozzle, which is explained in detail in the following section, is also located at the end of the beam line.
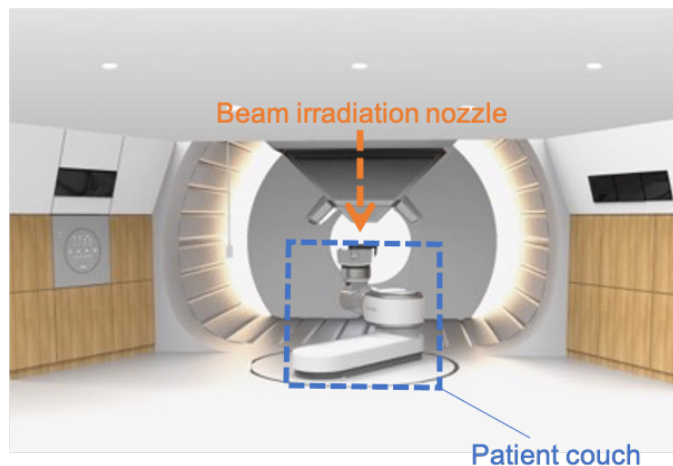
Fig. 1.6 A rotational gantry in the view from the treatment room. [24]
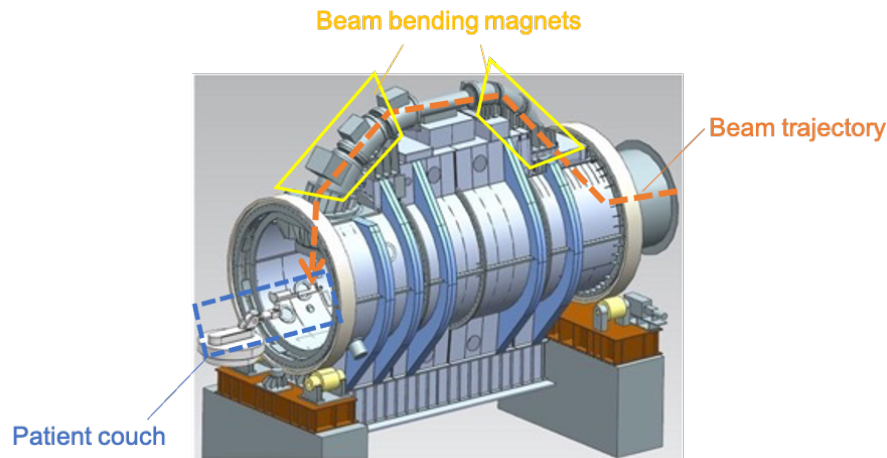
Fig. 1.7 A rotational gantry in the view from backyard. [24]

1.2.4 Irradiation Nozzle

Fig. 1.8 shows the schematic of typical irradiation nozzle [25]. The nozzle consists of a pair of scanning electromagnets, a scatter, a ridge filter, range shifters, beam monitors, multi-leaf collimators, and a bolus. The combination of these components can realize very precise dose delivery which suit to a large number of types of tumors of many patients, by using of several beam irradiation methods to form dose distribution which will be shown in detail in the following section. Some of these components are not necessarily implemented depending on the nozzle specification.

1.3 Beam irradiation methods

Since cancer tumor has a three dimensional volume while the dose distribution of the original particle beam has very sharp peak, an appropriate beam field have to be formed to give an optimal dose distribution which fit to the tumor volume. In many cases, the ideal dose distribution is the one in which the dose is homogeneous within the tumor but is as small as possible out of the tumor. In the history of particle beam therapy, three major methods have been considered in order to enclose the dose distribution to the ideal one. The irradiation methods can be classified into passive method, layer stacking method or pencil beam scanning method depending on the ways of forming a beam field in lateral and depth direction are passive or active.
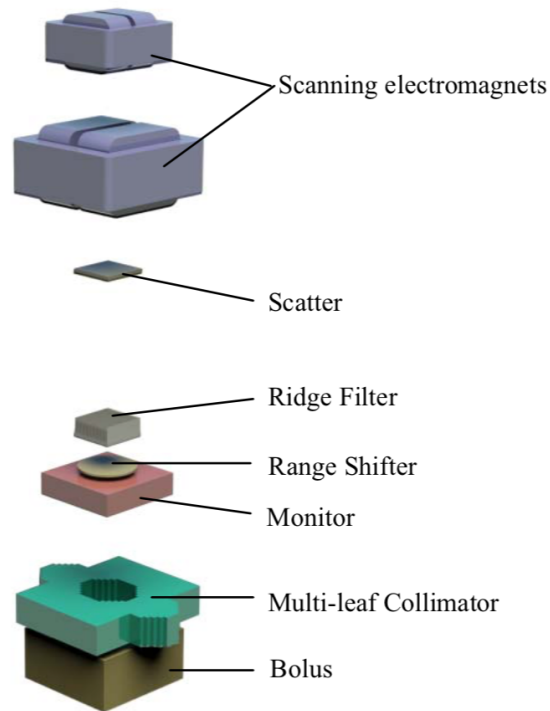
Fig. 1.8 A schematic of beam irradiation nozzle.
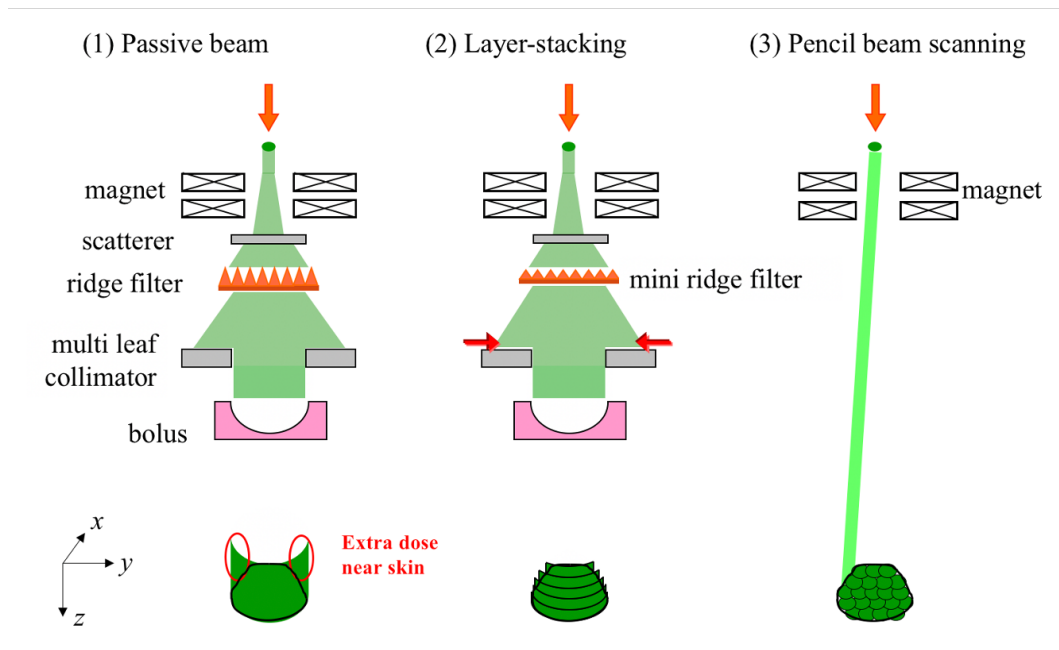
Fig. 1.9 Three irradiation methods to achieve three-dimensional conformal dose distribution.

1.3.1 Passive method

Passive method[26, 27] is the first standard method which is widely used for clinical perpose. In this method, the homogeneous beam field is formed both in depth and lateral direction. In lateral (xy) direction, the beam is rotated by using of wobbler magnets and is scattered by a scatterer. Wobbler magnets are two pairs of magnets and each pair generates approximately homogeneous magnetic field to y and x direction, which can slightly bend the beam direction to x and y direction, respectively. By applying alternating current to each magnets, the beam direction moves with a circular path. The scatterer is made of a solid metal or plastic and the beam size is expanded by a scattering effect. by adjusting the balance between the wobbling radius and the beam size after scattering, almost homogeneous dose distribution can be formed in lateral direction. Since the beam wobbling period is much shorter than the time of beam irradiation to the patient, the dose distribution can be seen as passively homogeneous.

Ridge-filters (RGFs) are also installed in the nozzle in order to form homogeneous dose distribution along z direction. Fig. 1.10 shows a schematic of RGF. RGF consists of a lot of "ridges" which have the varying thickness along the beam direction z. When the beam is injected across the RGF, some of beam passes through the thick part and some passes the thin part of the ridge along the beam direction. The dose peak depth where the beam can reach corresponds to the thickness of the ridge where the beam passes, and the beams of various ranges are mixed after passing the RGF. By arranging the shape of the ridge, we can control the dose distribution along z direction, usually as homogeneous as possible within the beam range of the target. This expanded, homogeneous dose distribution is called as spread-out Bragg peak (SOBP).

By combining the wobbler magnets, scatterer and RGF, three-dimensional large field of homogeneous dose can be achieved. Finally, multi-leaf collimator (MLC) [28] blocks unnecessary dose outside the target in x and y direction. Fig. 1.11 shows a schematic of MLC. MLC consists of a lot of "leaves" which is made of iron and can completely stop the irradiated beam. All the leaves can move in either x or y direction. By arranging the leaf edge positions corresponding to the projection of the contour of the target, the homogeneous dose are give only in the target.

1.3.2 Layer stacking method

In the layer stacking method[29, 30], the target was divided into several layers which is perpendicular to the beam direction and each layer is irradiated sequentially. For each layer
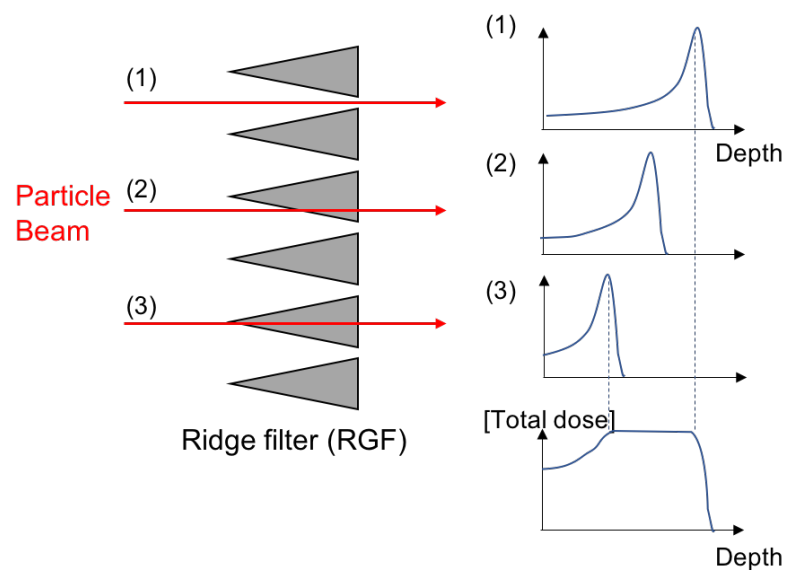
Fig. 1.10 A schematic of ridge-filter.
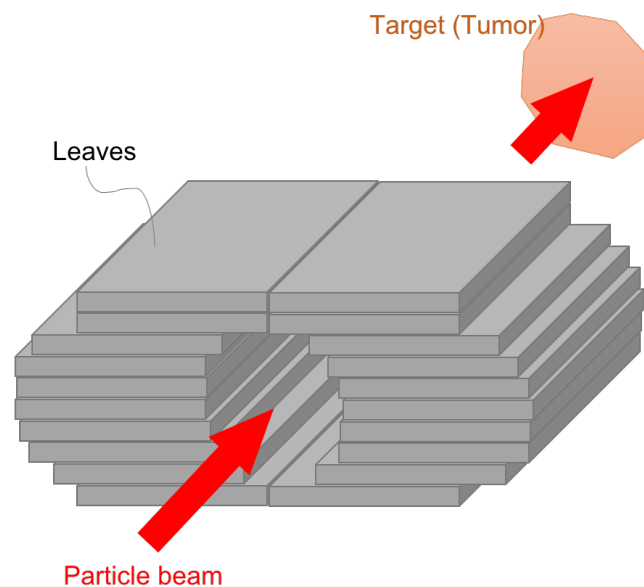
Fig. 1.11 A schematic of multi-leaf collimetor.

irradiation, the dose peak of the beam is expanded in xy plane by using wobbler magnets and scatterer as same to passive method. On the other hand, in z direction, the depth dose distribution has a sharp peak which is slightly expanded from Bragg peak and called as mini-SOBP, by using a mini-ridge-filter (mini-RGF). Or, a raw-Bragg peak without RGF is sometimes used in the layer stacking method. A homogeneous SOBP is formed by stacking

the mini-SOBPs of the layers. For each layer, SOBP dose is expressed as

$$D_{\text{SOBP}}(z) = \sum_{i=1}^{N} \chi_i d_i(z),$$ (1.3)

where χ_i and $d_i(z)$ are the beam amount and dose distribution of the i-th layer, respectively. N is the number of layers. Unlike passive method where the shape of the dose distribution is passively determined and only the total beam amount is prescribed, layer stacking method has a degree of freedom in determining the balance in the beam amount of each layer. In order to form a homogeneous distribution of SOPB D_{SOBP}, χ_i should be optimized based on objective function. For determining χ_i, treatment planning software which contains an optimization algorithm [31] is employed. One characteristic point of the layer stacking method is that MLC aperture is squeezed layer by layer corresponding to the cross sectional shape of the layer of the target [32]. This feature enables to reduce the extra dose outside the target at the proximal side as shown in Fig. 1.12. With this point, the layer stacking method can supply more precise dose distribution which is conformal to the target shape and realize better sparing with the organs at risk (OARs) around the tumor.
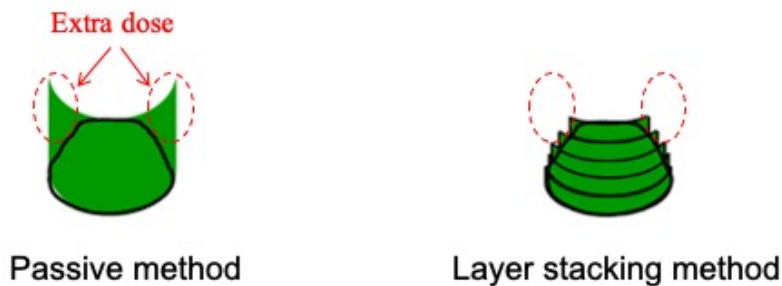
Fig. 1.12 The extra dose in the proximal side of the target is suppressed in the layer stacking method.

1.3.3 Pencil beam scanning method

Pencil beam scanning (PBS) was the first proposed by Kanai et al [33] and the first clinical treatment was carried out in 1996 at Paul Scherrer Institute (PSI) in Switzerland. In PBS, the target is at first divided into several layers, as the same to the layer stacking method, and then a lot of beam spots are located in each layer [34–36] . A pencil beam, which has a sharp dose peak in each of x, y and z direction, irradiates one spot and then move to the next spot.

For moving from spot to spot, the particle beam is slightly bended by Lorenz force under the magnetic field generated by the scanning magnets located in the irradiation nozzle [37]. After all the spots in one layer are irradiated, then layer is changed by shifting the beam energy.

Total dose distribution in pencil beam scanning is represented like one in the layer stacking method, as

$$D_{\text{total}}(x, y, z) = \sum_{i=1}^{N} \chi_i d_i(x, y, z), \tag{1.4}$$

where χ_i and $d_i(x, y, z)$ are the beam amount and the dose distribution of the i-th spot, respectively; N is the number of spots. As the same to layer stacking method, PBS can also provide three-dimensional conformal dose distribution to the target in which the unnecessary extra dose outside the target. Since it has much higher degree of freedom in determining the spot locations and number of particles to each spot, PBS has a larger potential that the dose distribution can be much closer to the ideal one compared with the layer stacking method.

Another large advantage of PBS compared with passive method and layer stacking method is that it does not require MLC, RGF nor bolus. Particularly, since the bolus should be fabricated with patient-specific in the passive method and the layer stacking method, PBS enables much faster start of the treatment which benefit for the patient than other two methods.

1.4   Issues of particle beam therapy and purpose of the research

Although particle beam has very attractive physical properties for cancer treatment, issues still remain to provide the benefit of this therapy for much larger number of patients. First of all, since very high energy particle beam is required to reach to the depth of cancer tumors in the human bodies, huge equipment is needed for the particle acceleration. For example, prostate cancer tumor usually locates at around 30 centimeter depth from the patient skin, which is the largest range requirement among every remediable cancer with the particle beam. This range corresponds to almost 230 MeV in the case of proton beam or 400MeV/u in the case of carbon beam, and the synchrotron accelerator with a diameter of almost 6 meter or 20 meter is required, respectively, to generate such high energy particle beam. Therefore, only limited facilities which have large enough area to contain the particle accelerator and additional

devices can currently supply particle beam therapy to the patients. In many cases, since it is difficult to construct such a large facility in the center of the city with high population density, facilities are often built in the suburban or in the countryside far from the midtown. This situation is very inconvenient to the patients, especially when they consider to take a daily-visit care while continuing their works, and degrades the advantage of the particle beam therapy in terms of QOL. Besides, because of very high initial cost to construct huge facility and running cost of electricity for high energy beam acceleration, the treatment cost usually becomes higher than other therapies. For above reasons, not all the cancer patient who are clinically compatible to particle therapy can choose this therapy. In addition, people require particle therapy to have significant clinical advantages over other therapies.

To resolve above issues and to wide-spread the particle therapy to much more patients, this research focuses on two technological challenges as follows:

- The equipment size for particle beam therapy should be much reduced in order to enable to be constructed a lot of hospitals with a limited space even in the center of the city.

- To enhance the advantage of particle beam therapy, the beam irradiation technology should be much sophisticated to achieve high-accuracy beam irradiation which matches to the complicated shape of the cancer tumor.

1.4.1 Topology optimization of superconducting magnets for particle accelerators

As already mentioned, there have been strong demands of smaller size of the particle therapy facility in order to widespread the usage of particle beam treatment. For the size reduction of the beam acceleration and transport apparatus, we need to increase the magnetic field strength for bending the beam generated by bending electromagnets. Using superconducting material is one solutions to generate large magnetic field [38, 39] while there is drawbacks in material cost, cooling cost, manufacturing issues, and difficulties in adjustment of field distribution.

There has been increasing interests in high temperature superconducting (HTS) material, which has higher critical temperature than conventional low temperature superconductors (LTS). HTS materials, such as Yttrium barium copper oxide (YBCO), can become superconducting state with liquid nitrogen, instead of liquid helium. That makes cooling system much

simpler and low cost. On the other hand, unlike copper cables and LTS cables which has circular cross section, YBCO cable is in a tape-like shape and has a strict constraint in its bending radius. Therefore, in terms of manufacturing, there are a limitation in the shape of HTS coils.

For particle accelerators, a saddle-shaped coil [40–42] has been considered to be suitable, because of homogeneous B-L product. B-L product is an integration of magnetic flux density along the trajectory of the particle beam. B-L product is proportional to the bending of beam direction, and ideally should be the same at any position of the beam injection to the magnet. Saddle-shaped coil can reduce the magnetic field from the contribution of coil-end part at the beam entrance of the magnet. However, since the saddle-shape is complicated and includes more than one winding axis, there are manufacturing difficulties and special winding equipment is needed. Therefore, in this research, we propose to use topology optimization to obtain the cross-sectional shape of accelerator coil which can be easily presented by a stack of simple square-shaped coils.

Figure 1.13 describes three types of design optimization methodologies. Parametric optimization is the most popular option, in which the design is defined by a finite number of design variables corresponding to characteristics of each part, e.g., length, width, angle, etc. Shape optimization has higher degree of freedom in the shape change, where the shape boundary can move arbitrary. Topology optimization has the highest degree of freedom, where new boundary generation and boundary disappearance are allowed; i.e., new holes and islands may be generated. By using topology optimization, we design a new cross sectional shape of superconducting coil, which is different from conventional rectangular cross section of square-shaped coils.
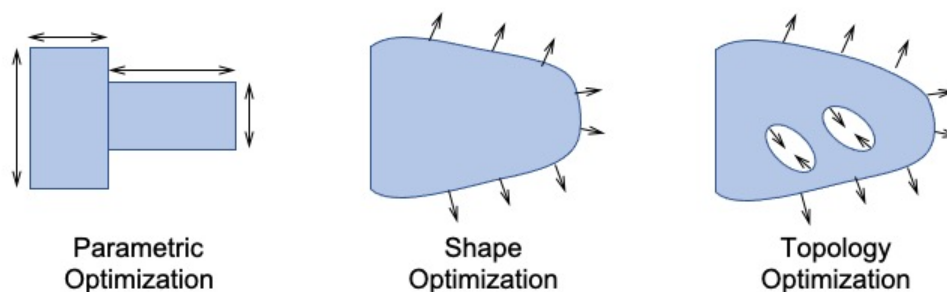
Fig. 1.13 Schematics for 3 types of design optimization methodologies.

1.4.2   Robust optimization considering patient motion

As well as smaller size of facilities, precise beam irradiation have also been required, in order to take much larger clinical advantage over other cancer therapies, especially X-ray radiation therapy. Although active irradiation techniques such as layer stacking method and pencil beam scanning method were developed to achieve three-dimensional conformal dose distribution to the tumor sparing the healthy tissue, these active methods also have an disadvantage that the dose distribution can become very unstable under the range uncertainty of the beam [43] and patient motion during the beam irradiation [44]. This effect is described in Fig. 1.14 with an example in layer stacking beam irradiation. Since each layer is irradiated sequentially, not at the same time, the dose distribution is affected by the relative position error among layers. A total dose distribution may have hot and/or cold spot near the layer with a large position error. PBS method has the same problem, because each spot is irradiated sequentially as similar as layers.

For X-ray radiation therapy, a methodology of robustness optimization [45], which enable to make the total dose distribution less sensitive to the disturbance, e.g., patient respiration motion, was proposed. As particle beam should be sensitive to patient motion not only along lateral direction but also depth direction due to the nature of Bragg peak, robustness of treatment planning is more important. For layer stacking particle therapy, use of RGF to broaden Bragg peak to make it less sensitive to the patient motion along depth direction was proposed [46]. However, loosening Bragg peak may cause degradation of distal fall-off, which is the steepness of total dose distribution behind the tumor. In this research, we propose a robust optimization method for beam amount irradiated to each layer, considering patient motion including depth direction, while keeping good distal fall-off.

1.4.3   Spot arrangement optimization for Pencil Beam Scanning

Pencil beam scanning (PBS) technique has a potential to offer much superior dose delivery to the patient, in which unnecessary dose to the healthy tissue can be much more reduced. This is mainly because PBS has quite high degree of freedom in treatment planing, especially in determining beam irradiation amount to thousands of spots, which is much larger than the number of layers in the layer stacking method. Further more, PBS includes other degree of freedom in determining spot positions and scan trajectory. A lot of optimization strategies in the treatment planning [47, 48] were proposed before. However, most of prior studies have been focusing on determination of the beam amount to each spot, and the spot position
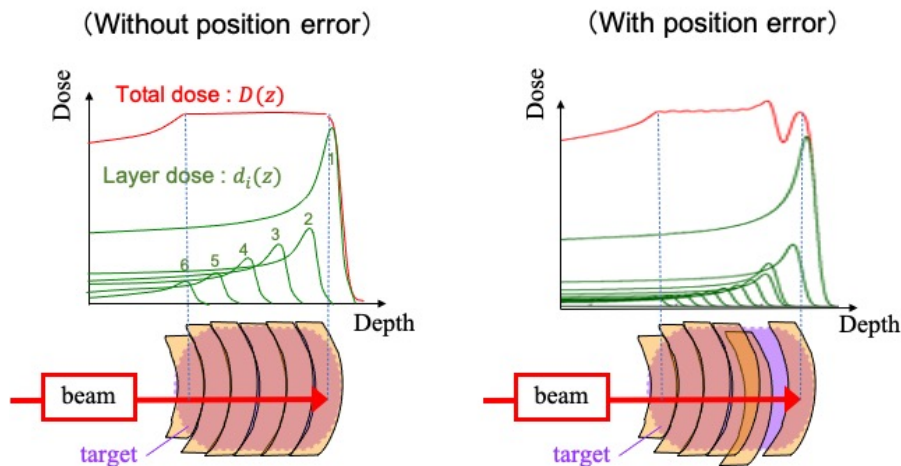
Fig. 1.14 Dose distribution inhomogeneity caused by range uncertainty and patient motion during layer stacking irradiation.

arrangement is normally fixed to be a square lattice pattern. Those methods may not realize the full potential of PBS to achieve the best beam dose distribution. Several studies have addressed scan path optimization techniques [49–51] , in which the order of spot irradiation is optimized while each spot position is unchanged from the initial lattice pattern. There were very few studies focusing on non-lattice pattern of spot arrangement in PBS.

On the other hand, many types of layout optimization techniques have been developed in the field of mechanical engineering, e.g., arrangement of actuator locations for deformable mirrors [52, 53]. In this research, therefore we tried to apply those layout optimization methodologies to design optimal spot arrangement, which can reduce the number of spots while keeping the quality of the dose distribution in PBS. Furthermore, we also propose modified algorithm to speedup the layout optimization process for PBS, because positions of thousands of spots have to be optimized in PBS and it may lead a long computation time, while most of the prior layout optimization studies normally handled layouts of a few tens of object to be optimized.

1.5   Organization of the dissertation

In this research, we address three theme as follows:

- We propose a topology optimization method of superconducting coil of particle accelerator for the purpose of minimizing the facility size.

- We propose a robustness optimization method of determining the beam amount of each layer, for the purpose of enhance the robustness of the dose distribution against the patient position error in layer stacking particle therapy.

- We propose a spot arrangement optimization method of pencil beam scanning for the purpose of reducing the unnecessary dose outside the tumor while reducing the total number of spot.

In Chapter 2, a topology optimization method of superconducting coil for compact size accelerators is constructed. In the proposed method, filtering based on Helmholtz type partial differential equation and the projection based on Heaviside function were applied to the density function, in order to relax the solution space of the optimization problem and to reduce the gray scale issue.

In Chapter 3, a robust optimization method of beam amount in the layer stacking is reported. In the proposed method, the upper limit of the beam amount to each layer is set and combinations of the limit setting are tested. The best pattern of the limit setting is selected by evaluating the robustness based on standard deviation of the depth dose distribution assuming Gaussian probability of the layer depth error.

In Chapter 4, a layout optimization method of the beam spots in the pencil beam scanning is reported. In the developed heuristic algorithm, enough large number of spots are densely located at the initial state and the spot with the smallest contribution to form the dose distribution is removed one by one through iterations. The objective function to determine the spot beam amount and the error function to judge the removable spot, at each step in the algorithm, is formulated.

The last chapter of this dissertation summarizes the proposed optimization methodology and the obtained result of each chapter.

Chapter 2

Topology Optimization of Superconducting Electromagnets for Particle Accelerators

The purpose of this chapter is to establish the designing scheme of simplified structure of superconducting coils for particle beam accelerators, which can be easily manufactured, by using of the procedure of topology optimization. We set three axes of design requirements for particle accelerators; magnetic field homogeneity, magnetic field strength and cross sectional area of the coil. We formulated the objective functional and developed the optimization algorithm to solve the multi-objective problem. In the algorithm, we applied the Heaviside-projection method to avoid gray-scales and excessively complex structures. Finally, the validity of the proposed scheme was confirmed with numerical examples of coil designs.

2.1   Introduction

Topology optimization was at first proposed by Bendsøe and Kikuchi [54] and has the highest degree of freedom in structural optimization. The biggest feature of topology optimization is a replacement of structural optimization problem with a spacial distribution problem of material, which enables a drastic structural deformation where not only the shape change of material boundary but also a generation and vanishment of holes. However, it is often an ill-posed problem because material density is allowed to have any discontinuous substructures within infinite small region. In order to relax the problem into well-posed,

homogeneity method [54] and density method [55, 56] can replace the discontinuous function with a continuous smooth function, while that sometimes reads to grayscale and excessively complicated substructure. The other approach to avoid grayscale is the level set method [57, 58], but in this study we apply density method because it is easy to implement for numerical computation.

With density method, design variable smoothing using Gaussian filter [59, 60] or projection method based on Heaviside function [61] is a considerable option for a relaxation of grayscale and complicated substructure. However, the treatment of filtering function or Heaviside function is quite perplexing on the design domain boundary, while these scheme is easy to implement in additional to density method. On the other hand, Kawamoto et al. [62] proposed Heaviside function projection with using Helmholtz equation. Their method didn't require any special care to functions on design domain boundary, furthermore, the level of complexity can qualitatively be controlled by a parameter in Helmholtz equation. These methods were used for a lot of design optimization problem that mainly consider the mechanical stiffness since long ago, on the other hand, some works were done for the optimization problems with electromagnetism, e.g., topology optimization of electromagnetic actuators or rotational motors [63, 64].

Beam bending magnets of charged particle accelerator is one of considerable electromagnetic applications for topology optimization. Accelerators have increasing needs for widely various purpose; nuclear experiment[65], cancer therapy[66], micro fabrication of semiconductor[67], and treatment of radioactive nuclear wastes[68]. Many of them has demands for miniaturization by using of superconducting coil with strong magnetic field. The beam bending magnet of particle accelerator is required to generate very precise magnetic field and so-called $\cos\theta$ type coil [69, 70] is widely used. To achieve three-dimensionally distributed, complicated current density, some coil winging method, which are named direct winding [71] or surface winding [72], were developed.

However, such special winding method leads a complicated manufacturing process and the high manufacturing cost, compared with simple pancake type, racetrack type or square-shaped coils. Furthermore, Bi or Y based high-Tc superconducting wires are usually tape-like flat wire and has lower degree of freedom in manufacturability, compared with conventional low-Tc superconducting wires such as NbTi or Nb_3Sn, therefore a lot of technological issues will be considered for industrial application if needs for high-Tc would increase in the future.

Simple pancake type or square shape coil, which has only one axis of winding, can be comparably easily manufactured with tape-like cable. Actually, design optimization with pancake type superconducting coil were studied for MRI and SMES [73, 74]. However, they employed parameter optimization where the coil cross sectional shape consists of one or plural rectangular while topology changes, i.e. change of the number of rectangular or generation of holes inside a rectangular, were not considered. In this study, based on a square-shaped coil with one winding axis, the cross-sectional shape of the coil is optimized with a high degree of freedom, and a methodology for finding a coil structure with a magnetic field distribution suitable for accelerators based on a framework of topology optimization.

2.2   Method of optimization

2.2.1   Structure expression of the coil in topology optimization

The basic concept of topology optimization is to introduce a characteristic function $\chi(x)$ into a fixed design domain D which includes the optimum configuration Ω to solve, as in the following Eq. (2.1). Here, the value of characteristic function $\chi(x)$ is 1 and 0 in the material region and the void region, respectively, to represent the optimized structure.

$$\chi(x) = \begin{cases} 1 & \text{if} \quad x \in \Omega \\ 0 & \text{if} \quad x \in D \backslash \Omega \end{cases} \tag{2.1}$$

With this shape expression, not only the change of boundary shape but also the change of topology, e.g., generation or vanishment of holes, is allowed in the optimization process. However, characteristic function $\chi(x)$ has very ill discontinuity that it is allowed to be oscillated between 0 and 1 with an infinite small steps, and that reads to quite difficult treatment in a mathematical sense. In order to solve this problem, homogenization method and density method were developed to replace the discontinuous characteristic function $\chi(x)$ with an approximated continuous smooth function which is easier to treat. Homogenization method introduces infinite small cyclic microstructures which enables to treat the relationship between physical property and continuous regularized density, while there is mathematical difficulty in its process.

In density method, on the other hand, the characteristic function $\chi(x)$ is approximated by a scalar monomial. This method can be quite simply implemented as a numerical computation while it is not strictly correct in a mathematical sense. In this work, we replace the design

variable with a continuous variable by this density method, i.e., the current density J in the coil is represented by using a regularized density function ρ, which is a continuous function between 0 and 1, as follows,

$$J = J_0 \rho^p, \tag{2.2}$$

where J_0 is the maximum value of current density. p the penalty parameter, which is a positive constant and set to be 1 in this work. Within the cross sectional plane which is perpendicular to the current flow direction, the current density is proportional to the number of conducting cables which go across the plane. Therefore, we set the design domain at the cross sectional plane and we can understand that the regularized density function stands for cable density which is proportional to the current density.

2.2.2   Filtering method and Heaviside projection

In density method, generally speaking, the optimized solution includes the grayscale in which the regularized density function ρ has an intermediate value between 0 and 1. This grayscale should be as less as possible because of manufacturability. In structural optimization problems, it is known that the grayscale can be reduce if penalty parameter is set to be 2 or more, generally 3. In this study, however, the penalty parameter is set to be 1 because the regularized density function is proportional to current density, as mentioned in the previous section, therefore, the optimized solution can include a lot of grayscale. Besides, the solution can possibly have excessively complicated substructure depending on parameters setting. Although physical performance of the device is expected to be higher when grayscale or complicated substructures, such optimum solution is impossible or quite difficult to realize in manufacturing within a reasonable cost. Therefore, a lot of schemes to remove grayscale and excessively complicated substructure in topology optimization: For example, the filtering method [59, 60] to smooth the design function or sensitivity, and projection method [61] to binarize density value into 0 or 1 with keeping continuity of the function based on regularized Heaviside function, were proposed.

Kawamoto et al. [62] proposed a method to solve a Helmholtz type partial differential equation (PDE), which is much simpler to implement for computation. With their method, for two-dimensional problem, a scalar function $\phi(x, y)$ and its smoothed function $\psi(x, y)$ have the relationship as following partial differential equation.

$$\left[-R_x^2 \frac{\partial^2}{\partial x^2} - R_y^2 \frac{\partial^2}{\partial y^2} \right] \psi(x,y) + \psi(x,y) = \phi(x,y), \tag{2.3}$$

where R_x and R_y is filtering radius to x and y direction, respectively. ψ become much smoother when the filtering radius is larger, while ψ equals to the original function ϕ when filtering radius is 0. Kawamoto[62] et al. used isotropic filtering radius in two dimension for mean compliance minimization problem. This study is, on the other hand, an optimization for coil cross sectional shape, thus the degree of freedom in determining the shape is limited with a tape width to the winding axial direction while the the degree of freedom is much higher to radial direction by adjusting the number of winding turns. Therefore, we introduced an anisotropic filtering radius to represent this difference of degree of freedom. Eq. (2.3) can be solved by applying finite element method (FEM) for ψ and ϕ based on rectangular mesh which is shown in the following section.

Then, the distribution of material density $\rho(x)$ is obtained by using the approximated Heaviside function as follows, in order to remove the gray scale, i.e. intermediate values, from the filtered design variable ψ for binarization.

$$\rho(x) = H_a(\psi) =$$
$$\begin{cases} 0 & \text{if} \quad \psi < -h \\ \frac{1}{2} + \frac{15}{16}\frac{\psi}{h} - \frac{5}{8}(\frac{\psi}{h})^3 + \frac{3}{16}(\frac{\psi}{h})^5 & \text{if} \quad -h \leq \psi \leq h \\ 1 & \text{if} \quad \psi > h \end{cases} \tag{2.4}$$

where h is a width of Heavisde function and is set to be enough small a value for binarizing the density into 0 or 1 in the almost of design domain, while keeping the continuity of the objective functional. Here, the density value 0 is interpreted to be a void region, while the density value 1 is interpreted to be a coil material where a constant current flows.

2.2.3   Objective functionals

In this work, we consider following three points as the design First, since the passing particle beam should take the same force independent of its path in the bending magnets for particle accelerators, the integrated magnetic flux density to z direction $B_z(x,y)$ which the particle beam passing to y direction in the xy plane experiences, that is called as B-L product, should be homogeneous in the x direction. The homogeneity of B-L product defined by eq. (2.6) should be as small as possible. For example, in the previous study about a bending magnet for

a rotation gantry in the heavy ion beam therapy, the target value for B-L product homogeneity was set to be less tthan 0.1% and the actual design was reported to be at the order of 10^{-4}. In this study, therefore, we set the target value for B-L product homogeneity less than 0.1% as them.

Second, since the averaged magnetic flux density should be the same to the design value in order to control the curvature of the particle beam bending, the target value was set to be $B_{zp} = 3.0\,\text{T}$ in this work as the typical value of the magnetic flux density for the superconducting magnet, and the corresponding objective function f_2 was defined as eq. (2.7). Third, The cross sectional area of the coil defined by f_3 in eq. (2.8) to reduce the material cost. Above three requirements have trade-off relations each other and we should treat a multi-objective optimization problem. We applied the weighted summation method, where the objective functional f was defined as the sum of three functionals with weight coefficients w_1, w_2, w_3 as in eq. (2.5).

$$\text{minimize} \quad f = w_1 f_1 + w_2 f_2 + w_3 f_3. \tag{2.5}$$

$$f_1 = \frac{\max_x \left(\int_{y_l}^{y_u} B_z(x, y')dy' \right) - \min_x \left(\int_{y_l}^{y_u} B_z(x, y')dy'. \right)}{\int_{y_l}^{y_u} B_z(0, y')dy'} \tag{2.6}$$

$$f_2 = \frac{\int_{x_l}^{x_u} \left(B_z(x', 0) - B_{zp} \right)^2 dx'}{\int_{x_l}^{x_u} B_{zp}^2 dx'}. \tag{2.7}$$

$$f_3 = \frac{\int_D \rho(x_d, z_d)d\Omega}{\int_D d\Omega,} \tag{2.8}$$

where x_l, x_u, y_l, and y_u are the lower and upper bound of the evaluation region for the magnetic flux density in xy plane.

2.2.4   The optimization process

Fig. 2.1 shows the flowchart of the optimization. First, the initial value of the scalar function ϕ is set. Next, ψ and ρ is sequentially calculated based on the PDE filter of eq. (2.3) and based on Heaviside projection of eq. (2.4), respectively. Then the coil configuration is determined and the value of objective functional in eq. (2.5) can be calculated. If the

objective functional is converged, the loop is over and the optimization process is terminated. On the other hand, if the objective functional is not converged, the sensitivity of the objective functional f with the scalar function ϕ is derived and ϕ is updated by using of the algorithm of Method of Moving Asymptote (MMA)[75].

Set initial value for $\phi(x_d, z_d)$

Calculate $\psi(x_d, z_d)$ using PDE filter

Calculate $\rho(x_d, z_d)$ using Heaviside's projection

Calculate the value of objective function

Converge?   yes

no

update $\phi(x_d, z_d)$ using MMA

Calculate the sensitivity of objective function

Optimal configuration
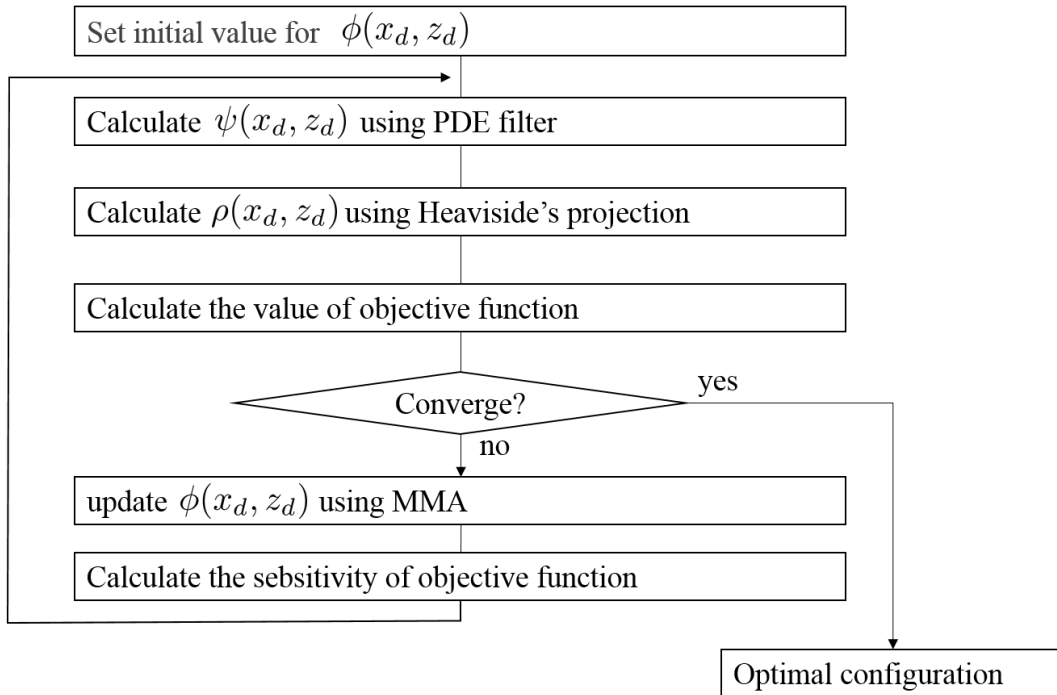
Fig. 2.1 Flowchart of optimization

2.3 Numerical Examples

2.3.1 The settings of the design domain and parameters

Fig. 2.2 is the schematic of the relationship between three dimensional coil configuration and the design domain in its xz plane. The coil consists of plural coil components and each component is a square-shaped coil which consists of four linear parts and four curve parts of 90 degrees. With the requirement of B-L product homogeneity, the optimal coil configuration should has symmetries with respect to each of xy, yz, and zx plane, thus the whole coil configuration in three dimension can be determined by setting the shape of coil cross section in the first quadrant in xz plane. Therefore, this is an optimization problem for two dimensional distribution of the coil material.

In this study, the desing domain was discretized by rectangular meshes with the size of 5 mm in x direction and 10 mm z direction. Mesh shape was set to be anisotropic because of following reasons: Tape-like superconducting cable has a rectangular cross sectional shape and its width along the winding axis was assumed to be 10 mm. the mesh size to x direction was decided considering the calculation cost, though the mesh size to x direction can be much smaller because the tape thickness is less than 1 mm.

As shown in fig. 2.3, the optimized cross sectional shape can be realized as the stack of plural square-shaped coil components which are sectioned by meshes. Since the size of the design domain to z direction was 150 mm and the size of the mesh to the same direction was 10 mm, every optimum solution can be represented by stacking at most 15 layers of coil components.

Filtering radius to z direction R_z was varied in the range from 1 mm to 100 mm and one to x direction R_x was set to be the half value of R_z in each case. The width h of Heaviside function was always set to be 0.1. y_l and y_u, which is the lower or upper limit of the integration range for B-L product, was set to be -1500 mm and 1500 mm, respectively. x_l and x_u, which is the lower or upper limit of evaluation region for B-L product or averaged magnetic flux density, was set to be -50 mm and 50 mm, respectively.

The weighting factors of the objective functional were determined as $w_1 = 0.9$, $w_2 = 0.1$. We empirically knew that this ratio of w_1 and w_2 simultaneously bring the B-L product homogeneity of almost 10^{-4} and also bring the difference of magnetic flux density from the target value of almost 1%. Here, the weight for the objective for B-L product homogeneity was stronger than one for the target value of the magnetic flux density because the absolute value of magnetic flux density can be adjusted by the coil current and there is at least 1% design margin considering the critical current of the superconducting coil, while B-L product homogeneity can be determine only by the coil configuration and there is no other margin.

w_3 was varied in three values; 0, 2.7×10^{-3}, and 9.1×10^{-3} in order to estimate the trade off between B-L product and cross sectional area. The loop of the flowchart was terminated after 15000 times update of the scalar function ϕ by MMA.

2.3.2   Calculation of magnetic flux density distribution

Fig. 2.4 shows the projection view of the square shaped coil component to xy plane. With z coordinate, the top and bottom surface of the coil component is at z_1 and z_2, respectively.
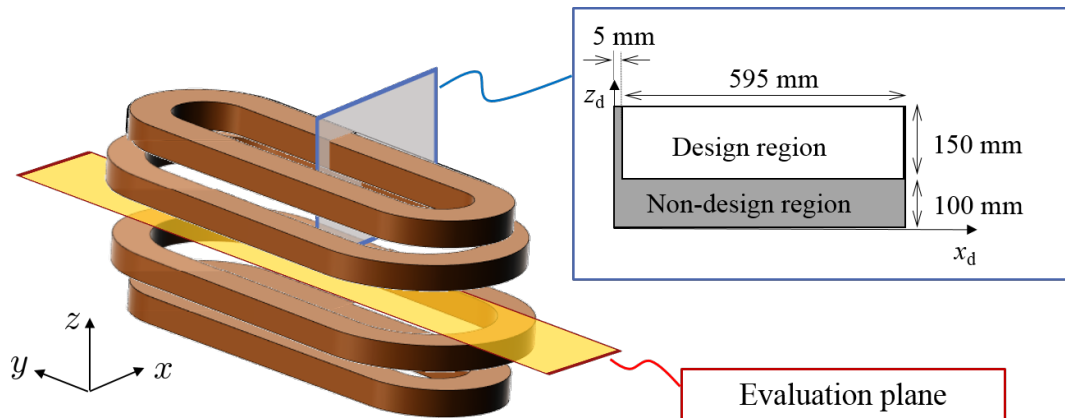
Fig. 2.2 Definition of design region and coil configuration
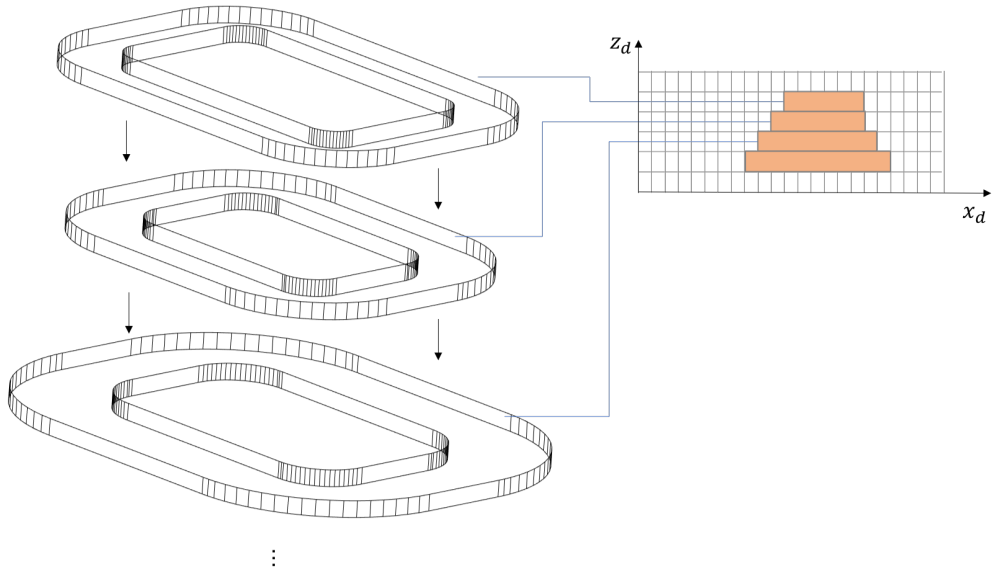
Fig. 2.3 Manufacturing the coil by stacking slices

The magnetic flux density to z direction at the point of interest (x, y, z) is calculated by the following equation[76].

$$B_z(x, y, z)$$

$$= \frac{\mu_0 J_0}{4\pi} \left[\sum_{i=1}^{2} \sum_{j=3}^{4} \sum_{k=1}^{2} (-1)^{i+j+k} F_{Lz}(X_i, Y_j, Z_k) \right.$$

$$+ \sum_{i=3}^{4} \sum_{j=1}^{2} \sum_{k=1}^{2} (-1)^{i+j+k} F_{Lz}(Y_j, X_i, Z_k)$$

$$+ \sum_{i=5}^{6} \sum_{j=3}^{4} \sum_{k=1}^{2} (-1)^{i+j+k} F_{Lz}(X_i, Y_j, Z_k)$$

$$+ \sum_{i=3}^{4} \sum_{j=5}^{6} \sum_{k=1}^{2} (-1)^{i+j+k} F_{Lz}(Y_j, X_i, Z_k)$$

$$+ \sum_{i=1}^{2} \sum_{j=1}^{2} (-1)^{i+j} \int_{\phi_1}^{\phi_1+\pi/2} F_{Rz1}(r_i, \phi, Z_j) d\phi$$

$$+ \sum_{i=1}^{2} \sum_{j=1}^{2} (-1)^{i+j} \int_{\phi_2}^{\phi_2+\pi/2} F_{Rz2}(r_i, \phi, Z_j) d\phi$$

$$+ \sum_{i=1}^{2} \sum_{j=1}^{2} (-1)^{i+j} \int_{\phi_3}^{\phi_3+\pi/2} F_{Rz3}(r_i, \phi, Z_j) d\phi$$

$$+ \sum_{i=1}^{2} \sum_{j=1}^{2} (-1)^{i+j} \int_{\phi_4}^{\phi_4+\pi/2} F_{Rz4}(r_i, \phi, Z_j) d\phi, \Bigg] \tag{2.9}$$

where

$$X_i = x - x_i, \tag{2.10}$$

$$Y_i = y - y_i, \tag{2.11}$$

$$Z_i = z - z_i. \tag{2.12}$$

r_1 and r_2 is the inner and outer radius of the curved parts, respectively, and has the following relation.

$$r_1 = x_5 - x_4 \tag{2.13}$$

$$r_2 = x_6 - x_4 \tag{2.14}$$

The functions F_{Lz} and F_{Rzk} ($k = 1, 2, 3, 4$) are defined as follows.

$$F_{Lz}(X,Y,Z) \tag{2.15}$$

$$= Y\ln(Z+\sqrt{X^2+Y^2+Z^2})+Z\ln(Y+\sqrt{X^2+Y^2+Z^2}) \tag{2.16}$$

$$-X\arctan\frac{YZ}{X\sqrt{X^2+Y^2+Z^2}} \tag{2.17}$$

$$F_{Rzk}(r,\phi,Z) \tag{2.18}$$

$$= Z\left[\ln(r-R_k\cos\phi+\sqrt{Z^2+r^2-2rR_k\cos\phi+R_k^2})\right. \tag{2.19}$$

$$+\frac{1}{2}\frac{R_k\cos\phi}{|Z|}\ln\frac{\sqrt{Z^2+r^2-2rR_k\cos\phi+R_k^2}-|Z|}{\sqrt{Z^2+r^2-2rR_k\cos\phi+R_k^2}+|Z|} \tag{2.20}$$

$$\left.-\frac{R_k\cos\phi}{Z}\arctan\frac{|Z|(r-R_k\cos\phi)}{R_k\sin\phi\sqrt{Z^2+r^2-2rR_k\cos\phi+R_k^2}}\right], \tag{2.21}$$

where R_k is the distance between the observation point (x,y,z) and the rotation center of the k-th curved part.

In the eq. (2.9), since the integration by ϕ can not be analytically calculated, we used a numerical approximation by Gaussian quadrature with 16th order Legendre polynomial. The magnetic flux density distribution at xy plane generated by the coil component corresponding each mesh in xz plane in Fig. 2.2 was calculated. The magnetic flux density distribution generated by the whole coil configuration is

$$B(x,y) = \sum_i \rho_i B_i(x,y), \tag{2.22}$$

where ρ_i is the density value at the i-th mesh and $B_i(x,y)$ is the magnetic flux density generated by the coil component corresponding to the i-th mesh with unit density value.
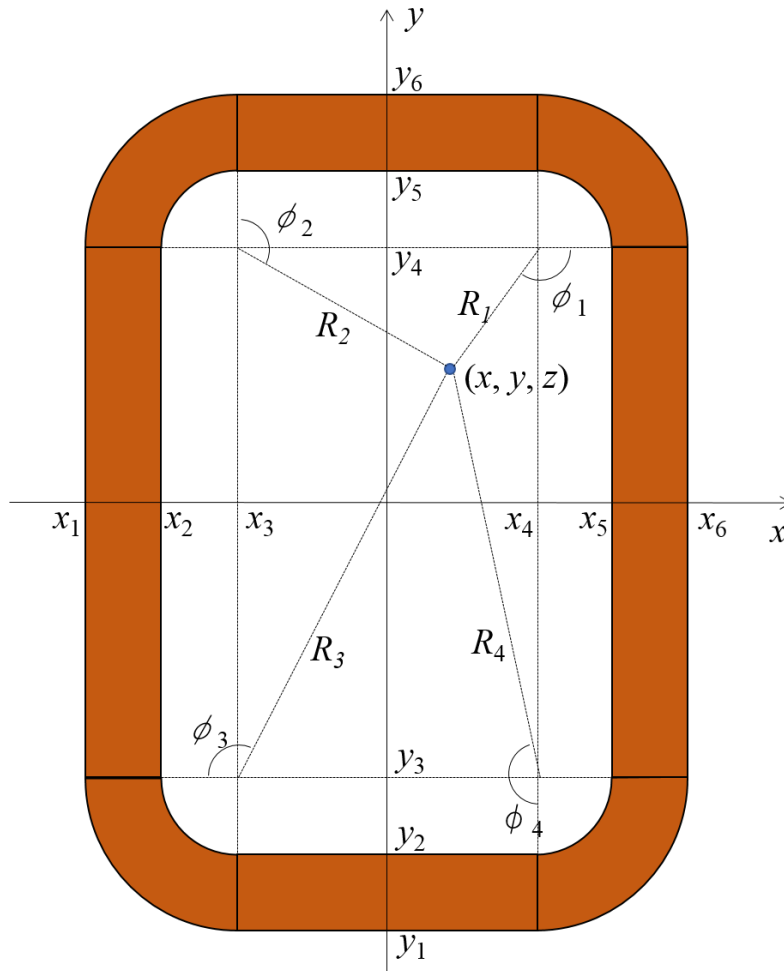
Fig. 2.4 Coil component configuration projected to xy plane

2.3.3   Results and Discussions

Filtering radius and coil shape

To evaluate the effectiveness of the proposed method, at first, the relationship between filtering radius and the obtained coil shape with the weighting factor for coil area w_3 in the objective functional set to be 0. The result is shown in Fig. 2.5 When $R_z = 1\,\text{mm}$, the filtering by PDE seemed to be not effective enough to remove the discontinuity from the solution ρ. The cross sectional shape became much smooth when R_z was larger. The material region, in which the density value rho is 1, was integrated into two or one island when $R_z \geq 15\,\text{mm}$ and when $R_z \geq 30\,\text{mm}$, respectively. When the filtering radius R_z became larger, the shape became simpler with a smooth boundary between the material region with $\rho = 1$ and the void

region with $\rho = 0$. Fig. 2.6 shows the B-L product homogeneity f_1 of the obtained solutions. Before binarization, B-L product homogeneity was the minimum at $R_z = 30\,\text{mm}$, monotonic decreasing when R_z is less than 30 mm, and slightly monotonic increasing when R_z is more than 30 mm. Filtering was introduced in order to relax the ill-posed problem and remove excessively complicated substructure, thus it basically limit the solution space. Nevertheless, the homogeneity became worth when R_z is smaller than 30 mm. We consider that there would be a lot of local minimums in the objective functional with a small value of filtering radius since a lot of solution with complicated substructure was allowed.

Binarization of the density

In this subsection we discuss the effectiveness of Heaviside function to remove grayscale from the solution. Fig. 2.7 shows the relationship between filtering radius and the ratio of the area of grayscale where ρ is intermediate value between 0 and 1 to the area of whole design domain. In the almost of all cases, except for the case with $R_z = 1\,\text{mm}$ in which the solution was discontinuous, the area of grayscale was less than half of that of the design domain. The grayscale was slightly monotonic increasing when R_z was increasing more than 30 mm, that is because the function psi was much smoothed by PDE filter when R_z is large and the area where ψ value was in the range of $-h < \psi < h$ increased.

When the real manufacturing of coil structures of these solutions, it is preferred to completely remove the grayscale because it would be difficult to be precisely realized in most cases. In this study, the value of ρ was simply binarized into 0 or 1 with the threshold of 0.5. The comparison between B-L product homogeneity f_1 before binarization and that after binarization is shown in Fig. 2.6. It was shown that the relatively good B-L product homogeneity less than 10^{-4} could be realized by the binarized density value of 0 or 1 when R_z was 30 mm or more, while the homogeneity became worth after binarization with every R_z value. Fig. 2.8 shows the magnetic flux density to z direction B_z at the origin of the coordinate, before and after binarization. The magnetic flux density before binarization became almost 3 T with every R_z values of 30 mm or more. After binarization, the values of B_z changed but the variations were almost within $\pm 1\%$, which can be adjusted by controlling the current density at the coil.

Fig. 2.9 shows the ratio of cross sectional area of the coil to the one of design domain. The value became stable at around 20 % when R_z is 30 mm or more and there was almost no difference between before and after binarization. We confirmed that the proposed method

with Heaviside function projection can suppress grayscale while keeping the continuous density function with a minimum performance disruption after binarization.
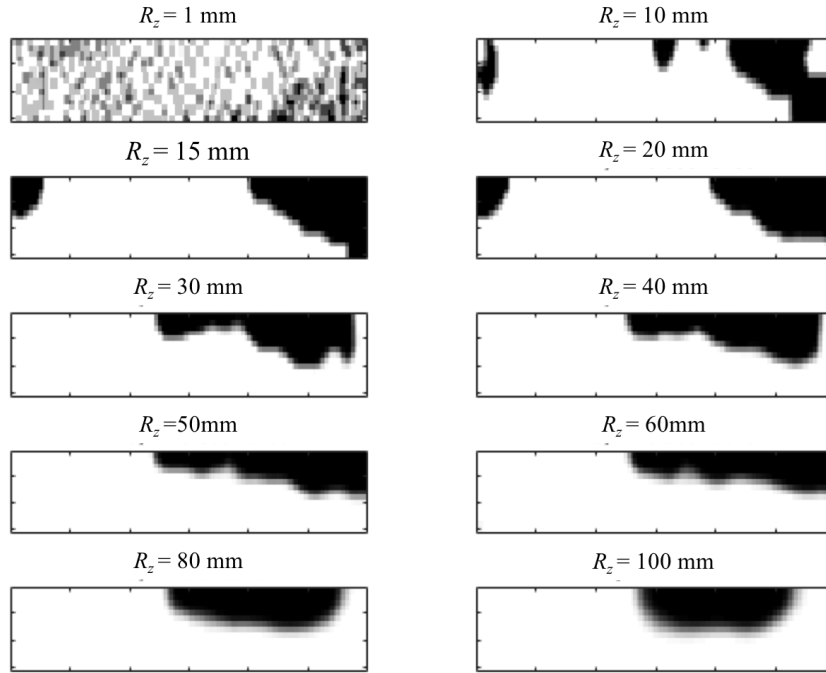
Fig. 2.5 Filtering radius dependence of optimal configuration with $w_3 = 0$

Cross sectional area term in the objective functional

To reduce an amount of superconducting cable, the third term with a weight coefficient w_3 in the objective functional of Eq. (2.5) , which is for the cross sectional area, was introduced. Fig. 2.10 and Fig. 2.11 is the cross section shape of the obtained solution with $w_3 = 0.0027$ and $w_3 = 0.0091$, respectively. They showed the same trends to the case of $w_3 = 0$ in Fig. 2.5 that the discontinuity of the solution was removed and the boundary shape became simple when the filtering radius became large. Fig. 2.12 (a) and (b) shows the B-L product homogeneity before/after binarization with $w_3 = 0.0027$ and $w_3 = 0.0091$, respectively. They also show the same trends that the values before binarization became stable when R_z is 30 mm or larger.
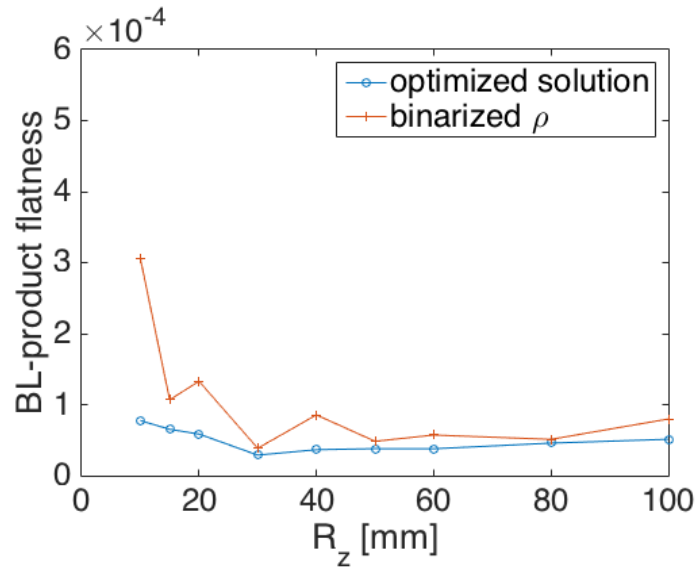
Fig. 2.6 Filtering radius dependence of BL-product flatness before/after binarization
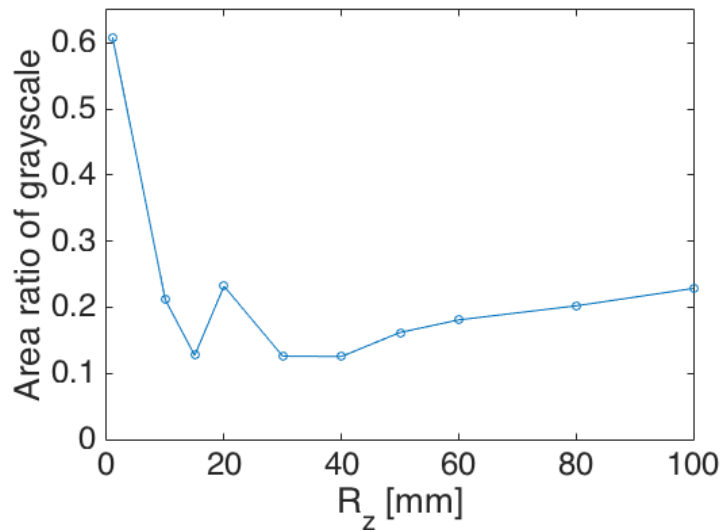
Fig. 2.7 Filtering radius dependence of area ratio of grayscale in ρ

B-L product homogeneity after binarization at $R_z = 30\,\text{mm}$ was around 6×10^{-5} and 2×2^{-4}, when $w_3 = 0.0027$ and $w_3 = 0.0091$, respectively. Though these values were worse than one with $w_3 = 0$, each values after binarization was less than twice of one before binarization and satisfied the target of within 0.1%. Fig. 2.13 (a) and (b) shows the ratio of the coil cross sectional area to the desing domain with $w_3 = 0.0027$ and $w_3 = 0.0091$,
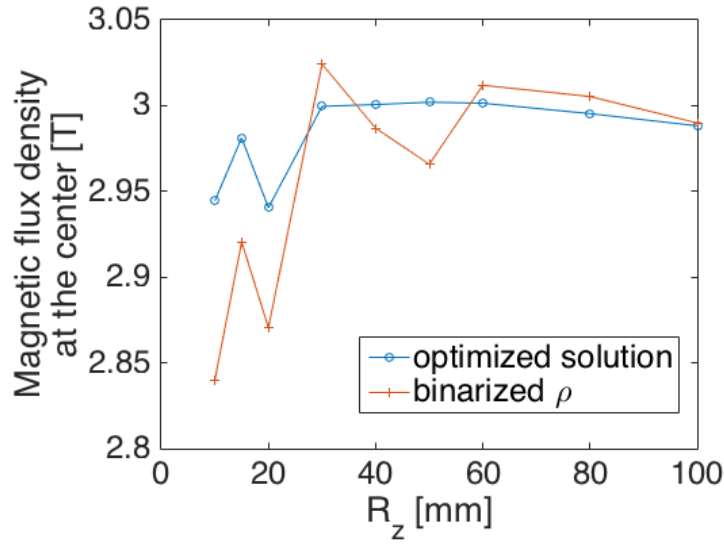
Fig. 2.8 Filtering radius dependence of magnetic flux density at the center before/after binarization
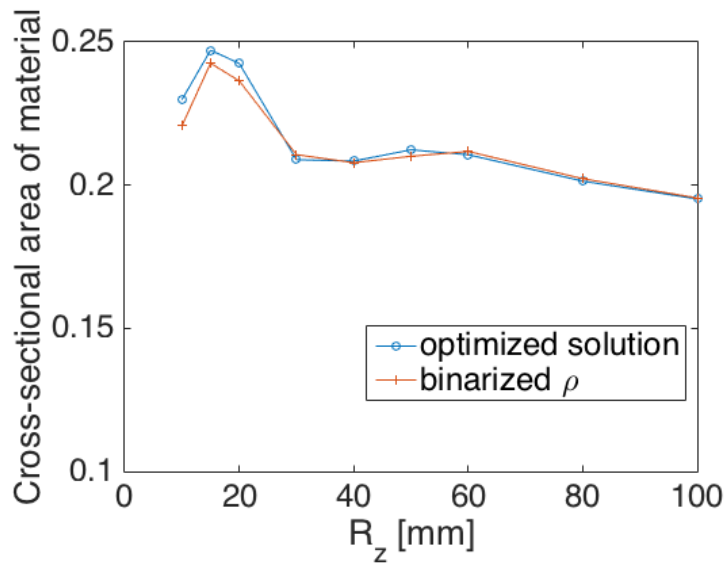
Fig. 2.9 Filtering radius dependence of cross-sectional area ratio of the material before/after binarization

respectively, where no significant change between before and after binarization, as similar to the case with $w_3 = 0$. when R_z is 30 mm or more, the ratio became stable around 0.19 and 0.14, with $w_3 = 0.0027$ and $w_3 = 0.0091$, respectively, and these values were smaller than one with $w_3 = 0$.

As discussed above, we confirmed a trade-off relationship between the B-L product homogeneity and coil cross sectional area by controlling w_3 value. This fact means that the weighting factor in the objective functional works correctly.

In comparison of Fig. 2.5 to Fig. 2.10 and 2.11 at the same filtering radius R_z, the center of gravity of the coil cross section moved to the negative direction along x axis with increasing w_3. we consider this trend is because of the second term in the objective functional, which works to enclose the magnetic flux density at the origin to the target value, i.e., the contribution of an unit area of cross section to generate magnetic flux becomes large when the cross section locates close to the origin.

Fig. 2.14 shows the number of islands that each coil cross section consist of. The number of islands decreased with the increase of filtering radius and the simplification of the boundary shape, and this trends are common in every w_3 values. With these result, we confirmed that the proposed method can control the shape complexity of the solution by changing the filtering radius independent of setting of the objective functional.

$R_z = 1$ mm $R_z = 10$ mm $R_z = 15$ mm $R_z = 20$ mm $R_z = 30$ mm $R_z = 40$ mm $R_z = 50$mm $R_z = 60$mm $R_z = 80$ mm $R_z = 100$ mm
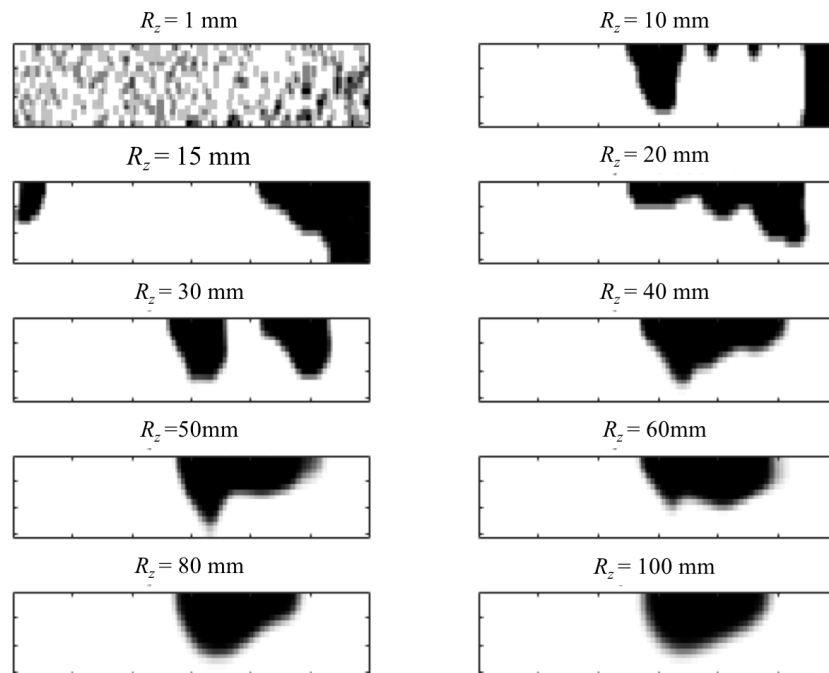
Fig. 2.10 Filtering radius dependence of optimal configuration with $w_3 = 0.0027$
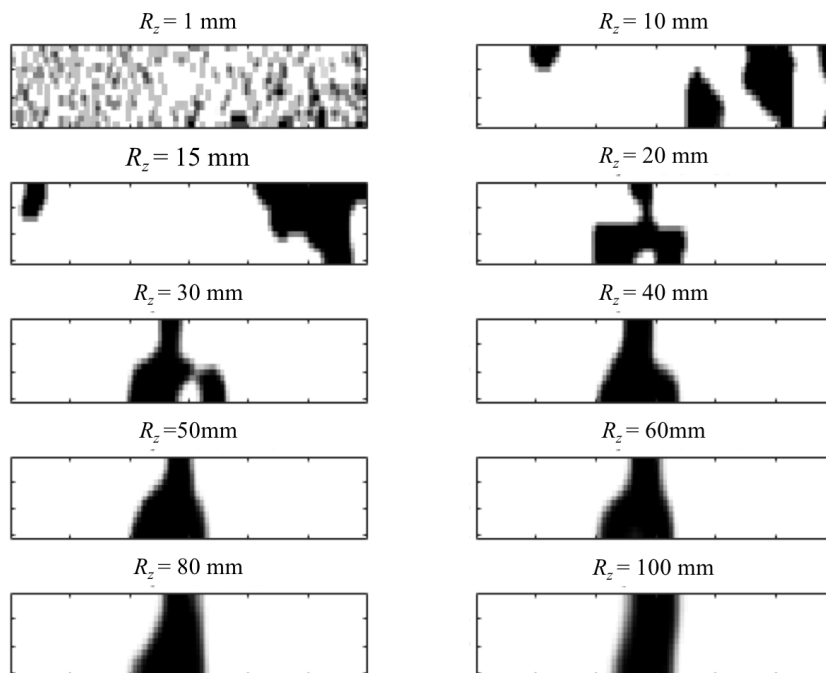
Fig. 2.11 Filtering radius dependence of optimal configuration with $w_3 = 0.0091$
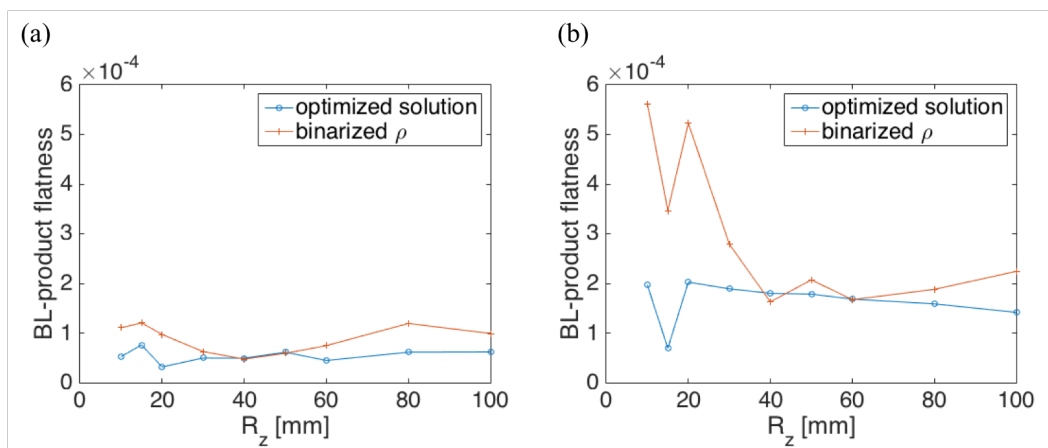
Fig. 2.12 Filtering radius dependence of BL-product flatness with (a) $w_3 = 0.0027$ (b) $w_3 = 0.0091$
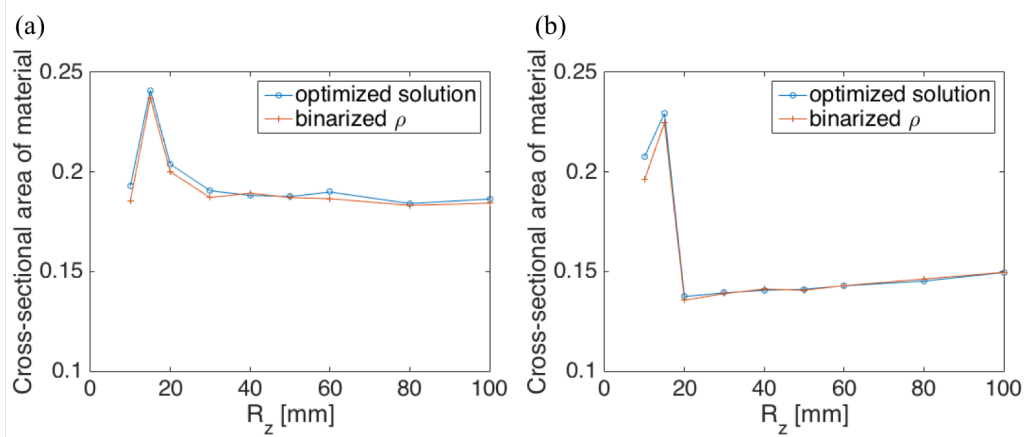
Fig. 2.13 Filtering radius dependence of cross-sectional area ratio of the material with (a) $w_3 = 0.0027$ (b) $w_3 = 0.0091$
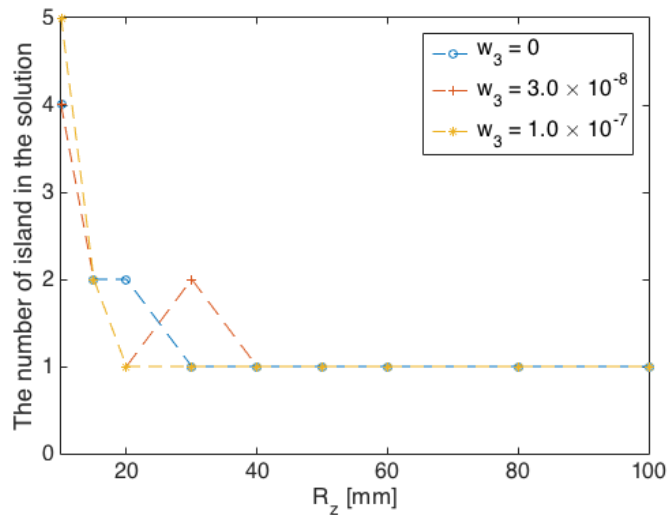
Fig. 2.14 Filtering radius dependence of the number of islands in the solution

2.4 Summary and future works

In this study, We developed a topology optimization method for superconducting electromagnets in particle accelerators, by using PDE filtering based on Heaviside function projection. We summarize the conclusion as follows.

(1) We set three requirements in designing the superconducting magnet coils for particle accelerators; B-L product homogeneity, flux density at the center and coil cross sectional area. We formulated three objective functionals corresponding to each requirement,

and defined a multi-objective optimization problem with weighted summation method to obtain the optimal solution which satisfy all the requirements.

(2) An optimization algorithm was developed to solve above problem using PDE filtering and Heaviside projection method in order to remove grayscale and excessively complicated substructures.

(3) We estimated the effectiveness of the proposed method by applying to a coil optimization problem. As a result, we obtained a coil configuration which satisfied all the requirements. We also confirmed that the performance degradation was small when the grayscale was completely binarized, and that the complexity of the solution was controlled by setting an appropriate filtering radius.

In this study, we set an objective functional considering magnetic flux distribution and material cost. When applying to real manufacturing, we should further consider the decrease of critical current density and electromagnetic stress because of the magnetic field the cable experiences. Noguchi et al[74] solved parameter optimization problem of the cross sectional shape for SMES coil designing under constraints of critical current density and Lorentz force at the cable. We believe we can obtain a higher performance coil configuration with manufacturability, by combining our proposed method.

Chapter 3

Robust Optimization for Layer-stacking Method Considering Patient Motion

The layer-stacking method can provide three-dimensional conformal dose distributions to the target based on a passive scattering method using mini-spread-out Bragg peak (SOBP). The purpose of this work is to demonstrate the effectiveness of a new weight optimization algorithm that can enhance the robustness of dose distributions against layer depth variation in layer-stacking proton beam therapy. In the robustness algorithm, the upper limit of the layer's weight was adapted to the conventional algorithm and varied for 620 weight set evaluations. The optimal weight set was selected by using an analytical objective function based on Gaussian function with $\sigma = 3$mm for WED variation. Then, we evaluated the stabilities of the one-dimensional depth dose distribution against WED variation generated by Gaussian samples. Three-dimensional dose distributions in the water phantom were also evaluated using the Monte-Carlo dose calculation. The variation of dose as well as dose volume histograms for the spherical target and the organ at risk (OAR) were evaluated. The robustness algorithm reduced the change of the dose distribution due to the WED variation by a factor of almost 3/4 compared to those with the conventional procedure. The rate of 91.8% in total samples was maintained within 5% change of the maximum dose, compared with the rate of 64.9% in the conventional algorithm. In the MC calculation, the high dose-volume in the OAR was reduced around the lateral penumbra and distal falloff region by the robustness algorithm. The stability of depth dose distributions was enhanced under the WED variation, compared to the conventional algorithm. This robust algorithm in layer-stacking proton therapy may be useful for treatment in which the sharpness of the distal falloff along the depth

distribution needs to be maintained to spare the organ at risk and keep the dose coverage for the target tumor.

3.1   Introduction

Particle beam therapy can provide a better conformal dose distribution than that with photon therapy and can spare healthy tissue around the tumor [26, 77]. Based on this idea, a passive irradiation method was first adapted to particle therapy as a two-dimensional irradiation technique. In this method, the particle beams are laterally broadened by a pair of wobbler magnets and scatterers, and the primary Bragg peaks are longitudinally broadened to form a spread-out Bragg peak (SOBP) using a range modulator or a ridge filter. A range compensator is used to match the dose distribution to the distal shape of the target volume, and a multi-leaf collimator (MLC) or a patient specific collimator forms the beam shape laterally. This method was used safely in treatment with fixed targets as well as those exhibiting respiration motion practically. However, unnecessary dose to the normal tissue located proximal to the target is unavoidable in the single field because the size of the SOBP is fixed to the longitudinal size of the target. Recently, a beam scanning method has become the mainstream as a three-dimensional irradiation technique, and it can reduce the unnecessary dose to the normal tissue. A more conformal dose distribution can be formed to even a complicated target shape compared with the distribution in the passive method. This method can be applied safely when the static condition of the irradiated region for the patient is maintained within expected setup uncertainties and internal motion. However, the interplay effect violating the dose distribution due to patient motion is still a problem [78]. Methods to maintain the robustness of the planned dose distribution against range and setup uncertainties have been reported [79]. The layer-stacking method has been developed as a three-dimensional irradiation technique based on the passive method [29, 30]. In this method, the target is separated into layers along the depth direction, and a certain amount of dose to each layer volume is delivered by uniform distributions with the smaller size of SOBP by changing the beam energy. Simultaneously, the aperture size of a multi-leaf collimator (MLC) is changed for each layer step-by-step. As a result, three-dimensional uniform dose distribution over the target volume can be formed by modulating the weighting factor of dose irradiation for each layer [31], and unnecessary dose to normal tissue proximal to the target is suppressed in a similar way to the scanning method. To obtain optimum weight for each layer, an iterative

algorithm which can consider the change of aperture size were developed [31]. In the layer stacking method, a single layer is almost simultaneously irradiated by the uniform dose distribution using wobbling magnets or double scatterers, and the irradiation time for a single layer is typically a few seconds or more. In the same way as the passive method, patient motion during a single layer irradiation causes no dose variation. Thus, the dose distribution in the layer-stacking method should have less sensitivity to the motion uncertainties than that in the scanning method. Nevertheless, the motion uncertainties relative to the beam direction among adjacent layer irradiations induces the variation of the water equivalent depth (WED), that causes the disturbance in the summed dose distribution from that planned [78]. A simple approach for this problem is to use the depth-dose distribution with a broadened Bragg peak rather than the mono-energetic one, which is called a "mini-spread out Bragg peak" (mini-SOBP), and is generated by the use of a mini ridge filter (mini RGF) designed for this purpose. Schaffner et al studied the robustness against beam range error in layer-stacking irradiation and discussed its dependence on the mini RGF design. [46] However, one should note that the more broadening mini-SOBP loses the sharpness of the dose distribution around the distal falloff and leads to increases of unnecessary dosage on organs at risk located behind the target. In this report, we propose a novel algorithm for determining layer weightings in the layer-stacking method, which can enhance the robustness against WED variation of layers, without over-broadening of mini-SOBP.

3.2   Materials and Methods

3.2.1   One-dimensional dose calculation

In actual treatment planning, dose distributions around planning target volumes (PTVs) on patient CT images are calculated three-dimensionally. Layer-stacking irradiation provides more conformal dose distributions to the PTV using a pair of wobbling magnets, scatterers, MLC, and mini-RGF. The mini-RGF forms a mini-SOBP with a length of about 10 mm. In this irradiation, the PTV is subdivided into several layer volumes along the beam direction, and the dose at each layer volume is delivered step-by-step with a small SOBP by changing the thickness of the energy degrader and the aperture shape of the MLC simultaneously. A relative dose-weighting factor for each layer volume is determined to produce a uniform dose distribution over the PTV while trimming out a higher dose in front of the target at last. However, since each layer volume is irradiated sequentially changing the degrader thickness

with constant steps, the variation of WED from the skin surface to the distal side of each layer volume during irradiation may disturb dose uniformity in actual treatment. This inter-layer WED variation is a specific phenomenon to the layer-stacking method and not occurs in the conventional passive method, where three-dimensional target is irradiated almost simultaneously. In the following, we discuss a weight optimization algorithm producing dose distributions with robustness against variations of the WED based on one-dimensional depth dose distribution. In the layer-stacking irradiation, the summed depth dose distribution over the whole PTV, $D_{SOBP}(z)$, on a one-dimensional basis is expressed by,

$$D_{SOBP}(z) = \sum_{i=1}^{n} \chi_i d_i(z), \tag{3.1}$$

where z, $d_i(z)$ and χ_i shows penetration depth, depth dose distribution with the mini-SOBP, and the weight value for i-th layer, respectively, and n denotes the number of all layers. Assuming the equivalence on the shape of $d_i(z)$ among all layers, $d_i(z)$ can be rewritten by the depth dose distribution of the first element as

$$d_i(z) = d_1(z + l(i-1)), \tag{3.2}$$

where l shows the WED corresponding to constant step size of the energy degrader and was set to be 5 mm.

3.2.2   Mini-SOBP distributions used in the model simulation

The simulated condition was on a one-dimensional basis, where the size of the PTV along a beam direction was around 100 mm water equivalent length (WEL) and the distal edge of the PTV was located at around 125 mm depth in water. In this case, 150 MeV proton beam energy was practically used in a proton therapy facility based on the passive scattering method, and the corresponding SOBP length of the summed depth dose distribution was set to be around 100 mm. The depth dose distributions of the mini-SOBP used in this work were designed for the layer-stacking system (Hitachi, Ltd., Tokyo, Japan) installed at Fukui Prefectural Hospital Proton Therapy Center (FPHPTC), and are shown in Fig. 3.1. The corresponding characteristic parameters are also listed in Table 3.1. These mini-SOBP distributions demonstrated the difference of the sharpness, in particular, on the length of the distal falloff. Types A and C show the sharpest and mildest distribution, respectively, and type B was in the middle between them. In the actual treatment at the proton therapy center,

the mini-SOBP distribution of type A has been used since 2014 for static targets, mostly head and neck cancer.
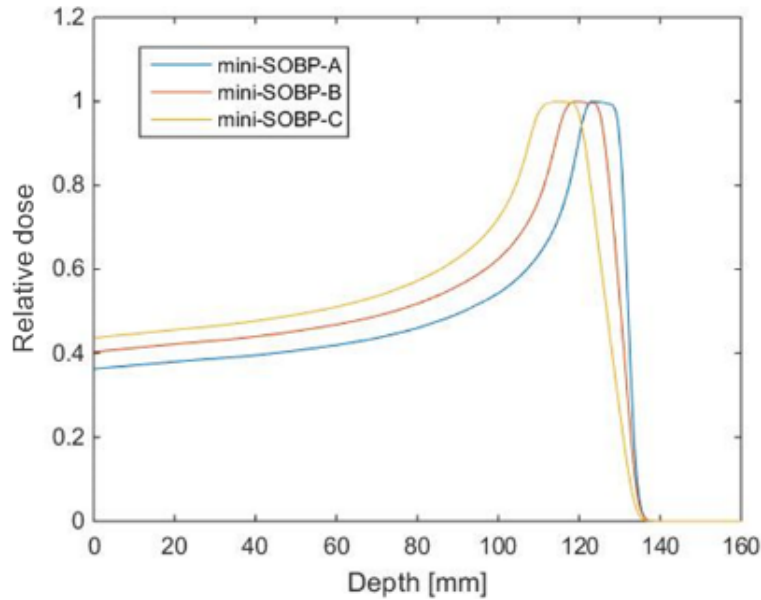
Fig. 3.1 Depth dose distributions of the mini-SOBP used for layer-stacking irradiation.

Table 3.1 Characteristic parameters for each mini-SOBP distribution shown in Fig. 3.1.

	Mini-SOBP A	Mini-SOBP B	Mini-SOBP C
SOBP length [mm]	10.3	12.1	13.8
Distal falloff [mm]	2.7	5.3	8.5

3.2.3 Weight optimization algorithms

As discussed in the reference [46], weight values of all layers calculated by an optimization method were principally classified into two groups. In the first group, a few layers contribute to the summed dose distribution showing a steeper gradient around the distal falloff region, while those in the second group contribute to more uniform distribution. Weight values of the layers in the second group are almost balanced with each other; however, the values in the first group are larger and tend to show more variation than of layers in the second group.

The layer with a larger weight value has a risk of strongly deteriorating the uniformity of the summed dose distribution when the WED in the corresponding layer volume changes relative to the one in other layers. Thus, balancing weight values among layers might be effective to maintain the robustness of the dose uniformity against the WED variation. Here, we propose a new robust weight optimization algorithm for layer-stacking irradiation by introducing two parameters, X_a and X_b, to limit the maximum of the weight value of layers classified into the first and second group, respectively, as follows,

$$\begin{cases} X_i^{\text{MAX}} = X_a, & i = 1, 2, \\ X_i^{\text{MAX}} = X_b, & i \leq 3, \end{cases} \tag{3.3}$$

where i shows the layer number and the 1st layer corresponds to the layer volume at the most distal side of the PTV. In the weight optimization algorithm, the maximum limiting values were varied according to the following conditions,

$$\begin{cases} X_a = 0.4 + 0.02 n_a, & n_a = 0, 1, 2, \cdots, 30, \\ X_b = 0.02 n_b, & n_b = 1, 2, 3, \cdots, 20, \end{cases} \tag{3.4}$$

Here, the weight value for each layer is defined as a ratio of peak value of depth dose distribution of the layer to objective dose. Ranges of X_a and X_b were set to be 0.4 - 1.0 and 0.02 - 0.4, respectively, with a constant step of 0.02. The algorithm could find the best set of weight values within 620 (31×20) combinations between X_a and X_b based on an objective function for the robustness of the summed dose distribution against the relative WED variation. Fig. 3.2 shows the flow of the optimization algorithm, and the objective function is discussed in the next section. The weight values of all layers under the maximum limitation were iteratively updated by the following,

$$\chi_i \rightarrow \frac{D^{\text{obj}} \sum_{j=1}^{m} d_i(z_j)^2}{\sum_{j=1}^{m} D_{\text{SOBP}}(z_j) d_i(z_j)^2} \chi_i, \tag{3.5}$$

$$\text{if} \chi_i > X_i^{\text{MAX}}, \chi_i \rightarrow X_i^{\text{MAX}}, \tag{3.6}$$

where z_j shows the depth of dose evaluation point which is discretized with a step size of 1 mm, and the set of z_j with $j = 1, \cdots, m$ covers the depth region over the PTV. Since the width of mini-SOBPs are 10 mm or more as in Table 3.1, the evaluation points are located enough dense not only on the peak depths of mini-SOBP but also between peaks. D^{obj}

shows the objective dose of the optimization and is set to be 1 in this work. We assume the prescribed dose also equals to 1, and discuss the dose distribution on the relative dose bases. Weight values of all layers were calculated according to Eq. (3.5) by an iterative procedure [31] under the constraint of Eq. (3.6) which is newly introduced in this work, and the set of converged weight values was determined after 10,000 iterations.
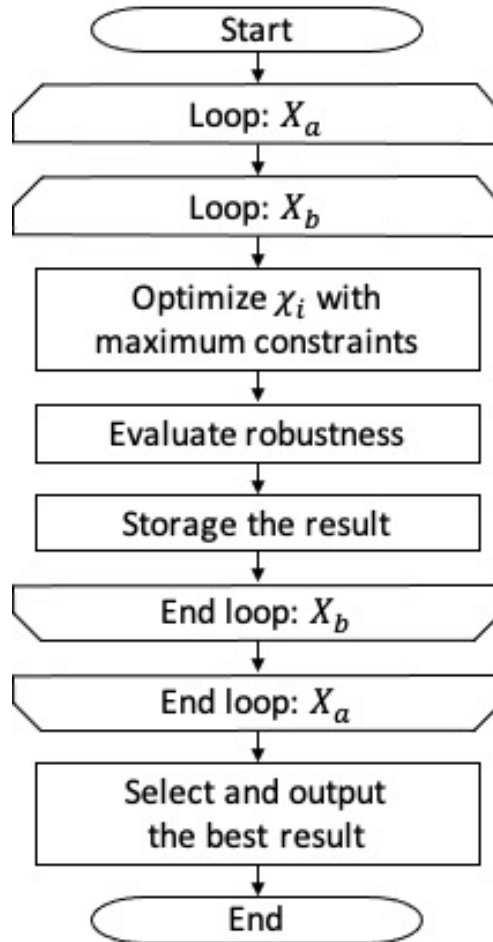
Fig. 3.2 Flowchart of the developed robustness algorithm.

3.2.4   Selection for appropriate sets of X_a and X_b values

After the optimization over 620 sets of X_a and X_b values, appropriate sets were selected by the following conditions: dose uniformity < 0.025, SOBP length > the one with conventional algorithm - 5 mm and distal falloff < the one with conventional algorithm + 1.5 mm, where the distal falloff corresponds to the depth distance between the relative dose of 0.8 and 0.2

to the objective dose at the distal side, whereas SOBP length corresponds to the distance between the proximal and distal side with the relative dose of 0.95. Dose uniformity u is defined by

$$u = \max_{z \in \Omega} \frac{|D_{\text{SOBP}}(z) - D^{\text{obj}}|}{D^{\text{obj}}}, \qquad (3.7)$$

where Ω shows an evaluation region along the depth, and is defined by the depth region between $2\sigma_{\text{shift}}$ inside of both of the proximal and distal side of the SOBP region. Here, σ_{shift} corresponds to one standard deviation of assumed WED variation and was set to 3 mm for the generation of the optimum weight values based on the robustness algorithm. Since D^{obj} is 1 in this work, u is just the maximum dose difference from 1 within the evaluation area. The schematic depth-dose curve is shown in Fig. 3.3 (a) to demonstrate the corresponding parameters discussed above.
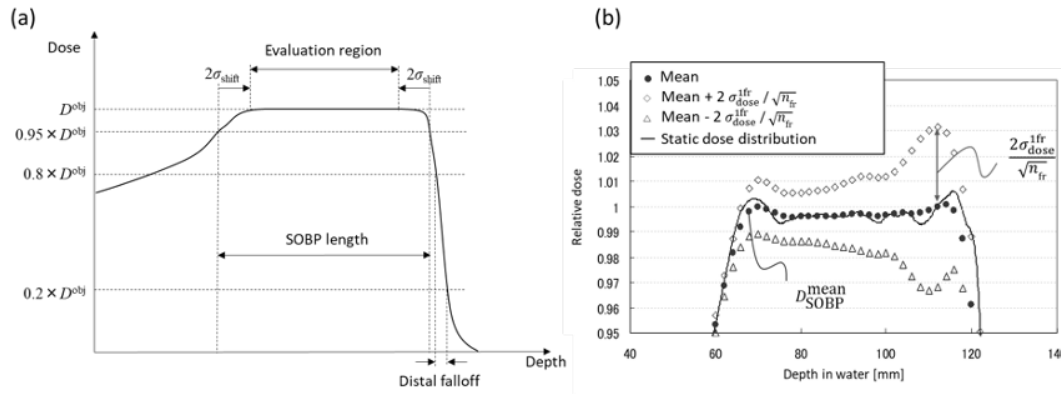
Fig. 3.3 Schematic depth-dose curve with dosimetric parameters (a) and the definition of parameter used in $R(w)$ expressed by Eq. (3.8) (b).

3.2.5 An objective function for the robustness

We introduced the following function evaluating the robustness of summed dose uniformity against WED variations,

$$R(\chi) = \max_{z \in \Omega} \left(\max_{+,-} \left| D_{\text{SOBP}}^{\text{mean}}(z) \pm \frac{2.0 \times \sigma_{\text{dose}}^{\text{1fr}}(z)}{\sqrt{N_{fr}}} - D^{\text{obj}} \right| \right), \qquad (3.8)$$

where D^{obj} shows the objective dose value and N_{fr} shows the number of fractions. $R(\chi)$ is defined as a function of one set of weight values and the robustness is stronger as $R(\chi)$ shows smaller values. Following functions used in above Eq. (3.8) are defined by

$$D_{\text{SOBP}}^{\text{mean}}(z) = \frac{1}{N} \sum_{j=1}^{N} D_{\text{SOBP}}^{j}(z), \tag{3.9}$$

$$\sigma_{\text{dose}}^{\text{1fr}}(z) = \sqrt{\frac{1}{N-1} \sum_{j=1}^{N} \left(D_{\text{SOBP}}^{j}(z) - D_{\text{SOBP}}^{\text{mean}}(z) \right)^2}, \tag{3.10}$$

where j denotes one event in which the WED of each layer were varied independently based on a probability distribution, and N shows the total number of events. One can consider $D_{\text{SOBP}}^{\text{mean}}(z)$ and $\sigma_{\text{dose}}^{\text{1fr}}(z)$ as the mean and standard deviation among $D_{\text{SOBP}}^{j}(z)$ samples, respectively, in random samples, as shown in Fig. 3.3 (b). In this work, we analytically evaluated the function of Eqs. (3.9) and (3.10) using Gaussian distribution accounting for the WED variation, since the computational time can be reduced in comparison to the one of random evaluation. In this way, Eqs. (3.9) and (3.10) can be rewritten by

$$D_{\text{SOBP}}^{\text{mean}}(z) = \sum_{i=1}^{n} \chi_i \int_{-\infty}^{+\infty} d_i(z - z') G(z') dz', \tag{3.11}$$

$$\sigma_{\text{dose}}^{\text{1fr}}(z) = \left[\sum_{i=1}^{n} \chi_i^2 \left\{ \int_{-\infty}^{+\infty} d_i(z - z')^2 G(z') dz' - \left(\int_{-\infty}^{+\infty} d_i(z - z') G(z') dz' \right)^2 \right\} \right]^{\frac{1}{2}}, \tag{3.12}$$

where $G(z') = \frac{1}{\sqrt{2\pi}\sigma} \exp(-\frac{z'^2}{2\sigma_{\text{shift}}^2})$ corresponding to Gaussian distribution with $\sigma_{\text{shift}} = 3$ mm was used commonly for all layers and the analytical evaluation of above equations is described in supplementary materials.

3.2.6 Validation of the robustness algorithm in one dimension

The robustness algorithm for three mini-SOBP distributions was tested by calculating the summed depth dose distributions with random variations of WED for each layer. Optimized weight values were obtained by the robustness algorithm with the constant value of σ_{shift} = 3 and used for the evaluation of the depth dose variation using random samples, where 10,000 random sets of depth dose distributions with and without the robustness condition

were generated respectively with WED variations by means of Gaussian probability density functions with sigma of 3 mm and 5 mm. The dose uniformity was compared between them, and the fraction number of N_{fr} was set to be 20 to simulate actual fractionated irradiations.

3.2.7   Validation of the robustness algorithm in three dimensions

The robustness algorithm was also tested on a three-dimensional basis using Monte Carlo simulations developed for the dose verification system at FPHPTC [80]. The setting for wobbling radius, the material geometry of mini-RGF of type A, and the range-shifter thickness corresponding to the depth of the slice were taken into account according to the planning parameters generated by the RTP system. The bolus and the aperture shape of the MLC opening were also designed by the RTP system assuming a spherical target with a diameter of 60 mm, and the center of the target was placed at the depth of 90 mm in the uniformed water phantom. The smearing distance of the bolus was set to be 6 mm. Three-dimensional dose distributions of each layer were calculated with the voxel size of $2 \times 2 \times 2 \text{mm}^3$ within statistical uncertainty of 0.5% along depth direction, and were summed up with the weights of the conventional and the robust algorithm by considering the positional errors among slices. The dose distributions of each slice in both algorithms were randomly shifted along perpendicular directions to the beam direction using two dimensional Gaussian distribution with σ_{shift} =3 mm. In this case, the proton range variation was generated by the variation of the bolus thickness due to the positional error of the target, while the error along the depth direction was not included because of the uniformity of the phantom. The dose volume histograms (DVH) for the spherical target and OAR were evaluated by these simulations, where the volume of OAR was placed surrounding the distal side of the target with the surface distance of 8 mm as shown in Fig. 3.4.

3.3   Results

3.3.1   Selection of the best solution

Fig. 3.5 (a), (b), (c), and (d) shows the value of the dose uniformity, SOBP length, distal falloff, and R(w) values defined in Eq. (3.8), respectively, over 620 sets of X_a and X_b in the case of the mini-SOBP of type B. In these figures, the dose uniformity (a) became within 2.5 percent over almost of (X_a, X_b) plane, although it became worse when X_b was small. SOBP
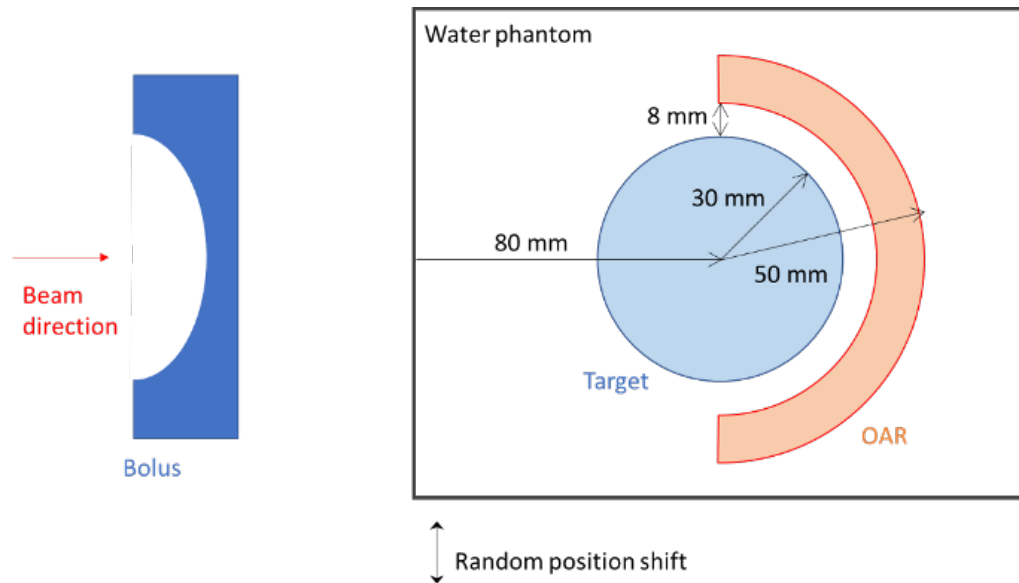
Fig. 3.4 The schematic of geometry settings of water phantom, bolus, target, and OAR for the Monte Carlo calculation.

length (b) almost always exceeded 100 mm except when X_a was smaller than 0.46. Distal falloff (c) showed a significant negative correlation with X_a and exceeded the appropriate condition with a small value of X_a. Within appropriate solutions maintaining the conditions of dose uniformity, SOBP length and distal falloff, a pair of X_a and X_b values were searched with the smallest value of $R(w)$ shown in Fig. 3.5 (d), and the selected value of X_a and X_b was 0.48 and 0.14, respectively, with $R(w) = 0.032$. In the conventional algorithm where $(X_a, X_b) = (1.0, 1.0)$, $R(w)$ value was found to be 0.041 and is larger than that in the robustness algorithm.

3.3.2   Comparison between conventional and robust solutions

Fig. 3.6 (a) shows a comparison between the weight values optimized by means of the conventional algorithm and the developed robustness algorithm, respectively in the case of type B. The weight value of the 1st layer was significantly larger than those of the other layers in the conventional result, while the weight values of the 1st and 2nd layer were approximately the same in the robustness algorithm. The weight value of the 3rd to the 9th layer also had differences in between those of the conventional and the robustness algorithm although the weight values of 10th and subsequent layers were similar. Fig. 3.6 (b) shows the depth dose distributions calculated by the optimized weight values in the case of type B. The
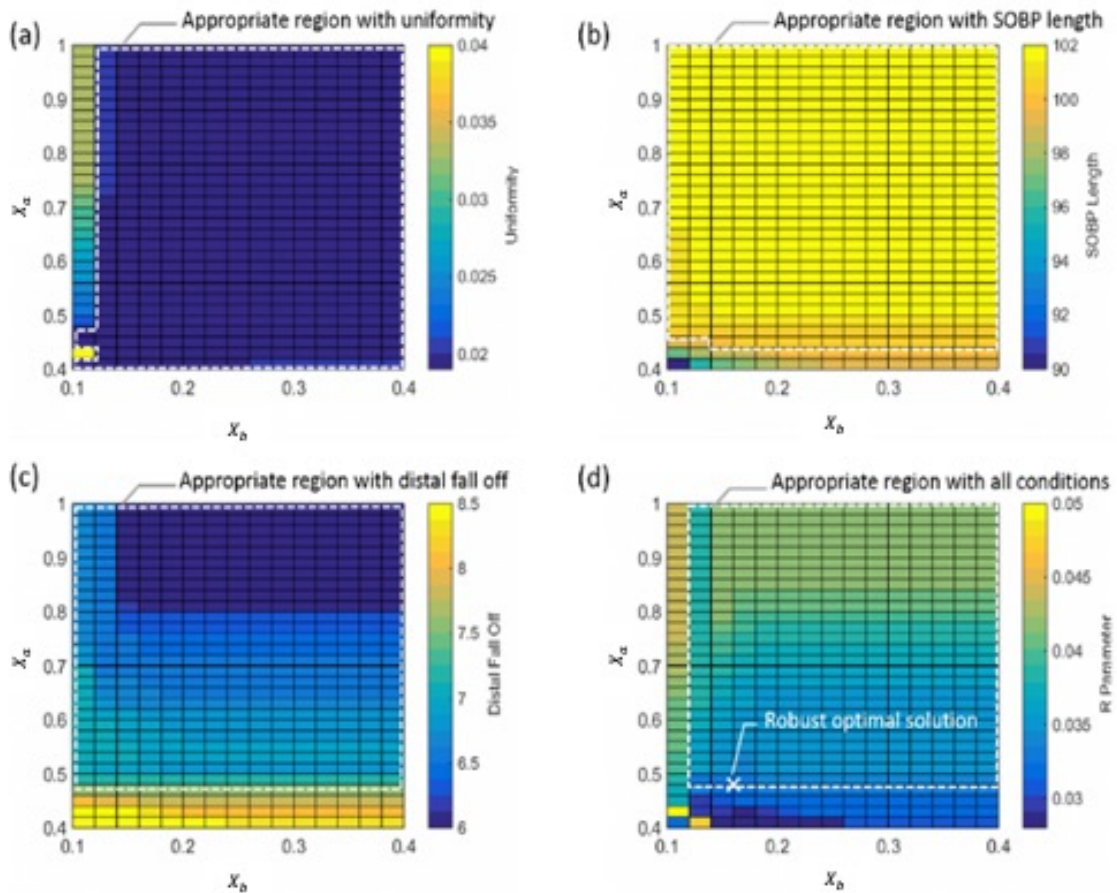
Fig. 3.5 The value of dose uniformity (a), SOBP length (b), distal falloff (c) and R parameter (d) over the (Wa, Wb) plane in the case of the mini-SOBP of type B. Areas surrounded by white dashed lines in each variable show the appropriate region.

objective dose was normalized to unity in this figure. Their corresponding dose uniformity, distal falloff and SOBP length are also summarized for the static condition in Table 3.2. Dose uniformity was maintained within 2%. Distal falloff was 6.1 mm and 7.2 mm with the conventional result and the robust result, respectively, thus a slight degeneration in distal falloff was shown with the robustness algorithm. Similarly, SOBP length was 102.8 mm and 100.9 mm with the conventional result and the robust result, respectively.

3.3.3   Robustness simulation under WED variation in one dimensional basis

Fig. 3.7 shows the mean, maximum, and minimum values of the total dose distribution through 20 fractions, in which the WED was varied randomly for each slice each fraction
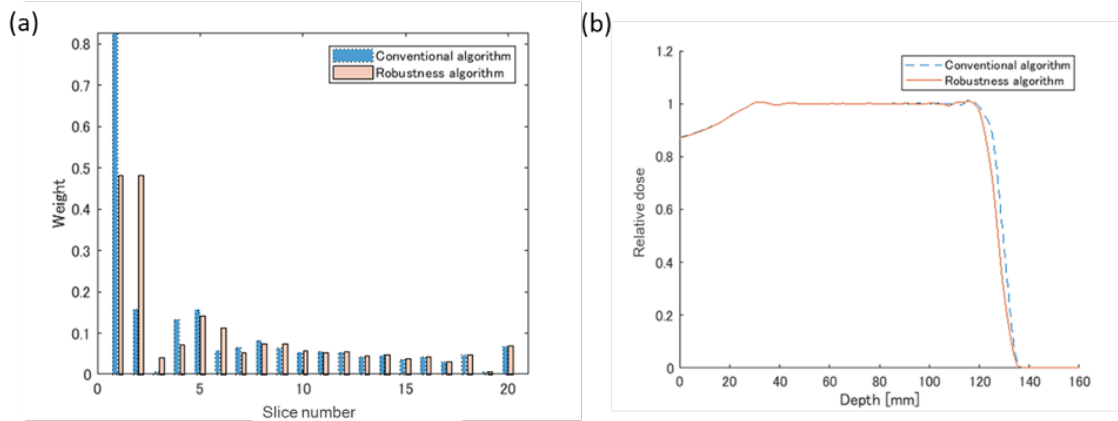
Fig. 3.6 The weight values (a) and the depth dose distributions (b) optimized with the conventional algorithm and the robustness algorithm in the case of the mini-SOBP of type B.

with σ_{shift} =3 mm. The presented calculation was carried out using the mini-SOBP of type B. The mean dose distribution with the robustness algorithm was almost equivalent to that with the conventional algorithm except for the distal edge region. On the other hand, the maximum and minimum dose over 10,000 random events were also close to the objective dose with the robustness algorithm, compared with the conventional algorithm, at around 110 mm depth. Dose uniformity, distal falloff and SOBP length under the variation of WED are also summarized in Table 3.2.

Table 3.2 Dose uniformity, distal falloff and SOBP length of the optimized depth dose distribution in the case of the mini-SOBP of type B. The definition of these characteristic parameters is described in the text.

		Dose uniformity [%]	Distal falloff (80%-20%) [mm]	SOBP length (95%-95%) [mm]	Distal side depth of 95% dose [mm]
Conven-	Static	1.9	6.1	102.8	122.6
tional	WED variation	2.4 (0.8)	7.8 (0.6)	101.6 (1.1)	121.4 (1.1)
Robust-	Static	1.9	7.2	100.9	120.8
ness	WED variation	2.2 (0.5)	8.6 (0.6)	99.4 (0.8)	119.3 (0.8)

Table 3.2 footnote: Values outside and inside parentheses show the average and standard deviation, respectively.
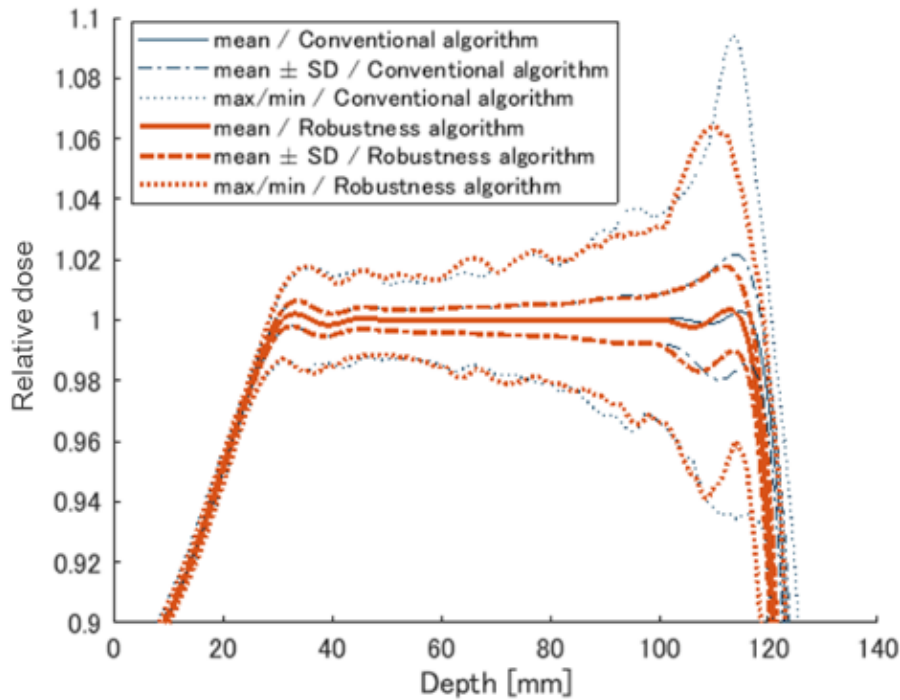
Fig. 3.7 The mean, maximum and minimum value of depth dose distribution under WED variation for each slice with σ_{shift} =3 mm in the case of the mini-SOBP of type B.

Next, we estimated the maximum dose difference between the static dose distribution without WED variation and the disturbed dose distribution with WED variation, within the evaluation region, over each entry of 10,000 random samples. Fig. 3.8 shows the results for each of three mini-SOBPs with the WED variation of 3 mm and 5 mm. Compared with the conventional algorithm, all results with the robustness algorithm show smaller peak value and smaller peak width. The mean value of the maximum dose difference with the robustness algorithm was 0.033, 0.020 and 0.016, though that with the conventional algorithm was 0.046, 0.026 and 0.022 for the mini-SOBP of type A, B and C, for the WED variation of 3 mm. Table 3.3 shows the path rate so that the maximum dose difference between the static dose distribution and the disturbed dose distribution within the evaluation region was within 5% and 10,000 random samples were analyzed for each of the WED variations of 3 mm and 5 mm. The analyses showed that the rate with a WED variation of 3 mm was in the range of 91.8-100% and improved in comparison to the rate of 64.9-99.2% in the conventional procedure and the robustness algorithm was found to be most effective in the mini-SOBP of type A, which has the sharpest distal falloff among the three.
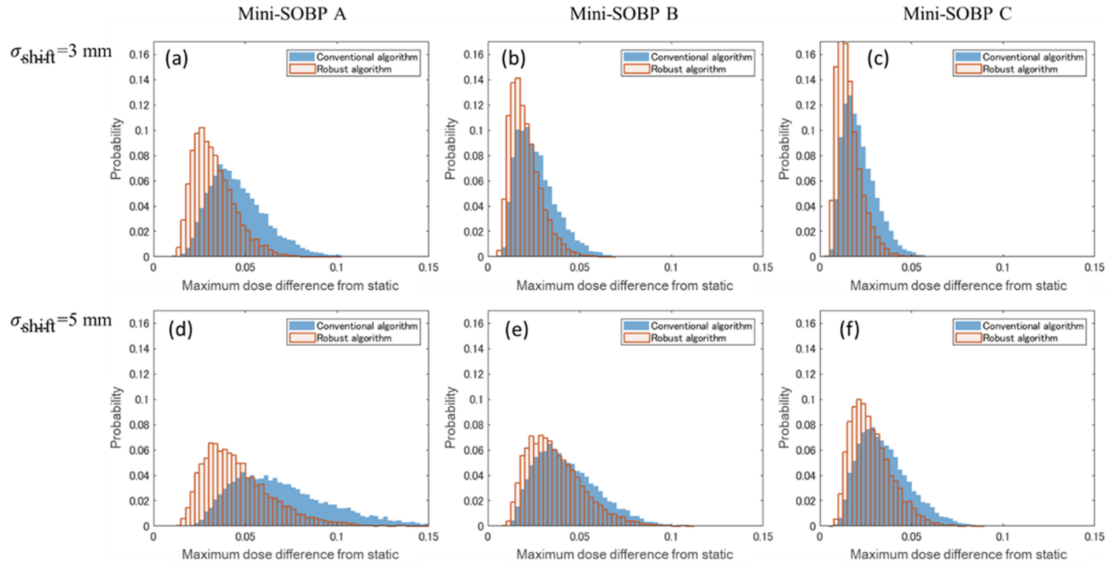
Fig. 3.8 The histogram of the maximum dose difference between with and without WED variation with σ_{shift} =3 mm and 5 mm for the mini-SOBP of type A, B and C.

Table 3.3 Pass rate for maximum difference between the violated and static dose within 0.05 under WED with σ_{shift} = 3 mm and 5 mm.

σ_{shift} [mm]	Algorithm	Pass rate [%]		
		Type A	Type B	Type C
3	Conventional	64.9	96.4	99.2
	Robustness	91.8	99.6	100
5	Conventional	25.9	68.3	85.1
	Robustness	65.6	81.7	95.5

3.3.4   Evaluation in three-dimensional bases

Fig. 3.9 (a) and (b) shows the static dose distribution over the xz plane with the conventional algorithm and the robustness algorithm, respectively, by the three-dimensional MC simulation. One sample of the dose distribution generated with a set of random positional errors for each slice was also shown in Figs. 3.9 (c) and (d) for the conventional and robustness algorithm, respectively. Fig. 3.9 (e) and (f) shows a two dimensional map of the dose difference between the static distribution and that with positional errors for each algorithm. The variation of

the dose distribution around the lateral penumbra region and the distal falloff region was found to be significantly larger in comparison with that around the center of the target. This is because of the shape of the bolus used, as shown in Fig. 3.10 (a). Fig. 3.10 (b) shows the corresponding change of the proton range when protons pass the bolus with the positional shift of 3 mm, 6 mm, and 9 mm from the original position. Protons passing through the center of the target region around $x = \pm 10$ mm have no range variation against the positional error due to the constant thickness of the bolus while the proton range can change by between 4 mm and 9 mm around $x = \pm 30$ mm with a positional error of between 3 mm and 9 mm. Despite this large range variation around the off-center region, the area of the larger dose deviation, as shown in Figs. 3.9 (e) and (f), can be strongly reduced by the robust algorithm in comparison to that in the conventional algorithm. Fig. 3.11 (a) and (b) shows the volume histogram of the dose difference between static distributions and randomly shifted distributions in the target volume and OAR volume, respectively for each algorithm. In the target, the shape of the histogram in the robustness algorithm shows a slightly narrower shape than that in the conventional algorithm. On the other hand, as shown in Fig. 3.11 (b), the strong deviations of dose difference in the conventional algorithm were reduced by a factor of two in the robustness algorithm and the width of the histogram in the robustness algorithm becomes much narrower than that in the conventional algorithm. Fig. 3.12 (a) and (b) shows the maximum, minimum and average of DVHs among 1000 random trials for the target and the OAR, respectively, for each algorithm. As shown in Fig. 3.12 (a), the target DVH is almost unchanged in two algorithms. The DVH parameters of the target volume in the static distribution and randomly shifted distribution are summarized in Table 3.4. In the randomly shifted distribution, the standard deviation of maximum and minimum dose was reduced to roughly $\frac{2}{3}$ with the robustness algorithm compared with those with the conventional algorithm, which is consistent with the result of one-dimensional simulation. Fig. 3.12 (b) shows the DVH of the OAR volumes and the DVH parameters are also summarized in Table 3.5. The dose volume above 50% of the prescribed dose was reduced in the robustness algorithms in comparison to that in the conventional algorithm. In particular, the value of V80% in the robustness was 30% smaller than that in the conventional algorithm and the robustness algorithm could maintain the higher dose volume.
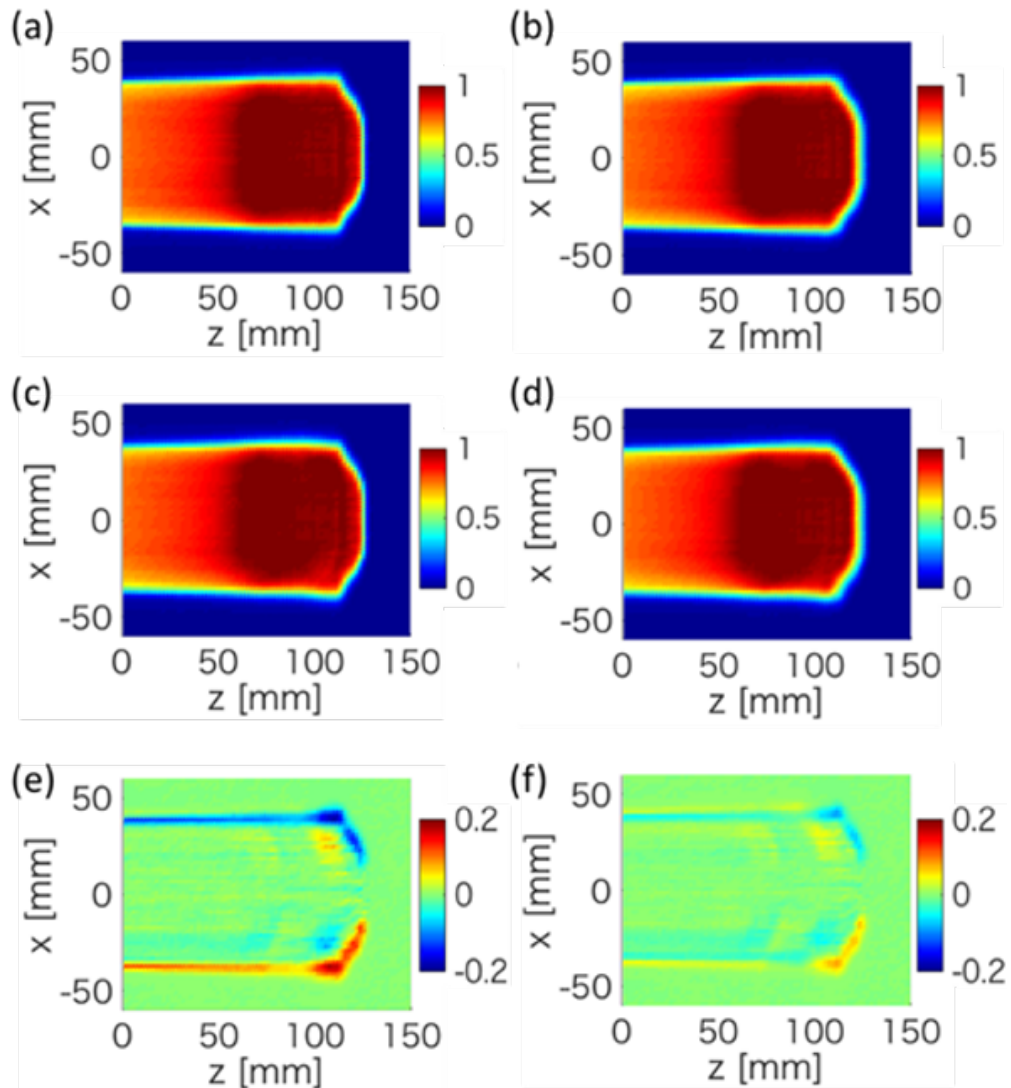
Fig. 3.9 The upper panel shows calculated static dose distributions for the conventional algorithm (a) and the robustness algorithm (b). The middle panel shows one sample of the dose distribution with random positional errors for the conventional algorithm (c) and the robustness algorithm (d). The lower panel shows the dose difference between the static distribution and that with positional errors for the conventional algorithm (e) and the robustness algorithm (f).

3.4   Discussion

In this work, we have developed a weight optimization algorithm for layer-stacking irradiation to produce a robust depth dose distribution against the variation of water equivalent depth (WED). Intra-fractional movements of the patient's body or respirational movements during each layer's irradiation cause variations of water equivalent depth along the proton beam
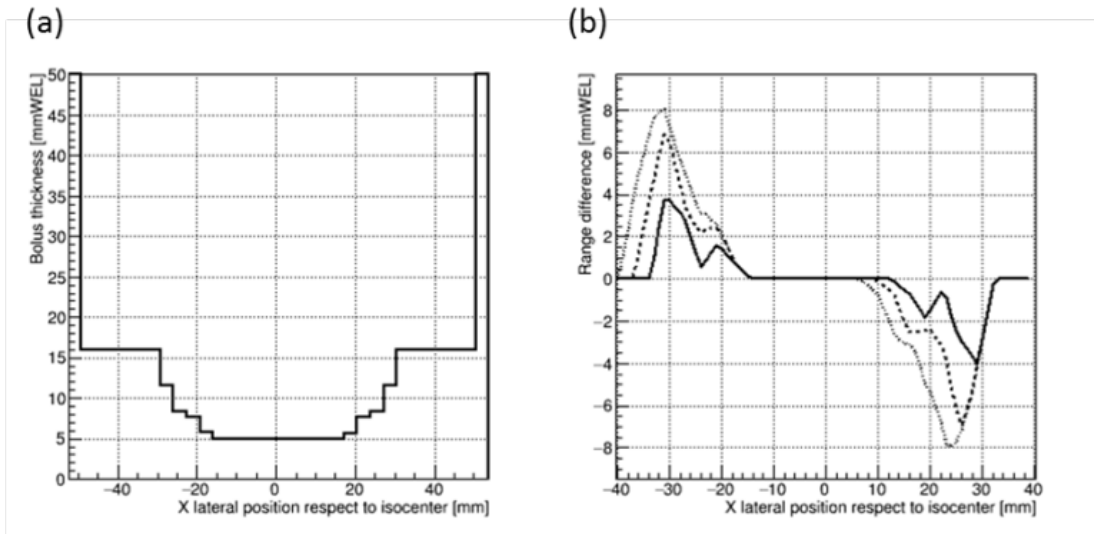
Fig. 3.10 The shape of the used bolus with the smearing value of 3 mm along the lateral beam position and the proton range difference when protons pass the bolus with the positional shift of 3 mm (solid), 6 mm (dashed), and 9 mm (dotted) from the original position.
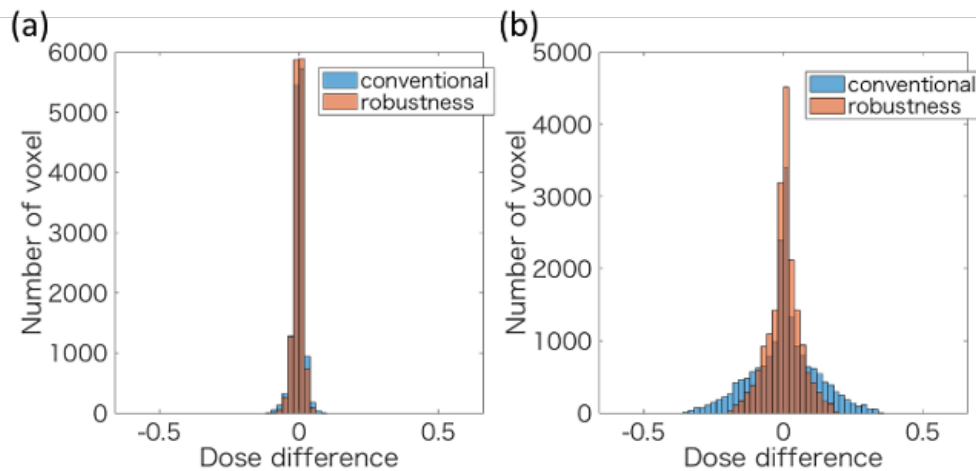
Fig. 3.11 The volume histograms of the dose difference between static distributions and randomly shifted distributions for the target (a) and the OAR (b).

direction. We assumed the value of 3 mm used as the standard deviation in this work to simulate the WED variation due to the intra-fractional movement in the case of head and neck treatment, where spatial displacements of bony structures were measured for thirty patients treated at FPHPTC by using kV-X ray images before and after treatment, and the standard deviation of the displacement along the vertical, lengthwise, and lateral directions was 0.8 mm, 0.4 mm, and 0.8 mm, respectively. Then, WED value over the target surface
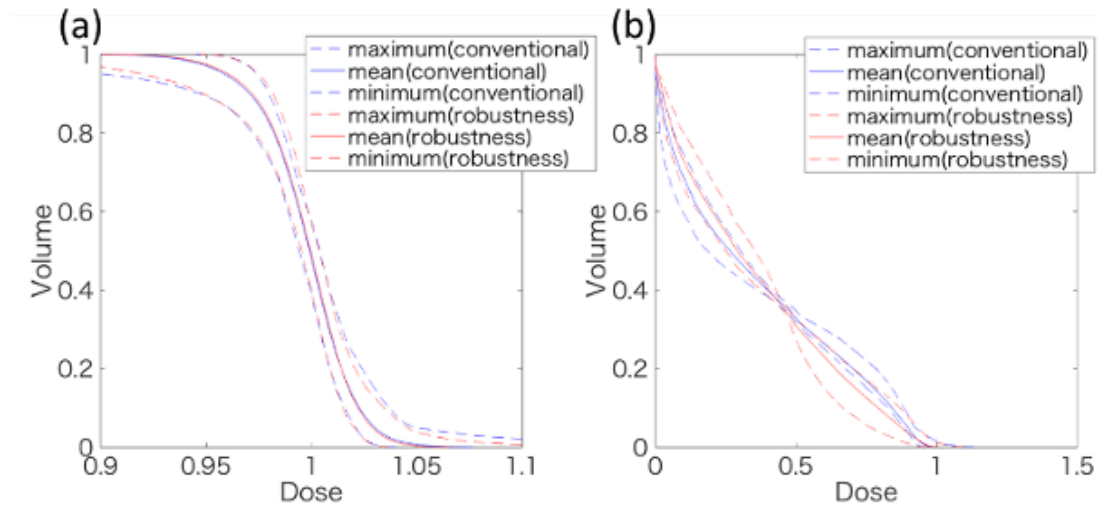
Fig. 3.12 The average and maximum/minimum envelope of DVH among 1000 trials of position shift simulation for the target (a) and the OAR (b).

along the beam direction was calculated by integrating the converted water density from CT volumetric data used for treatment planning. Also, the variation of WED value along the beam directions due to movement of the patient's body was simulated by shifting the position of the beam iso-center on CT data. In the layer-stacking method for proton therapy, mini-SOBP distributions with a width of around 10 mm are stacked step-by-step along the beam direction by changing the thickness of the range-shifter with a step of 5 mm, and the uniform dose distribution can be produced conforming to the shape of the PTV. Since the practical length of the distal falloff of the mini-SOBP distribution used in the treatment was less than 1 cm, several millimeters of the WED variation can easily cause about ten percent of hot/cold spots to the objective dose at the joints of mini-SOBPs. In particular, the WED variation occurring between the 1st and 2nd layer's irradiation strongly disturbs the uniformity and reproducibility of the depth dose distribution around the distal region, since the delivered dose in these layers dominates that in others. Thus, one needs to pay special attention to the variation of the dose coverage around the distal side of the PTV, and tolerance dose of normal tissues placed after the PTV, for example, the brain stem, optic chiasma, and spinal cord in the case of head and neck treatment. Based on the above discussions, we subdivided the layers into a group of the 1st and 2nd layers and a group of the other layers, and the weight optimizations were carried out by setting the maximum limitation of weight values depending on the group. The maximum limitation makes weights more balanced among layers in comparison with the conventional method, and disperses the sensitivity

Table 3.4 The DVH parameters of the target volume in the static and random distributions. The values and those inside parentheses for the random distributions show the averaged values and standard deviations, respectively.

	Conventional		Robustness	
	Static	Random	Static	Random
Mean	1.000	0.998 (0.001)	1.000	0.998 (0.001)
Maximum	1.039	1.077 (0.027)	1.035	1.066 (0.017)
Minimum	0.943	0.893 (0.043)	0.944	0.900 (0.031)
D95%	0.976	0.956 (0.009)	0.976	0.961 (0.008)
D80%	0.988	0.982 (0.002)	0.989	0.983 (0.002)

Table 3.5 The DVH parameters of the OAR volume in the static and random distributions. The values and those inside parentheses for the random distributions show the averaged values and standard deviations, respectively.

	Conventional		Robustness	
	Static	Random	Static	Random
Mean	0.350	0.353 (0.003)	0.349	0.352 (0.003)
Maximum	0.986	1.004 (0.022)	0.991	1.009 (0.021)
V20%	0.557	0.557 (0.012)	0.584	0.601 (0.020)
V50%	0.326	0.328 (0.004)	0.311	0.308 (0.006)
V80%	0.128	0.134 (0.010)	0.107	0.096 (0.016)

of WED variation occurring in certain layers' irradiation to the summed dose distribution. Then, the robust algorithm searched for the minimum point of the objective function over all sets of the maximum limitations for the weight optimization. This objective function was analytically derived based on the depth dose distribution of the mini-SOBP and Gaussian distribution with the constant WED variation as an input.

3.4.1 Depth dose distribution produced by Robustness Algorithm

As shown in Figs. 3.7 and 3.8, the robustness algorithm can reduce the changes of the depth dose distribution caused by the WED variation with σ_{shift}= 3 mm, compared with those of the conventional algorithm. On the other hand, the distribution by the robustness algorithm had smaller SOBP length and larger distal falloff than that by the conventional algorithm, while both distributions around the proximal region coincided well. Moreover, as shown in Table 3.2 for type B, the depth, z_d^{95}, corresponding to 95% of the objective dose at the distal side in the robustness algorithm was 1.8 mm shallower than that in the conventional algorithm, since the robustness algorithm balanced the weight value of the 1st and 2nd layer while the weight value was concentrated in the 1st later in the conventional algorithm, demonstrated in Fig. 3.6 (a). In practical treatment, the difference of 1.8 mm in the depth of z_d^{95} should be compensated by tuning the thickness of the energy degrader in order to maintain the dose coverage for the distal edge of the target.

3.4.2 Approach to the robust dose distribution in the layer-stacking method

The shape of the partial depth dose distribution of each layer (mini-SOBP) is also an important factor to determine the robustness. In the case of carbon ion therapy, the layer-stacking method was also used in their treatment and Gaussian shaped mini-SOBP was proposed to enhance the robustness against the WED variation among layers [46]. Here, the original shape of the Bragg peak was blurred to a Gaussian shape and the overlap between each of the dose distributions among layers was also increased to reduce the magnitude of hot/cold spots. In this work, we also examined the robustness algorithm based on each of three types of mini-SOBPs where the sharpness of the depth dose distributions are varied as shown in Fig. 3.1 and Table 3.1. As shown in Fig. 3.8 and Table 3.3, the variations of the dose distribution are suppressed for all types of mini-SOBPs in the robustness algorithm compared with those in the conventional algorithm. In particular, the reduction of dose variation by introducing the robustness algorithm was the most significant in the mini-SOBP of type A, which has the sharpest distal falloff. On the other hand, in the case of the mini-SOBP of type C, which has the most relaxed shape of depth dose distribution, the robustness is better but the improvement of the robustness by the robustness algorithm was smaller than for type A or B. This is because the mini-SOBP of type C has the largest value of distal falloff and it

is large compared with the range of WED variation: 3-5 mm. Therefore, we consider that the developed algorithm is much more suitable for enhancing the robustness against WED variation while maintaining the sharp distal edge to reduce the unnecessary dose to normal tissues. On the other hand, simply using a very blurred shape of mini-SOBP is more effective than the developed algorithm when the range of target motion is much larger (e.g., a lung tumor).

3.4.3 Evaluation in three-dimensional bases

Based on each weight optimization algorithm, three-dimensional dose distributions in the water equivalent phantom were evaluated by the Monte-Carlo proton dose calculation system developed at FPHPC. As shown in Fig. 3.9, larger dose variation due to the positional error along the lateral direction was found around the lateral penumbra and distal falloff region, and was caused by the gradient of the thickness of the used bolus. Since the OAR volumes are often placed behind the target volume along the beam direction or beside the volume along the lateral direction, in particular, for head and neck treatment, the robust dose distribution against the positional error is strongly desired to carry out the treatment safely. As shown by Fig. 3.12 and Tables 3.4 and 3.5, while averaged DVH parameters for the target are almost equivalent in the two algorithms, the minimum/maximum dose deviation in the target volume and the high-dose volume of the OAR in the robustness algorithm were found to be smaller than that in the conventional algorithm Therefore, applying the robustness algorithm to the weight optimization in layer-stacking radiation may provide safer treatment.

3.4.4 Comparison between the layer-stacking method and the scanning method

Generally speaking, the scanning method is weak against patient motion compared with the layer-stacking method, because not only inter-layer correlation in the depth direction but also three-dimensional intra-layer motion disturbs the dose distribution in the beam scanning method. This so-called "interplay effect," can be reduced by the repainting technique [81] and a sufficient number of repaintings make the robustness of dose distribution by the beam scanning method almost equivalent to that of the layer-stacking method, though the large number of repainting results in long treatment time. Inaniwa et al. [79] developed an another algorithm which made relaxed dose distribution in the boundary of overlapping fields to

enhance the robustness of the dose distribution of multi-field against setup errors in intensity modulated particle therapy. This may have a similar effect to relaxing the mini-SOBP in layer stacking method, rather than limiting the weight. However, relaxing mini-SOBP in later-stacking method leads to larger distal fall-off as already discussed, while beam scanning method can simultaneously realize relaxed dose in overlapped region and sharp edge at the target boundary because of its higher degree of freedom in in determining the weight values of a lot spots. Inaniwa et al. [82] also developed the robustness weight optimization algorithm for the beam scanning method where penalty conditions considering risk factors of dose to OARs due to set-up errors and beam range errors were accounted for . Our proposal is similar to their method at the point that the weight values in a certain region area are reduced, while they set the penalty term to weight values in the cost function instead of setting upper limit of the weight. They evaluated the effectiveness of reducing unwanted dose to OARs. however, while they did not discuss the relationship between controlling limiting the weight set and keeping dose uniformity homogeneity in the target volume.Since their optimization algorithms made use of the large degree of freedom in determining the weights of spots in the beam scanning method, a similar scheme cannot be applied to the layer-stacking method with a smaller degree of freedom in weights of layers. On the other hand, The way of limiting the maximum value of the weight which we developed for the layer-stacking method can be applied to the beam scanning method and is expected to have an effect of obtaining three-dimensional robust dose-distributions against WED variations and motions in the lateral direction by redistributing large spot weights to neighboring spots.

3.4.5   The limitations of the developed method

The robust solution obtained by the developed method is often found on the boundary of the appropriate region of the condition space, as shown in Fig. 3.5. In particular, the value of X_a, which is the maximum limitation of the weight values for the layers at the distal side, usually has a strong correlation with distal falloff and R value defined by Eq. (3.8); thus, a stronger constraint for distal falloff results in a solution with less robustness. Therefore, the selection condition of the distal falloff for appropriate sets of X_a and X_b values may need to be carefully considered, and sometimes have to be tuned, in 3D proton treatment planning using the patient's CT-images with simulating dose changes due to WED variations, although we demonstrated the effectiveness of the robust algorithm based on the 3D uniformed water phantom using MC proton dose calculation. However, the work for 3D dose evaluation in the

proton treatment planning system is beyond the scope of this research within our materials, and we will study this in the future.

3.5   Conclusion

We developed a new optimization algorithm for the weight values of mini-SOBPs in layer-stacking proton therapy, which can enhance the robustness against WED variation of the layer depth. In the developed algorithm, we introduced the maximum limitations of the weight values. We searched for the best set of limitation condition based on the evaluation function of robustness, which is defined by assuming random Gaussian probability density function of depth shifts of layers. The depth dose distribution optimized by the developed algorithm was stable under the random position shifts of the layers in the depth direction, compared to the conventional weight optimization algorithm, while SOBP length and distal falloff become worse. The developed algorithm was more effective when the shape of the mini-SOBP was sharp, and was also demonstrated by 3D dose calculation in the water phantom with an aspherical target. Thus, this algorithm in layer-stacking proton therapy may be useful for treatment where the sharpness of the distal falloff along the depth distribution needs to be maintained to spare the organ at risk.

Supplementary Materials

In this section, the derivation of Eqs. (10) and (11) is shown and the expectation value of variable x is defined by $\langle x \rangle$. We introduced z'_i as a deviation of depth value on i-th layer and, in this case, the summed depth dose distribution is expressed as,

$$D_{SOBP}(z) = \sum_{i=1}^{n} \chi_i d_i(z - z'_i) \tag{3.13}$$

The probability density of depth deviations for all layers is defined here by the function of $P(z'_1, z'_2, \cdots, z'_n)$ and the expectation of $D_{SOBP}(z)$ can be expressed by,

$$D_{SOBP}^{\text{mean}}(z) = \langle D_{SOBP}(z) \rangle = \iiint \cdots \int \left(\sum_{i=1}^{n} \chi_i d_i(z - z'_i) \right) P(z'_1, z'_2, \cdots, z'_n) dz'_1 dz'_2 \cdots dz'_n, \tag{3.14}$$

where the operator of $\int dz_i'$ means the integration on the depth deviation of i-th layer with the range of $(-\infty, \infty)$. Considering that depth deviations among all layers are independent and the provability density follows Gaussian distribution, Eq. (3.14) can be rewritten using by

$$\langle D_{\text{SOBP}}(z) \rangle = \sum_{i=1}^{n} \left\{ \iiint \cdots \int \chi_i d_i (z - z_i\prime) \prod_{j=1}^{n} G\left(z_j'\right) d z_j' \right\}, \tag{3.15}$$

where we used the relation of $P\left(z_1', z_2', \ldots, z_n'\right) = \prod_{i=1}^{n} G\left(z_i'\right)$. In addition, all of Gauss distributions follow the normalization condition of $\int_{-\infty}^{\infty} G\left(z'\right) d z' = 1$ and the integration of Eq. (3.15) can be further reduced to the one with $i = j$ as the form of Eq. (10) like,

$$\langle D_{\text{SOBP}}(z) \rangle = \sum_{i=1}^{n} \left\{ \int_{-\infty}^{+\infty} \chi_i d_i (z - z_i\prime) G\left(z_i'\right) dz_i\prime \right\}. \tag{3.16}$$

Next we shows the derivation of Eq. (11). The dispersion of the summed dose distribution can be calculated based on statistics by

$$D_{\text{SOBP}}^{variance}(z) = \langle D_{\text{SOBP}}(z)^2 \rangle - \langle D_{\text{SOBP}}(z) \rangle^2. \tag{3.17}$$

The analytical calculation of the first term in the right side of Eq. (3.17) is followed by

$$\langle D_{\text{SOBP}}(z)^2 \rangle = \iiint \cdots \int \left(\sum_{i=1}^{n} \chi_i d_i (z - z_i\prime) \right)^2 \prod_{k=1}^{n} G\left(z_k'\right) d z_k'$$

$$= \iiint \cdots \int \left(\sum_{i=1}^{n} \chi_i d_i (z - z_i\prime) \right) \left(\sum_{j=1}^{n} \chi_j d_j (z - z_j\prime) \right) \prod_{k=1}^{n} G\left(z_k'\right) d z_k'. \tag{3.18}$$

The integrations in Eq. (3.18) are further reduced to those with $i = k$ or $j = k$ and, thus, written by

$$\langle D_{\text{SOBP}}(z)^2 \rangle = \sum_{i=1}^{n} \left\{ \int_{-\infty}^{+\infty} (\chi_i d_i (z - z_i\prime))^2 G\left(z_i'\right) dz_i\prime \right\}$$

$$+ \sum_{i \neq j}^{n} \left\{ \iint_{-\infty}^{+\infty} \chi_i \chi_j d_i (z - z_i\prime) d_j (z - z_j\prime) G\left(z_i'\right) G\left(z_j'\right) dz_i' d z_j' \right\}, \tag{3.19}$$

where $\sum_{(i \neq j)}$ means the summation of n(n-1) samples on $i, j = 1, 2, \cdots, n$ without the combination of $i = j$. In addition, the second term in the right side of Eq. (3.19) can be factorized by the individual integration over z_i' and z_j' as

$$
\sum_{i \neq j}^{n} \left\{ \int_{-\infty}^{+\infty} \chi_i d_i \left(z - z_i\prime\right) G\left(z_i'\right) dz_i' \right\} \left\{ \int_{-\infty}^{+\infty} \chi_j d_j \left(z - z_i\prime\right) G\left(z_j'\right) dz_j' \right\}
$$
$$
= \left\{ \sum_{i=1}^{n} \int_{-\infty}^{+\infty} \chi_i d_i \left(z - z_i\prime\right) G\left(z_i'\right) dz_i' \right\}^2 - \sum_{i=1}^{n} \left\{ \int_{-\infty}^{+\infty} \chi_i d_i \left(z - z_i\prime\right) G\left(z_i'\right) dz_i' \right\}^2 . \quad (3.20)
$$

By using relations of Eqs. (3.17), (3.19) and (3.20), the dispersion can be derived as

$$
D_{\text{SOBP}}^{variance} (z)
$$
$$
= \sum_{i=1}^{n} \left\{ \int_{-\infty}^{+\infty} \left(\chi_i d_i \left(z - z_i\prime\right)\right)^2 G\left(z_i'\right) dz_i\prime \right\} - \sum_{i=1}^{n} \left\{ \int_{-\infty}^{+\infty} \chi_i d_i \left(z - z_i\prime\right) G\left(z_i'\right) dz_i' \right\}^2 . \quad (3.21)
$$

The standard deviation of $\sigma_{\text{dose}}^{\text{1fr}}(z)$ is obtained by the squared root of $D_{\text{SOBP}}^{variance}(z)$ in Eq. (3.21).

Chapter 4

Spot Arrangement Optimization for Pencil Beam Scanning in Particle Therapy

Pencil beam scanning technique can provide good dose distribution which is conformal to a complex shaped tumor in particle beam therapy. In this chapter, we present an optimization method to derive the non-lattice spot arrangement pattern with a smaller number of beam spots, compared with the conventional lattice pattern, for the purpose of shortening the treatment time. In the developed algorithm, a large enough number of spots were located densely in every layer at the initial state, and then the spot with the smallest contribution was removed one by one through iterations. For the selection of the spot to be removed, a weight optimization process with an objective function was employed. The developed algorithm was tested by numerical examples of spherical targets with a radius of 30 mm surrounded by the organs at risk. The dose quality with the obtained spot arrangement and that with the lattice spot arrangement were compared, with both conditions of a nominal number of spots and reduced number of spots. With the proposed algorithm, the number of spots was significantly reduced while the dose quality was kept within a tolerance level, compared to the cases with the lattice spot arrangements. Further, in the obtained spot arrangement, the spots were located on the closed lines which were concentric to the target contour.

4.1 Introduction

Particle beam therapy [7, 8] has attracted increasing interest as a less-invasive cancer treatment compared with other therapies such as surgery, chemotherapy or X-ray radiotherapy. When the charged particles such as protons or carbon ions with high energy are irradiated into the patient, the kinetic energy of the particles is transferred to the body through the ionization effect and the cells in the cancer tumor are destroyed. The radiation dose, which is the energy absorption from the particle beam, becomes maximum at the certain depth from the patient skin where the particles stop in the patient's body. This feature of the dose distribution in the depth direction is called the Bragg peak, and the peak depth can be controlled by changing the initial beam energy. To generate a high energy particle beam, a particle accelerator such as a cyclotron or synchrotron is used. After acceleration, the particle beam is administered to the patient in the treatment room.

For the clinical purpose, the dose should be as ideally homogeneous within the tumor and simultaneously as low outside the tumor as possible. The pencil beam scanning (PBS) technique is currently a very popular irradiation method to form a three dimensional dose distribution which precisely matches the target shape [83, 77] With PBS, many beam irradiation points, which are called spots, are located in the patient's body and a particle beam is administered to each spot. After the dose is given to one spot, the beam is moved to the next spot. The beam sequentially irradiates all the spots which are arranged inside and around the target volume, as if painting it out by a pencil. The beam motion is controlled by the magnetic field generated by a pair of electromagnets called scanning magnets [37] which are installed in the beam irradiation nozzle. In order to determine the operation pattern of the scanning magnets, both the positions of all the spots and the number of particles given to each spot must be determined by using the optimization technique.

In many prior studies in PBS, the positions of the beam irradiating spots are set to be basically lattice patterns and are unchanged through optimization, although the number of particles to each spot is optimized to form an ideal dose distribution [34]. In addition, shortening the treatment time is also an important criteria for the physical burden of the patient, and decreasing the number of spots directly contributes to the treatment time reduction. By using heuristic approaches such as simulated annealing, several researchers addressed proposing the scan path optimization technique to find the best order of spots to be irradiated for minimizing the total path length of the beam motion [49–51]. In these studies, however,

the spot positions were still fixed with the lattice pattern and the number of spots was also fixed.

Contour scanning technique [84, 85] was proposed as a non-lattice spot layout, in which spots are located on the enlarged contour of the target cross section and its concentric curve with a constant spacing. It was found that the contour based spot layout leads to a better dose distribution than the conventional lattice spot laypiy especially with the point that the unnecessary dose outside the target could be reduced. In their method, however, the spot positions were determined on a rule-base and the mathematical optimality of the spot layout was not discussed.

On the other hand, in the research field of mechanical engineering, many position optimization techniques were studied for various purposes.

Fukushima et al. [86] proposed an optimization method of engine mounting layout in a vehicle, using the Most Probable Optimum Design (MPOD) method. Similarly, Nishiura et al. [87, 88] proposed an optimization of the stator pole arrangement of a spherical actuator by a genetic algorithm. In these methods, the locations of multiple objects were optimized while the number of the objects never changed through optimization. Matsumoto et al. [89] proposed a method to determine the optimal placement of solar arrays that maximize the total amount of received light. With this method, the layout of the solar arrays was kept to a lattice pattern while the number of solar arrays was optimized by changing the interval of the solar arrays and the relative position of the lattice coordinate to the site boundary.

For optical apparatus, as another example, several techniques for layout optimization have been studied in order to design actuator locations for deformable mirrors. For example, Haftka *et al* [52] have reported optimal actuator locations for space antennas based on the surface control method. On the other hand, Yamaki et al. [53] proposed an actuator layout design method for deformable mirrors in fundus imaging modality. Their method can obtain the optimal layout of a minimum number of actuators while keeping the error of mirror surface deformation small enough. In their approach, many actuators were located at the initial step and then an actuator was removed step by step based on the contribution of each actuator. For proton beam scanning, Van de Water *et al* [90] employed a similar method of layer reduction and spot reduction in the treatment planning while they didn't discuss the relationship between the optimum spot locations and the target geometry.

In this research, we construct a heuristic method in determining optimum spot locations in PBS, which can realize acceptable dose distribution with a smaller number of spots than

the conventional lattice pattern. First, we formulate the dose optimization problem with fixed spot locations. Then we present the algorithm to obtain optimum spot locations by iteratively removing the spot with low contribution to form the dose distribution. Unlike the method of Yamaki et al. which optimizes the two-dimensional locations of several tens of actuators, the spots in PBS are located in three-dimensions, and usually more than thousands of spots should be removed. Therefore, we also propose the improved method to accelerate the optimization process by introducing a multiple spot reduction scheme and confirm its effectiveness.

4.2 Methods

4.2.1 Pencil beam scanning overview

Figure 4.1 shows a schematic of PBS. The target volume is divided into plural layers which are perpendicular to the beam direction and spots are located in each layer. Each spot in the layer is sequentially irradiated, as it is painted by a moving pencil beam. After every spot in one layer is irradiated, the beam energy is shifted to change the layer. Here, we define the coordinate in which the beam direction is along the z axis and the layers are parallel to the xy plane. The spots are located mainly inside the target T. A small number of spots are also located outside and close to the target boundary, in order to enhance the dose sharpness at the target edge.

Figure 4.2 (a) shows a schematic of the irradiation nozzle for PBS. A pair of scanning magnets are installed in the nozzle and each of them generates a magnetic field to the y and x directions. Since the particle beam is a positive charge, the beam direction is slightly bent to the x and y directions by the Lorentz force. The xy position of the beam at the patient can be controlled by adjusting the current to the scanning magnet which correlates to the strength of the magnetic field and the beam bending angle. The nozzle also contains the beam position monitor and the dose monitor which enable the feedback control of the beam position and the beam dose, respectively. Figure 4.2 (b) shows an example of the operation pattern of the scanning magnets and Fig. 4.2 (c) shows the path of the beam position in the xy plane. The beam position stays at a spot when the magnetic fields of both magnets are fixed, and the beam position moves to the x or y direction when the corresponding magnetic field changes. The time length of staying at a spot corresponds to the number of particles to be irradiated to the spot.
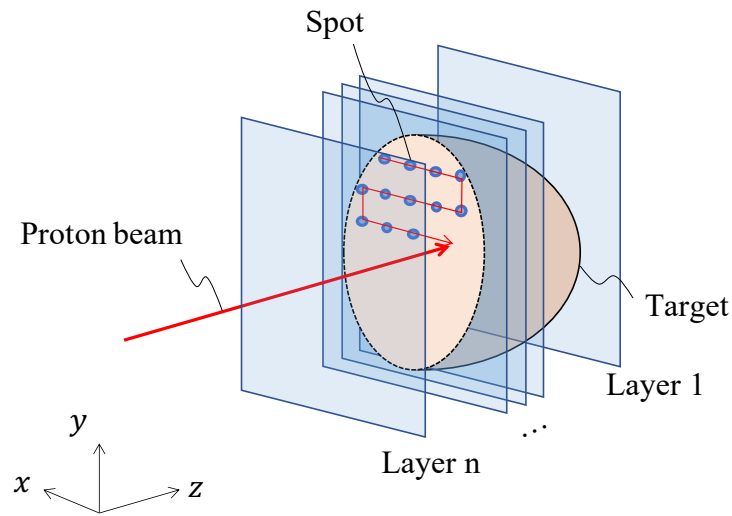
Fig. 4.1 Image of the beam spots in PBS.
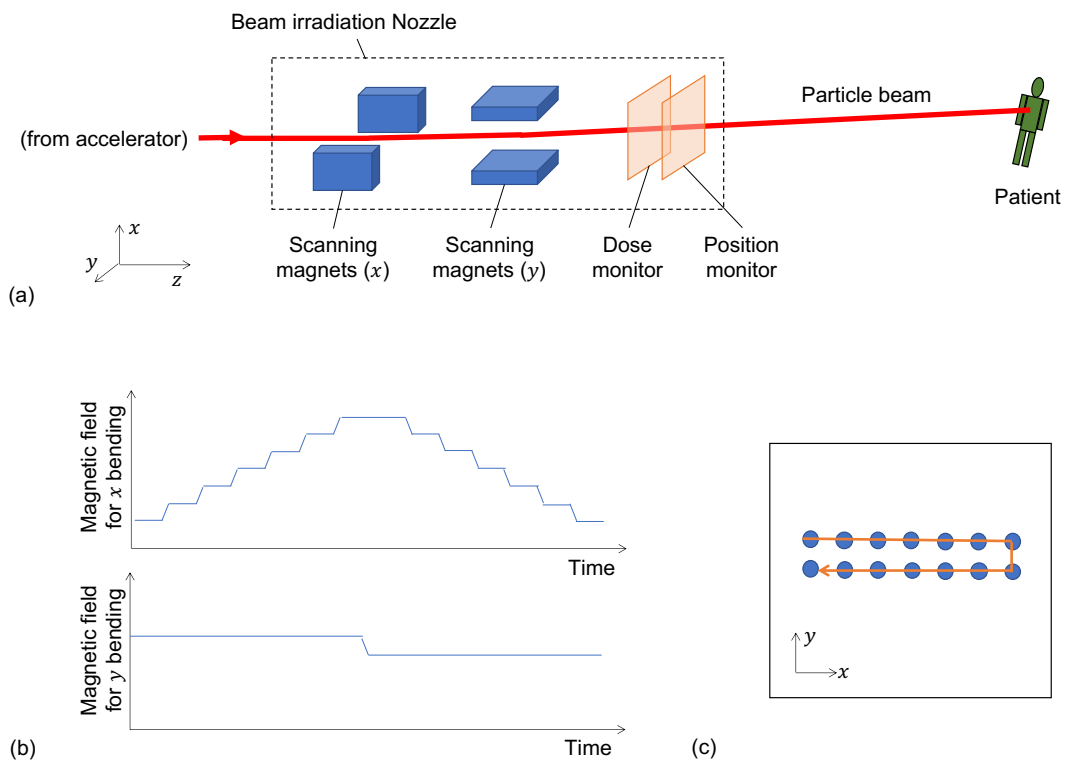
Fig. 4.2 (a) Schematic of the beam irradiation nozzle and the scanning magnets in PBS. (b) Example of the scanning magnet operation. (c) Example of the beam position motion corresponding to the scanning magnet operation in (b).

4.2.2 Formulation of dose distribution calculation

We assumed the two-dimensional Gaussian as the dose distribution of a single spot in the xy plane, as follows.

$$D_{xy:i}(x,y) = \frac{1}{2\pi\sigma^2} \exp\left(-\frac{(x-x_i)^2 + (y-y_i)^2}{2\sigma^2}\right), \tag{4.1}$$

where (x_i, y_i) denotes the position of the i-th spot, and σ is the beam spot size. Here, we consider the spot shape is approximately isotropic, while the actual beam spot shape is an ellipsoid represented by using σ_x and σ_y.

Depth dose distribution along the z direction was obtained by Monte-Carlo simulation [91, 80].

Figure 4.3 shows the simulated depth dose distribution $D_{z:i}(z)$ of proton beam with the energy of 130 MeV. Three-dimensional dose distribution of a single spot is calculated by the multiplication of two-dimensional dose and depth dose distribution as

$$D_i(x,y,z) = D_{xy:i}(x,y) \times D_{z:i}(z). \tag{4.2}$$
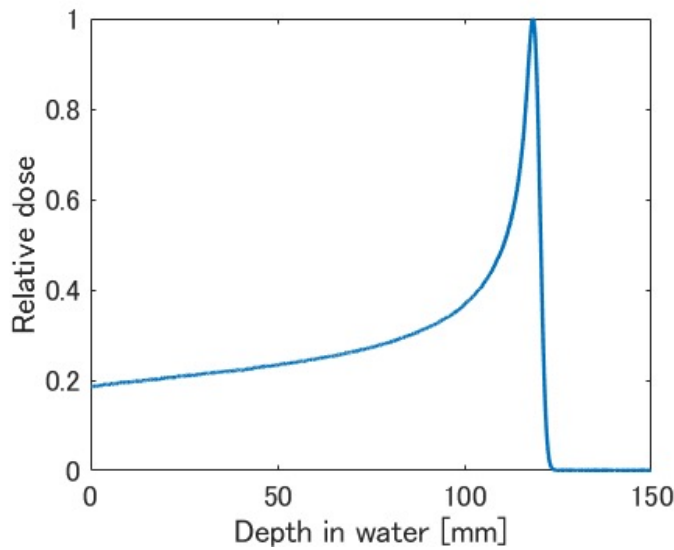
Fig. 4.3 Simulated depth dose distribution of the particle beam.

The total dose distribution D_{total} is calculated as the weighted sum of contribution from each spot as

$$D_{total}(x,y,z) = \sum_{i=1}^{N} \chi_i D_i(x,y,z),$$

(4.3)

where χ_i stands for the number of particles delivered to the i-th spot and N stands for the number of spots.

4.2.3 Requirements for the dose distribution

In particle beam therapy, the dose distribution is required to be homogeneous inside the target while it should be as small as possible outside the target. In this study, we set the objective function f as follows.

$$f = w_1 f_1 + w_2 f_2 + w_3 f_3.$$

(4.4)

$$f_1 = \frac{\int_T \left(D_{total}(x,y,z) - D_{obj}\right)^2 d\Omega}{\int_T d\Omega}.$$

(4.5)

$$f_2 = \frac{\int_{\bar{T}} (D_{total}(x,y,z))^2 d\Omega}{\int_{\bar{T}} d\Omega}.$$

(4.6)

$$f_3 = \frac{\int_O (D_{total}(x,y,z))^2 d\Omega}{\int_O d\Omega}.$$

(4.7)

Here, f_1, and f_2 stand for the square of the dose difference from the objective dose D_{obj} in the target region, T, and the square dose in the region outside the target, $\bar{T}$, respectively. Besides, particularly important organs where it is strongly desired to avoid the dose irradiation, such as the heart or the esophagus, are called as organs at risk (OARs) and f_3 stands for the square of the dose in the OAR region, O. Figure 4.4 shows a general, simple schematic of the regions T, $\bar{T}$, and O. The symbols w_1, w_2, and w_3 are the weighting factors for f_1, f_2, and f_3, respectively. Each of f_1, f_2, and f_3 was normalized by the total volume of the region. In this objective function, the first term f_1 makes the dose distribution close to the ideal one inside

the target. The second term f_2 and the third term f_3 reduce the total amount of unnecessary dose outside the target and in the OAR, respectively. The region O is usually included in $\bar{T}$ and w_3 is set to be a larger value than w_2 to reduce the OAR dose more strongly than the dose at general volume outside the target.
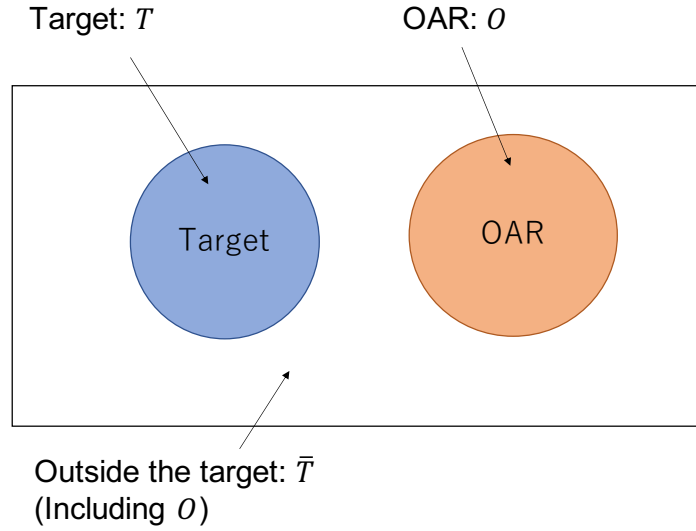
Fig. 4.4 Relationship among the target, outside the target, and the OAR

4.2.4   Particle number optimization with a fixed spot layout

The objective functions in Eqs. (4.4-4.7) can be transformed as follows. The integration in the target T was calculated as

$$
\begin{aligned}
\int_T \left(D_{total} - D_{obj} \right)^2 d\Omega &= \int_T \left(\sum_{i=1}^N \chi_i D_i - D_{obj} \right)^2 d\Omega \\
&= \int_T \left(\sum_{i=1}^N \sum_{j=1}^N \chi_i \chi_j D_i D_j - 2 D_{obj} \sum_{i=1}^N \chi_i D_i + D_{obj}{}^2 \right) d\Omega \\
&= \sum_{i=1}^N \sum_{j=1}^N \chi_i \chi_j \int_T D_i D_j d\Omega - 2 D_{obj} \sum_{i=1}^N \chi_i \int_T D_i d\Omega \\
&\quad + D_{obj}{}^2 \int_T d\Omega.
\end{aligned}
\tag{4.8}
$$

The integration outside the target $\bar{T}$ was calculated as

$$
\begin{aligned}
\int_{\bar{T}} (D_{total})^2 \, d\Omega &= \int_{\bar{T}} \left(\sum_{i=1}^{N} \chi_i D_i \right)^2 d\Omega \\
&= \int_{\bar{T}} \sum_{i=1}^{N} \sum_{j=1}^{N} \chi_i \chi_j D_i D_j \, d\Omega \\
&= \sum_{i=1}^{N} \sum_{j=1}^{N} \chi_i \chi_j \int_{\bar{T}} D_i D_j \, d\Omega.
\end{aligned}
\tag{4.9}
$$

The integration in the OAR O was also calculated the same as Eq. (4.9). Therefore, the objective function f was represented as

$$
f = X^T H X + D_{obj} \Lambda^T X + D_{obj}{}^2,
\tag{4.10}
$$

where the matrix H and the vectors X and Λ are defined as follows.

$$
H =
\begin{pmatrix}
h_{11} & h_{12} & \dots & h_{1N} \\
h_{21} & h_{22} & \dots & h_{2N} \\
\vdots & \vdots & \ddots & \vdots \\
h_{N1} & h_{N2} & \dots & h_{NN}
\end{pmatrix}.
\tag{4.11}
$$

$$
\Lambda =
\begin{pmatrix}
\lambda_1 \\
\lambda_2 \\
\vdots \\
\lambda_N
\end{pmatrix}.
\tag{4.12}
$$

$$
X =
\begin{pmatrix}
\chi_1 \\
\chi_2 \\
\vdots \\
\chi_N
\end{pmatrix}.
\tag{4.13}
$$

$$h_{ij} = w_1\frac{\displaystyle\int_T D_iD_j d\Omega}{\displaystyle\int_T d\Omega} + w_2\frac{\displaystyle\int_{\bar{T}} D_iD_j d\Omega}{\displaystyle\int_{\bar{T}} d\Omega} + w_3\frac{\displaystyle\int_O D_iD_j d\Omega}{\displaystyle\int_O d\Omega}. \tag{4.14}$$

$$\lambda_i = -2w_1\frac{\displaystyle\int_T D_i d\Omega}{\displaystyle\int_T d\Omega}. \tag{4.15}$$

Since χ_i corresponds to the number of particles delivered to each spot, it must be 0 or a positive value at every spot. Finally, the optimization problem was represented as follows.

$$\text{minimize} \quad f, \text{ with respect to } \chi_i$$
$$\text{subject to } \chi_i \geq 0, \quad \text{for} \quad i = 1, 2, ..., N. \tag{4.16}$$

Strictly speaking, this should be an integer problem because χ_i is the number of particles. However, we treat it as a real number because the number of particles per spot should be typically at the order of 10^4 or more while the requirement of dose accuracy is around 1%, thus a fraction of χ_i less than one is negligible. Since the objective function f is a quadratic form of χ_i as shown in Eq. (4.10), this optimization problem was solved with a quadratic programming approach. We used an interior-point algorithm provided by MATLAB, which is suitable to the convex optimization problem as Eq. (4.16)

4.2.5   Spot layout optimization

Method of single-remotion

Figure 4.5 shows a basic flowchart of the proposed method. In this algorithm, only a single spot is simultaneously removed per iteration. A large number of spots are at first placed densely in each layer of the target as the initial state. Then, the particle number optimization process and the spot removing process are alternately repeated and the number of spots decreases step by step. In the spot removing process, the spot with the smallest number of particles is selected as the first candidate to be removed. After one spot is removed, the

particle number optimization for the remaining spots is performed and the objective function f is evaluated. If f value exceeds the tolerance level f^*, the removed spot is restored and then the next candidate spot is removed.

The algorithm proceeded by the following steps.

Step 1. X is optimized with the initial spot positions and the initial value of the objective function f is calculated. The tolerance level f^* is set. The value k is set to be 1.

Step 2. The spot with the k-th smallest value of X is removed.

Step 3. X is optimized again with the new spot layout and the objective function f is calculated.

Step 4. When $f \leq f^*$, reset $k = 1$ and return to Step 2. When $f > f^*$, the removed spot is restored and k is incremented as $k = k + 1$. Return to Step 2.

Step 5. The iteration is terminated when k exceeds the number of remaining spots.

In this study, the tolerance level f^* of the objective function is set as 1.3 times f value at the initial state. At the initial state spots are located dense enough and the dose distribution is considered to be almost ideal. Therefore, the value 1.3 indicates the level of deterioration from the ideal dose distribution. So this value should be set as small as possible while avoiding an accidental stop of the optimization process caused by a negligible small uplift during the spot elimination steps. We empirically determine this value as 1.3 in which the final dose distribution keeps still acceptable quality enough. Actually, the increase of f value at the near-final steps in the optimization iterations, which is shown later in the section 3.3, and then the termination timing of the optimization process is considered to be less sensitive to the setting of f^*

Method of multiple-remotion

In a three-dimensional case, the number of spots at the initial state and the number of spots to be removed through optimization is expected to be significantly larger compared with a two-dimensional case, and that leads to a long computation time. On the other hand, in typical particle therapy facilities, new patients come almost every day and the staff must
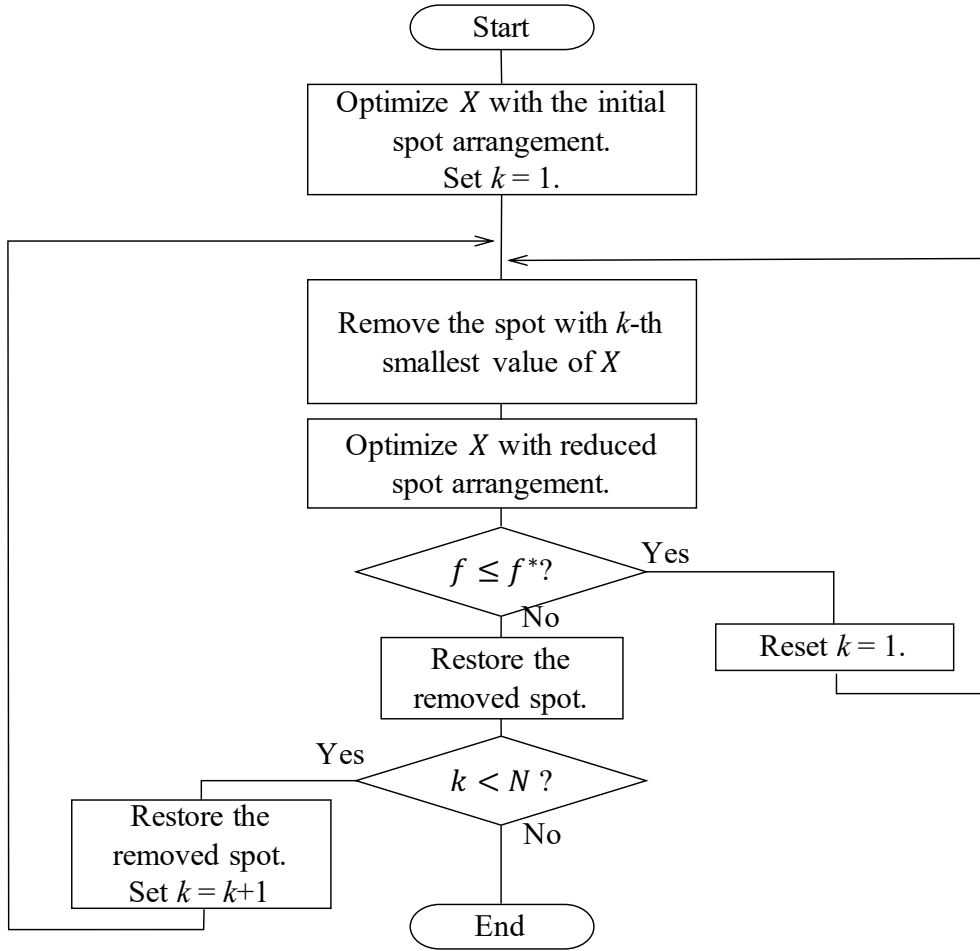
Fig. 4.5 Flowchart of the algorithm with the method of single-remotion.

make patient-specific treatment planning on a daily basis. Therefore, a faster optimization process for the spot layout is desired in particle beam therapy.

In the proposed method, most of the computation time are spent for the process to create the matrix H in Eq. (4.10) and to solve the quadratic problem in Eq. (4.16). Besides, the quadratic problem is repeatedly solved every time the spot is removed. Therefore, reducing the number of steps of spot remotion is very effective to shrink the computation time.

Figure 4.6 shows the flowchart of our proposal for an improved method where multiple spots are simultaneously removed to speed up the optimization process. n_r stands for the number of spots to be removed per iteration. After the optimization of χ_i, the spots with the 1st, 2nd, $\cdots$, n_r-th minimum number of particles are removed and the optimization of χ_i with the remaining spots is carried out again. If f value exceeds f^*, the spot remotion is canceled

and the next spots with the $n_r + 1$-th, $n_r + 2$-th, $\cdots$, $2n_r$-th minimum number of particles are removed, then the process continues similarly. When there is no set of n_r continuous spots to be removed without violating f value, the n_r is decreased to the half value. Here, fractions less than 1 are rounded down. Finally, the optimization process is terminated when $n_r = 1$ and there is no single spot to be removed without violating f value.
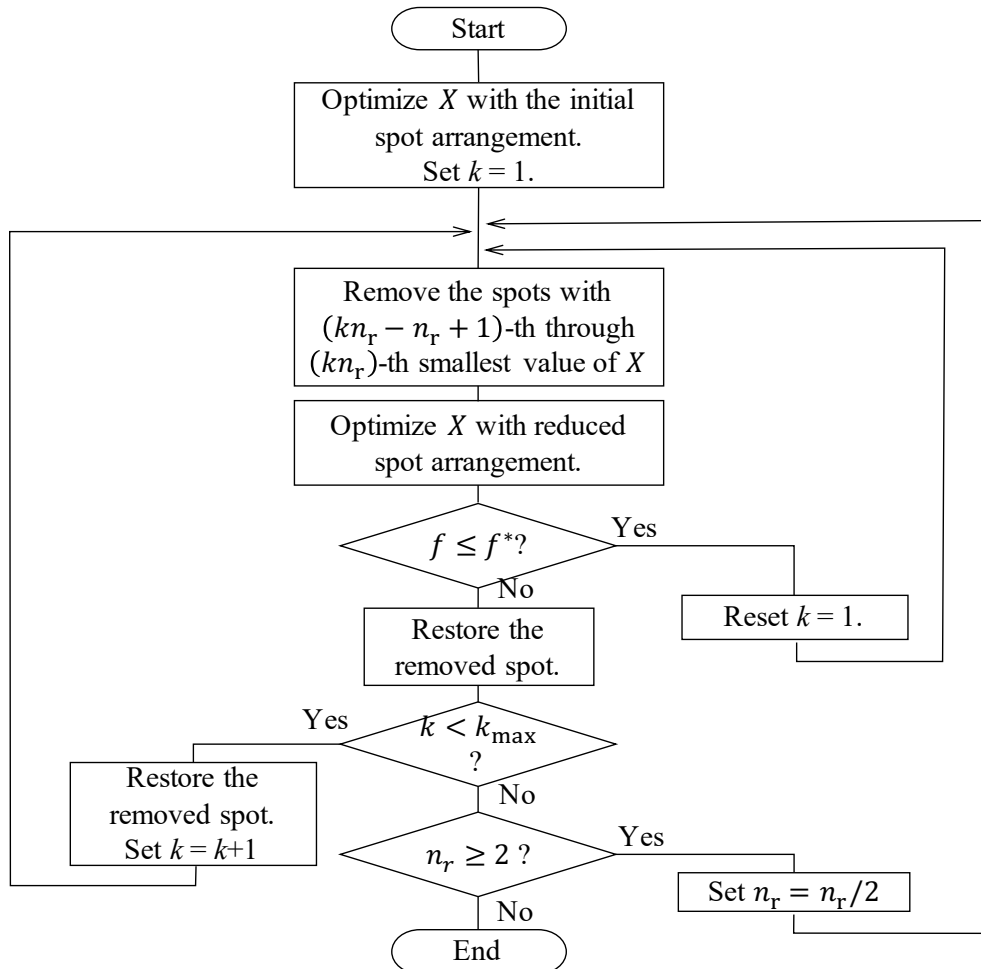

Fig. 4.6 Flowchart of the algorithm with the method of multiple-remotion.

4.2.6 Target geometries and parameter setting

Two-dimensional targets

In order to evaluate the effectiveness of the proposed method, we set several test cases on both two-dimensional and three-dimensional bases. Figure 4.7 shows the test cases for the two-dimensional target: (a) is a square target of 50 mm × 50 mm, (b) is a circular target with a radius of 30 mm, (c) is a concave target where a 30 mm × 30 mm square region is cut out from a 50 mm × 50 mm square, and (d) is a square target of 50 mm × 50 mm with a circular hole with a radius of 15 mm. The beam size σ is set to be 4 mm. The algorithm of single spot remotion, which is shown in Fig. 4.5, is applied to each target. With every target, the optimized spot layout is compared to a lattice pattern with a similar number of spots. No OAR is set in two-dimensional cases.
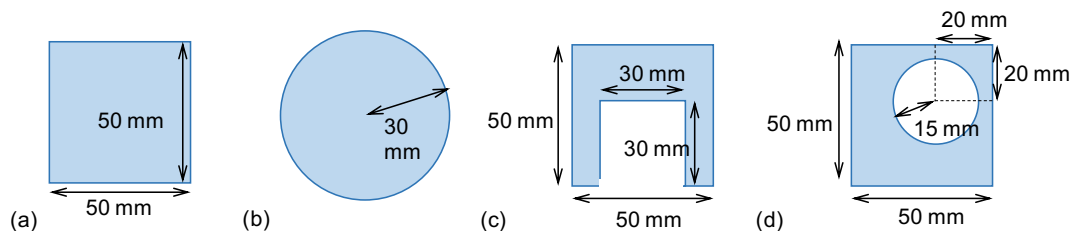
Fig. 4.7 Geometries of the two-dimensional targets with the shapes of (a) square, (b) circle, (c) concave, and (d) square with a hole

Three-dimensonal targets

We also consider a three-dimensional spherical target as shown in Fig. 4.8. In order to test the effectiveness of the proposed algorithm taking advantage of the Bragg-peak of the particle beam in the depth direction, an OAR is placed very close to the target. The target has a spherical shape with the radius of 30 mm and a center depth of 90 mm. A hollow hemisphere-shaped OAR is located as surrounding the half of the target at the opposite side from the beam direction with 8 mm spacing from the target surface. We set this target geometry because of following reasons.

- The spherical shape of the target is one of the typical assumption in particle beam therapy, as shown in the prior research, for example, [30]

- The OAR dose not usually exist at the upstream of the target along the particle beam trajectory, because there is a degree of freedom in deciding the beam irradiation angle and such angles are not selected.

- Filling all the region surrounding the rear half of the target with the OAR should be one of the most difficult setting in sparing the OAR from unnecessary dose.

The setting of parameters

For two-dimensional cases, we set the weighting factors as $w_1 = 0.99$ and $w_2 = 0.01$ in the objective function in Eq. (4.4). For three-dimensional cases, we set $w_1 = 0.950$, $w_2 = 0.003$, and $w_3 = 0.047$. The maximum dose value outside the target is more than half of D_{obj} because of the so-called penumbra structure [92], which is the dose drop around the target edge, with the width of typically around 10 millimeter. On the other hand, the dose fluctuation in the target is less than 10 percent of D_{obj}. Since f_1, f_2 and f_3 have a dimension of square of the dose, f_2 and f_3 often have one or two order larger values in a decimal digit compared with f_1. In order to correct the balance and to put closer order of penalty on each objective function, the value of w_1 should be larger than w_2 and w_3. Besides, in three-dimensional cases, w_3 is set to be larger than w_2 because the OAR dose should be reduced with higher priority than a general volume outside the target. The balance among w_1, w_2 and w_3 can be arranged case by case, considering the importance of the requirements of each corresponding objective function. As the initial state in the spot layout optimization process, the spots are located in the lattice layout with a spacing of 2 mm, which corresponds to 0.5σ, both along the x and y directions in two-dimensional targets and in every layer in three-dimensional targets. The initial spots are located not only inside the target but also outside the target where the distance from the target boundary is within a margin of 1σ. With the three-dimensional target, the depth of layers is set with a spacing of 4 mm. For every cases in two-dimensional and three-dimensional targets, we set $D_{obj} = 1$.
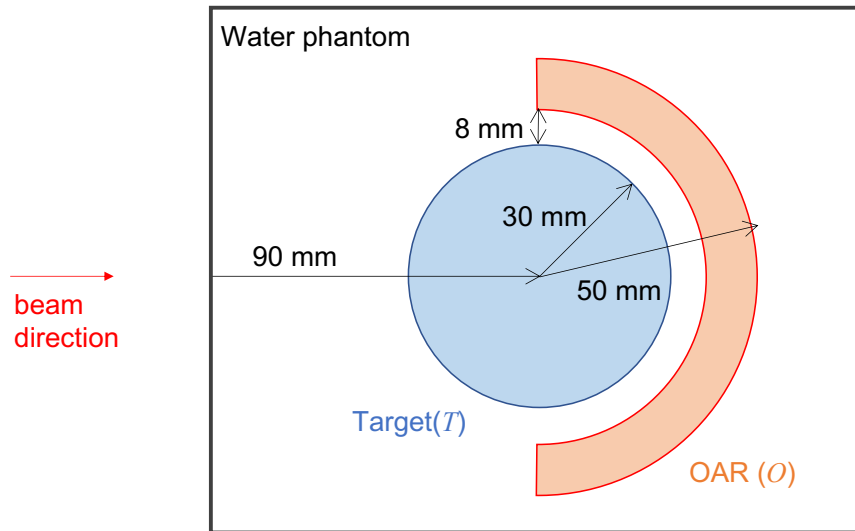
Fig. 4.8 Geometry of the three-dimensional spherical target

4.3   Results and Discussions

4.3.1   Two-dimensional cases

Figure 4.9 shows the initial states of spot locations for two-dimensional targets (a), (b), (c), and (d). Figure 4.10 shows the optimized spot layouts for each target. Here, the blue small circles and red solid lines stand for the spot locations and the target contours, respectively. The numbers of spots at the optimized solutions were 76, 84, 54, and 55 for the targets (a), (b), (c), and (d), respectively. On the other hand, we also tested the lattice spot patterns which have a similar number of spots to the optimized ones as shown in Fig. 4.11. In the optimized spot layouts, more spots were located on the contour of the target, compared with those in the lattice layout. Figure 4.12 shows the dose distribution with the optimized spot layouts and Fig. 4.13 shows the dose distribution with the lattice spot layouts for targets (a), (b), (c), and (d). A similar dose distribution which matches the target contour was confirmed for each shape of target. Table 4.1 shows the comparison of the number of spots and values of the objective function between the optimized spot layout and the lattice spot layout with each target. With every target, the total objective function f with the optimized spot layout was smaller than that with the lattice spot layout. With targets (a) and (b), the objective function f_1, which corresponds to the dose uniformity in the target, with the optimized spot layout was larger than that with the lattice spot layout, while the objective function f_2, which corresponds to the unnecessary dose outside the target, with the optimized spot layout was smaller than

that with the lattice spot layout, With targets (c) and (d), on the other hand, both f_1 and f_2 with the optimized spot layout were smaller than those with the lattice spot layout. We can conclude that the proposed method is effective especially in reducing the unnecessary dose outside the target by adjusting the spot locations close to the target contour. Furthermore, these results imply that the proposed method is also effective in forming homogeneous dose distribution in the target when the target contour shape is complicated, as in targets (c) and (d).

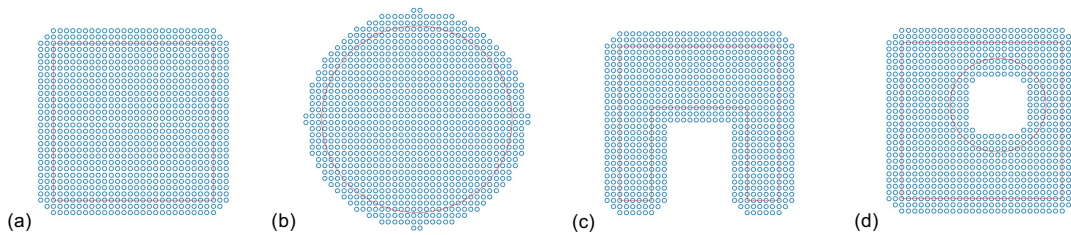Fig. 4.9 Initial state of spot locations with two-dimensional targets.
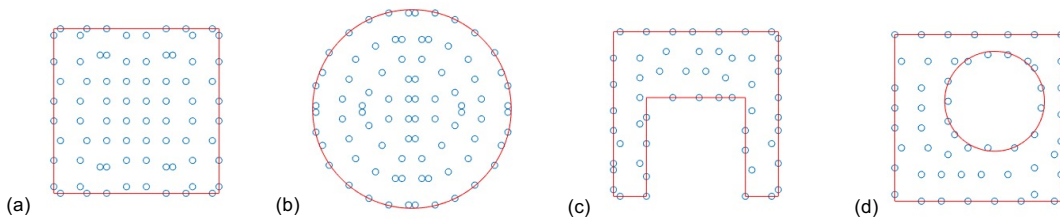
Fig. 4.10 Optimized spot layout with two-dimensional targets.
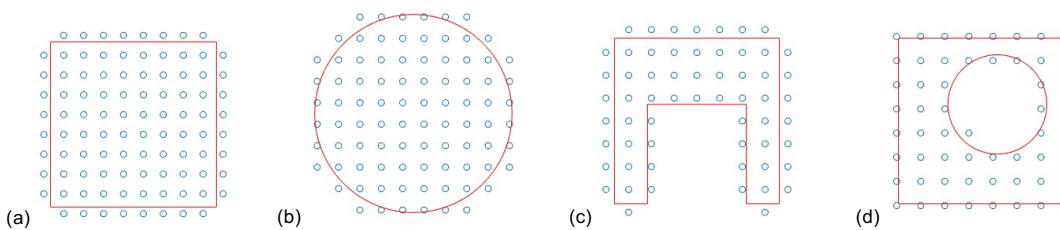
Fig. 4.11 Lattice spot layout with two-dimensional targets.

4.3.2   Three-dimensional case

Figures 4.14 (a) and (b) show the optimized spot layouts with the proposed method of single-remotion and that with the method of multiple-remotion, respectively. With the method of
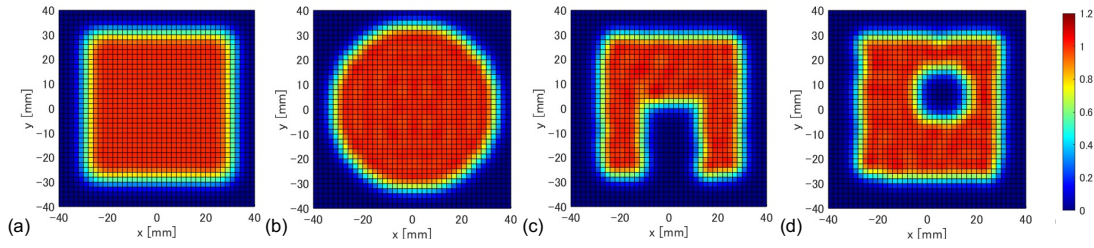
Fig. 4.12 Dose distribution for the optimized spot layout with two-dimensional targets.
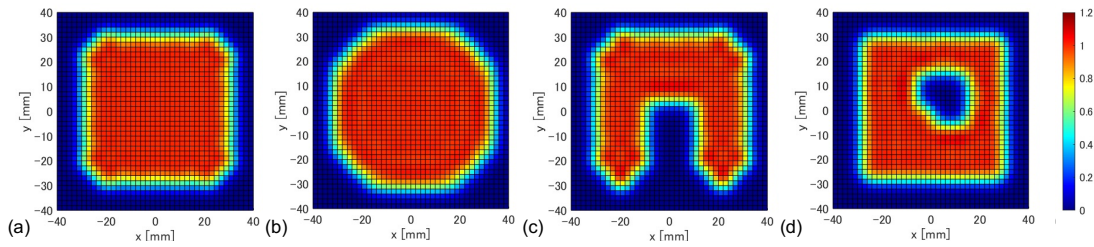
Fig. 4.13 Dose distribution for the lattice spot layout with two-dimensional targets.

Table 4.1 Number of spots and value of the objective functions with optimized and lattice spot layouts for the two-dimensional targets.

Target	Spot layout	Number of spots	f $(\times 10^{-3})$	f_1 $(\times 10^{-4})$	f_2 $(\times 10^{-2})$
(a)	Optimized	76	0.93	3.49	5.88
	Lattice	96	1.03	0.97	9.36
(b)	Optimized	84	0.95	2.93	6.57
	Lattice	88	1.04	2.12	8.12
(c)	Optimized	54	1.20	4.02	8.04
	Lattice	60	1.64	4.91	11.5
(d)	Optimized	55	1.33	4.24	9.11
	Lattice	56	1.52	5.34	9.95

multiple-remotion, the initial value of n_r, the number of spots to be simultaneously removed per iteration, was set to be 5. On the other hand, Fig. 4.14 (c) shows the lattice spot layout where the spot spacing was adjusted so that the number of spots became similar to those in the optimized layouts. The numbers of spots were 652, 688, and 724 in the spot layouts which were optimized with the methods of single-remotion, multiple-remotion and the lattice layout, respectively. In both optimized spot layouts in Figs. 4.14 (a) and (b), many spots were located on the contour of the target in each layer, similar to the two-dimensional results shown in Fig. 4.10. Figures 4.15 (a) and (b) show the dose distributions in the xz cross-sectional plane

with the optimized spot layout for the methods of single-remotion and multiple-remotion, respectively. Here, the white dashed lines show the target contours. On the other hand, Fig. 4.15 (c) shows the dose distribution with the lattice spot layout. The envelope of the dose distribution around the target edge shows mismatches to the circular shaped contour, while the dose distribution with the optimized spot layout shows a smoother dose distribution conformal to the target as in Figs. 4.15 (a) and (b). Table 4.2 shows the comparison of the number of spots and values of the objective function among the optimized spot layouts and the lattice spot layout. Each of the objective functions f, f_1, f_2, and f_3 shows quite similar values in both optimized spot layouts. The objective function f with both optimized spot layouts was reduced to almost half of that with the lattice spot layout. Both f_1 and f_3, which correspond to the dose uniformity in the target and the unnecessary dose to the OAR behind the target, respectively, were smaller with the optimized spot layouts compared to those with the lattice spot layout. The second term f_2, which corresponds to the unnecessary dose outside the target, was almost the same value in every spot layout. This is because the largest contribution to f_2 is the dose in the front region of the target, which is the upstream of the beam trajectory and inevitable to be irradiated regardless of the spot layout. From this result, we consider that the proposed method is effective especially in avoiding an unnecessary dose to the OAR near the target while keeping the dose homogeneity within the target.

Table 4.2 Number of spots and value of objective functions with optimized and lattice spot layouts for the three-dimensional target.

Spot layout	Number of spots	f $(\times 10^{-4})$	f_1 $(\times 10^{-4})$	f_2 $(\times 10^{-2})$	f_3 $(\times 10^{-3})$
Optimized (single-remotion)	688	4.64	1.54	9.55	0.66
Optimized (multiple-remotion)	652	4.64	1.51	9.61	0.67
Lattice	724	9.01	5.76	9.51	1.45

4.3.3   Effectiveness of multiple-remotion method

Figure 4.16 shows the history of changes in the objective function f through iterations with each method of single-remotion and multiple-remotion. With the method of multiple-remotion, the cases in which the initial n_r values were 5, 10, 20, 40 were compared. The horizontal axis is the total number of removed spots from the initial state through the optimization process. With every case, f value was almost unchanged at the beginning of the

Fig. 4.14 Spot locations in each layer with (a) optimized spot layout with the method of single-remotion, (b) optimized spot layout with the method of multiple-remotion, and (c) lattice spot layout with the three-dimensional target.

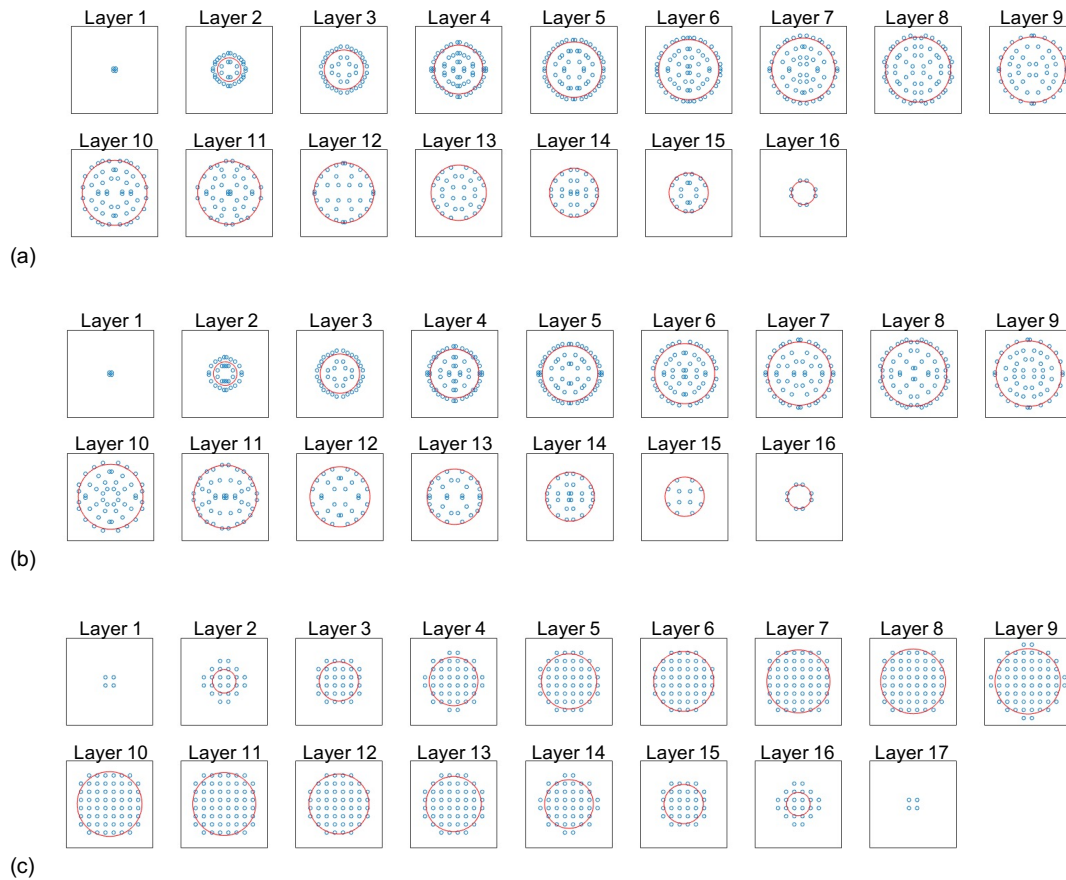Fig. 4.15 Dose distribution at the *xz* cross-sectional plane with (a) optimized spot layout with the method of single-remotion, (b) optimized spot layout with the method of multiple-remotion, and (c) lattice spot layout with the three-dimensional target.
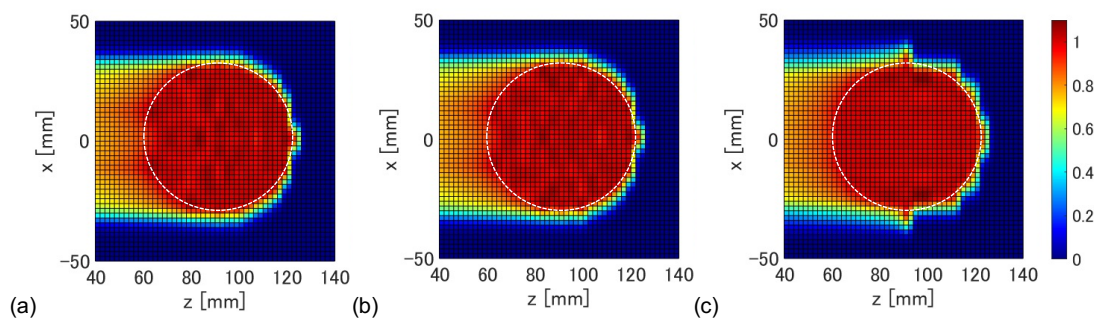
optimization process and suddenly increased toward the end of the optimization process. That is because the spots removed at the early phase in the process have very small contributions,

while every spot has a certain contribution to form the acceptable dose distribution at the
final phase. With the cases of multiple-remotion with $n_r = 5$ and $n_r = 10$, the increase of
f came at similar timings to that of single-remotion. On the other hand, with the cases
of multiple-remotion with $n_r = 20$ and $n_r = 40$, the increase of f came at earlier timings
than that of single-remotion and also multiple-remotion with $n_r = 5$ and $n_r = 10$. Table 4.3
summarizes the comparison of the initial/final values of the number of spot and the objective
function f, and the total computation time. Through this study, we used a Windows computer
with Intel Core-i5 1145G7 CPU (2.6GHz) and 16GB RAM. It is shown that larger value of
n_r could make computation time much shorter, therefore, there is a trade-off between the
solution quality and the computation time in the setting of n_r value. For our problem setting
of the three-dimensional target, we consider it is appropriate to set n_r value around 5 to 10,
because it can accelerate the optimization process without any significant deterioration in the
quality of obtained spot layout.
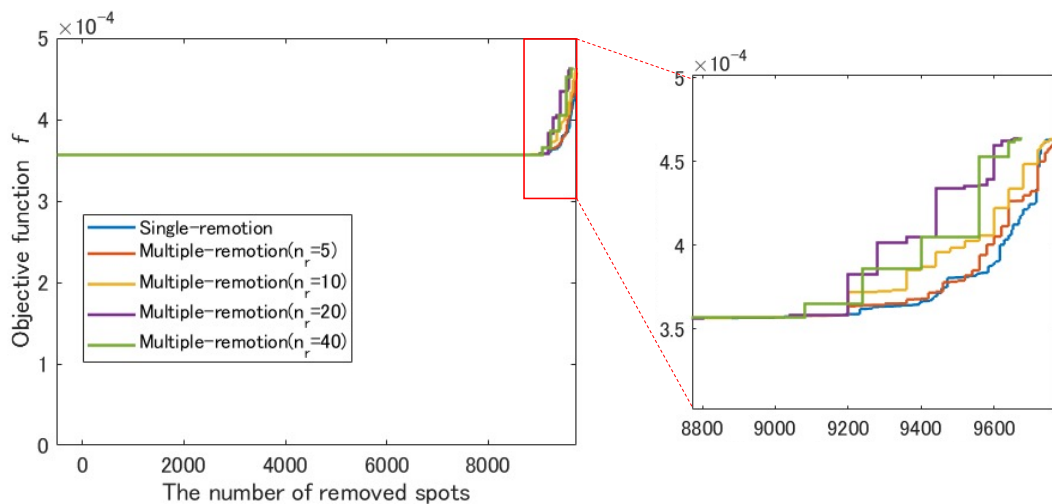
Fig. 4.16 Changes in the objective function f in the optimization processes with the method
of single-remotion, the method of multiple-remotion. The right side figure shows the enlarged
view.

4.3.4   Initial state dependence

The computation time of the optimization process depends not only on n_r values but also on
the number of spots at the initial state. In order to clarify this dependency, the computation
time and the objective function was investigated by varying the spot spacing of the initial
lattice from 1.6 mm to 6.0 mm along both x and y direction. Figure 4.17 (a) shows the

Table 4.3 The number of spots and the objective function at the initial and the final state, and the computation time, with single-remotion and multiple-remotion methods with initial n_r value of 5, 10, 20 and 40.

Initial value of n_r	Initial number of spots	Initial value o of f ($\times 10^{-4}$)	Final number of spots	Final value of f ($\times 10^{-4}$)	Computation time [sec]
1	11128	3.57	688	4.64	36073
5	11128	3.57	652	4.64	7461
10	11128	3.57	684	4.64	3697
20	11128	3.57	776	4.64	2094
40	11128	3.57	772	4.64	1078

relationship between the f values and the number of spots at the initial spots depending on the initial spot spacing. Larger value of the initial spot spacing leaded to larger value of f and smaller number of spots. Changes in the objective function f through the optimization processes are shown in Fig. 4.17 (b). The horizontal axis is the total number of remained spots at each step. For all of the cases, the method of multiple-remotion were applied and the initial n_r were set to be 10. Table 4.4 shows the summary of the initial and the final values of the number of spots and the objective function f, and the total computation time. There was a trend that larger value of the initial spot spacing resulted in larger value of f not only at the initial state but also at the final state. The final number of spots were similar values around 700 for all the cases while there was a small fluctuation depending on the initial spot spacing. Regarding f at the final state, the cases with the initial spot spacing of 1.6 mm, 2.0 mm, 2.4 mm, 3.0 mm, 4.0mm reached similar values. On the other hand, the final f values with the initial spot spacing of 5.0 mm and 6.0 mm were apparently larger than those with 1.6-4.0 mm. The computation time was obviously shorter when the initial spot spacing was larger. From these results, we conclude that the initial spot spacing can be determined by considering the trade-off between the computation time and the objective value, but it should be at most 4.0 mm which corresponds to just the same value to the beam spot size σ.

4.4   Conclusion

In this chapter, we proposed an optimization method for the spot position layout to determine the scanning magnet operation in particle therapy. We achieved the following:

(a)

(b)
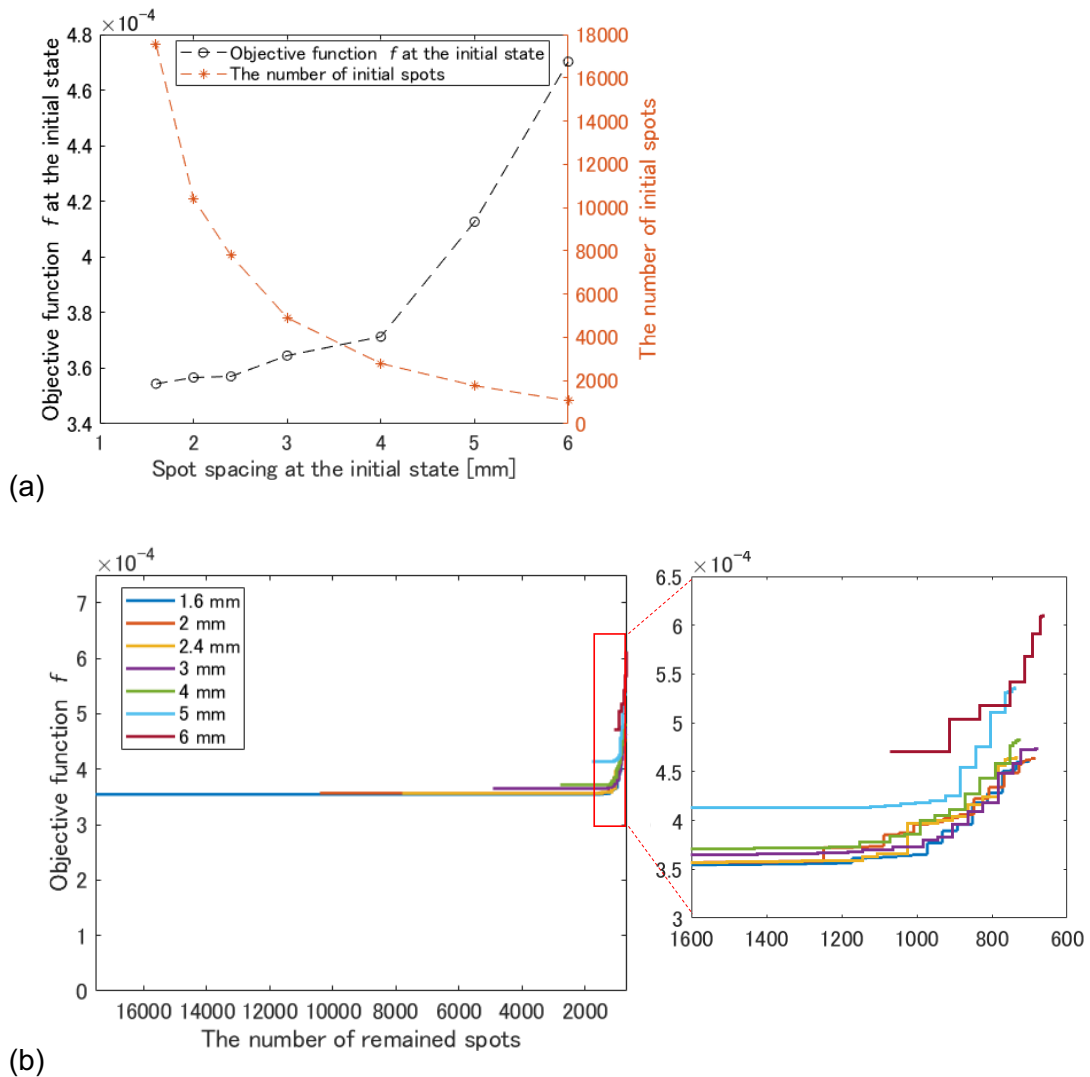
Fig. 4.17 (a) The objective function f and the number of spots at the initial state depending on the initial spot spacing. (b) Changes in the objective function f in the optimization processes with various values of the initial spot spacing, with the method of multiple-remotion with $n_r = 10$. The right side figure shows the enlarged view.

1. We formulated the objective function to evaluate the spot layout and the dose distribution considering the dose homogeneity within the target and the dose reduction outside the target.

2. The spot layout optimization algorithm was constructed, where the spots were densely located at the initial state and removed step by step through iterations based on the contribution of each spot.

Table 4.4 The number of spots and the objective function at the initial and the final state, and the computation time, among various initial state settings. For all the cases initial value of n_r were 10.

Initial spot spacing [mm]	Initial number of spots	Initial value of f $(\times 10^{-4})$	Final number of spots	Final value of f $(\times 10^{-4})$	Computation time [sec]
1.6	17572	3.54	700	4.61	12564
2.0	11128	3.57	684	4.64	3697
2.4	7824	3.57	732	4.64	1413
3.0	4904	3.65	676	4.73	402
4.0	2832	3.71	724	4.83	162
5.0	2832	4.13	736	5.36	110
6.0	2832	4.70	664	6.11	93

3. The algorithm was confirmed and the effectiveness was shown by examples of the two-dimensional and three-dimensional targets. With the optimized spot layout, the objective functions showed better values than those with the conventional lattice spot layout with similar numbers of spots. We also found that many spots were located on the contour of the target with the optimized spot layout.

4. Furthermore, we confirmed the method of multiple-remotion could effectively accelerate the optimization process with very small degradation in the dose quality in the solution.

Chapter 5

Summary

This dissertation has focused on optimization methods which were proposed to reduce the size of the particle therapy system and to provide more effective cancer therapy for patients. With each study of charged particle accelerators and beam irradiation systems, the spatial distribution of physical quantities such as magnetic field or beam dose distribution was formulated and the optimization methodology was constructed, considering the requirement for therapy system. Main findings in the obtained results are as follows:

In Chapter 1, the issues in particle therapy systems and the proposal approaches to them were introduced and the purpose of this research was addressed.

In Chapter 2, a topology optimization method of superconducting coil for compact size synchrotron accelerators and rotational gantries was constructed. In the proposed method, filtering based on Helmholtz type partial differential equation and the projection based on Heaviside function were applied to the density function. In the numerical example, cross-sectional shapes of the coils, which fulfill all the requirements for accelerator coils, were obtained.

In Chapter 3, a robust optimization method for layer stacking irradiation was reported. In the proposed method, the upper limits of the beam amount to each layer was introduced and combinations if the limit setting were searched. The best limit setting was selected based on the robustness evaluation using standard deviation of the depth dose distribution assuming Gaussian probability of the layer position error. Finally, the effectiveness of the developed algorithm was shown through the one-dimensional and three-dimensional numerical simulations using random trials.

In Chapter 4, a layout optimization method of the beam spots in the pencil beam scanning was reported. In the proposed heuristic algorithm, enough large number of spots were

densely located at the initial state and the spot with the smallest contribution to form the dose distribution was removed one by one through iterations. The objective function to determine the spot weights and the error function to judge the removable spot, at each step in algorithm, was formulated. The algorithm was applied to numerical examples with two-dimensional and three-dimensional targets, and good dose distribution was realized with the reduced number of spots.

These results can contribute size reduction of particle therapy equipment and improvement of treatment precision. Combining a compact accelerator with less-invasive beam irradiation will benefit much a larger number of cancer patients. In addition, as future research theme, more practical and combined problems should be addressed: For example, very strong magnetic field generated by superconducting coils may have impacts on hoop stress and critical current density. Therefore, multi-disciplinary design optimization considering those effectiveness is desired. Regarding beam irradiation, beam port angle, i.e. an angular position of the rotational gantry is also a tunable variable as well as beam amount of layer/spot and spot arrangement. Considering beam angle may significantly enlarge the solution space of the optimization problem, and we will need a breakthrough in optimization methodologies.

References

[1] M. Parkin, F. Bray, J. Ferlay, and P. Pisani. Global cancer statistics 2002. *CA Cancer J Clin.*, 55(2):74–108, 2005.

[2] A. Jemal, F. Bray, MM. Center, J. Ferlay, E. Ward, and D. Forman. Global cancer statistics. *CA Cancer J Clin.*, 61(2):69–90, 2011.

[3] C. Fitzmaurice, D. Dicker, A. Pain, H. Hamavid, M. Moradi-Lakeh, MF. MacIntyre, et al. The global burden of cancer 2013. *JAMA Oncol.*, 1(5):690, 2015.

[4] F. Bray, J. Ferlay, I. Soerjomataram, RL. Siegel, LA. Torre, and A. Jemal. Global cancer statistics 2018: Globocan estimates of incidence and mortality worldwide for 36 cancers in 185 countries. *CA Cancer J Clin.*, 68(6):394–424, 2018.

[5] H. Sung, J. Ferlay, RL. Siegel, M. Laversanne, I. Soerjomataram, A. Jemal, and F. Bray. Global cancer statistics 2020: Globocan estimates of incidence and mortality worldwide for 36 cancers in 185 countries. *CA Cancer J Clin.*, 71(3):209–249, 2021.

[6] J. Thariat, J. M. Hannoun-Levi, A. Sun Myint, T. Vuong, and J. P. Gérard. Past, present, and future of radiotherapy for the benefit of patients. *Nat Rev Clin Oncol.*, 10(1):52–60, 2013.

[7] J. S. Loeffler and M. Durante. Charged particle therapy-optimization, challenges and future directions. *Nat. Rev. Clin. Oncol.*, 10:411–424, 2013.

[8] G. Kraft. Tumor therapy with heavy charged particles. *Prog. Part. Nucl. Phys.*, 45:473–544, 2000.

[9] D. Schulz-Ertner, O. Jäkel, and W. Schlegel. Radiation therapy with charged particles. *Seminars in Radiation Oncology*, 16(4):249–259, 2006. Innovative Technologies in Radiation Therapy.

[10] B. Jones and P. Price. Proton therapy: Expanding clinical indications. *Clinical Oncology*, 16:324–325, 2004.

[11] W. T. Chu. Overview of light-ion beam therapy. In *ICRU-IAEA meeting*, 2006.

[12] R. R. wilson. Radiological use of fast protons. *Radiology.*, 47(5):487–491, 1946.

[13] K. Kagawa, M. Murakami, Y. Hishikawa, and M. Abe. Particle therapy practice: sixty year's experience and visions for the next century. *J Jpn Soc Ther Radiol Oncol. (in Japanese)*, 12:205–220, 2000.

[14] Particle Therapy Co-Operative Group. Statistics of patients treated in particle therapy facilities worldwide., 2023. https://www.ptcog.site/index.php/patient-statistics-2.

[15] National Institute for Quantum Science and Technology. QST innovative project., 2023. https://www.qst.go.jp/site/innovative-project-english/quantum-scalpel.html.

[16] K. Noda, T. Furukawa, T. Inaniwa, Y. Iwata, T. Kanai, M. Kanazawa, S. Minohara, K. Mizushima, S. Mori, T. Murakami, N. Saotome, S. Sato, T. Shirai, E. Takada, and Y. Takei. Recent progress on HIMAC for carbon therapy. In *Proceedings PAC09*, 2009.

[17] Z. Jin-Quan, S. Ming-Tao, and W. Bao-Wen. Injection system design for a hadron therapy synchrotron. *Chinese Physics C*, 32(5):393–396, may 2008.

[18] S. Fukumoto, K. Endo, K. Muto, T. Kitagawa, T. Inada, H. Tsujii, Y. Takada, A. Maruhasi, Y. Hayakawa, J. Tada, and S. Sato. Design of a synchrotron for proton therapy. In *Proceedings of the 1989 IEEE Particle Accelerator Conference, . 'Accelerator Science and Technology*, pages 700–702 vol.1, 1989.

[19] G. Arduini, R. Cambria, C. Canzi, F. Gerardi, B. Gottschalk, R. Leone, L. Sangaletti, and M. Silari. Physical specifications of clinical proton beams from a synchrotron. *Med Phys*, 23(6):939–951, 1996.

[20] K. Kleeven and S. Zaremba. Cyclotrons: Magnetic design and beam dynamics. *arXiv:1804.08961v1*, 2018.

[21] H. Takekoshi, S. Matsuki, K. Mashiko, and N. Shikazono. RF structure of superconducting cyclotron for therapy application. *Bull. Inst. Chem. Res., Kyoto Univ.*, 59(1):1–8, 1981.

[22] S. Gotoh. Development status of next-generation high magnetic field superconducting proton therapy systems. *Ionizing radiation*, 39(2):55–57, 2013.

[23] S. Fukumoto. Cyclotron versus synchrotron for proton beam therapy. In *Proceedings of the 14th International Conference on Cyclotrons and their Applications*, pages 534–536, 2004.

[24] Y. Iwata, K. Noda, T. Shirai, T. Fujita, T. Furukawa, K. Mizushima, Y. Hara, Y. Saraya, R. Tansho, S. Matsuba, S. Mori, S. Sato, K. Shoda, T. Fujimoto, H. Arai, T. Ogitsu, N. Amemihya, Y. Nagamoto, T. Orikasa, and S. Takayama. Present status of a superconducting rotating-gantry for carbon therapy. In *Proceedings HIAT2015*, 2015.

[25] Mitsubishi electric develops multi-function irradiation nozzle for proton-type particle therapy systems., 2015. https://www.mitsubishielectric.com/news/2015/0217-b.html.

[26] W. T. Chu, B. A. Ludewigt, and T. R. Renner. Instrumention for treatment of cancer using proton and light-ion beams. *Rev. Sci. Instrum.*, 64(8):2055–2122, 1993.

[27] T. Kanai, M. Endo, S. Minohara, N. Miyahara, Hi. Koyama-ito, H. Tomura, N. Matsufuji, Y. Futami, A. Fukumura, T. Hiraoka, Y. Furusawa, K. Ando, M. Suzuki, F. Soga, and K. Kawachi. Biophysical characteristics of HIMAC clinical irradiation system for heavy-ion radiation therapy. *International Journal of Radiation Oncology*Biology*Physics*, 44(1):201–210, 1999.

[28] A. Brahme. Optimal setting of multileaf collimators in stationary beam radiation therapy. *Strahlenther Onkol.*, 164(6):343–350, 1988.

[29] T. Kanai, K. Kawachi, and H. Matsuzawa. Broad beam three-dimensional irradiation for proton radiotherapy. *Med. Phys.*, 10:344–346, 1983.

[30] Y. Futami, T. Kanai, M. Fujita, H. Tomura, A. Higashi, M. Matsufuji, N. Miyahara, M. Endo, and K. Kawachi. Broad-beam three-dimensional irradiation system for heavy-ion radiotherapy at HIMAC. *Nuclear Instruments and Methods in Physics Research A.*, 430:143–153, 1999.

[31] N. Kanematsu, M. Endo, Y. Futami, and T. Kanai. Treatment planning for the layer-stacking irradiation system for three-dimensional conformal heavy-ion radiotherapy. *Med. Phys.*, 29(12):2823–2829, 2002.

[32] HIMAC NEWS: Development of layer stacking particle therapy system (in japanese). https://www.nirs.qst.go.jp/publication/nirs_news/200210/hik2p.htm.

[33] T. Kanai, K. Kawachi, and Y. Kumamoto. Spot scanning system for proton radiotherapy. *Med Phys.*, 7:365–369, 1980.

[34] M. Krämer, O. Jäkel, T. Haberer, G. Kraft, D. Schardt, and U. Weber. Treatment planning for heavy-ion radiotherapy: physical beam model and dose optimization. *Phys. Med. Biol.*, 45:3299–3317, 2000.

[35] O. Jäkel, M. Krämer, C. P. Karger, and J. Debus. Treatment planning for heavy ion radiotherapy: clinical implementation and application. *Phys Med Biol.*, 46(4):1101–1116, 2001.

[36] B. Marchand, D. Prieels, B. Bauvir, R. Sépulchre, and M. Gérard. IBA proton pencil beam scanning: An innovative solution for cancer treatment. In *Proceedings EPAC2000*, 2000.

[37] C. H. Miao, M. Liu, C. X. Yin, and Z. T. Zhao. Precise magnetic field control of the scanning magnets for the APTRON beam delivery system. *Nuclear Science and Techniques*, 28, 12 2017.

[38] H. Blosser, J. Bailey, R. Burleigh, D. Johnson, E. Kashy, T. Kuo, F. Marti, J. Vincent, A. Zeller, E. Blosser, G. Blosser, R. Maughan, W. Powers, and J. Wagner. Superconducting cyclotron for medical application. *IEEE Transactions on Magnetics*, 25(2):1746–1754, 1989.

[39] H. Blosser, D. Johnson, D. Lawton, F. Marti, R. Ronningen, and J. Vincent. A compact superconducting cyclotron for the production of high intensity protons. In *Proceedings of the 1997 Particle Accelerator Conference (Cat. No.97CH36167)*, volume 1, pages 1054–1056 vol.1, 1997.

[40] K. Koyanagi, S. Takayama, T. Tosaka, K. Tasaki, T. Kurusu, T. Yoshiyuki, N. Amemiya, and T. Ogitsu. Development of saddle-shaped coils using coated conductors for accelerator magnets. *IEEE Transactions on Applied Superconductivity*, 23(3):4100404–4100404, 2013.

[41] K. Koyanagi, S. Takayama, H. Miyazaki, T. Tosaka, K. Tasaki, T. Kurusu, and Y. Ishii. Development of saddle-shaped coils for accelerator magnets wound with YBCO-coated conductors. *IEEE Transactions on Applied Superconductivity*, 25(3):1–4, 2015.

[42] S. Takayama, K. Koyanagi, T. Orikasa, Y. Ishii, T. Kurusu, Y. Iwata, K. Noda, K. Suzuki, T. Ogitsu, Y. Sogabe, and N. Amemiya. Research and development of the coil system for a beam transport and irradiation line (in japansese). *J. Cryo. Super. Soc. Jpn.*, 52(4):234–243, 2017.

[43] Ruirui Liu, Baozhou Sun, Tiezhi Zhang, Jeffery F. Williamson, Joseph A. O'Sullivan, and Tianyu Zhao. Dosimetric impact of range uncertainty in passive scattering proton therapy. *J Appl Clin Med Phys.*, pages 1–9, 2021.

[44] Christoph Bert, Sven O Gr ozinger, and Eike Rietzel. Quantification of interplay effect of scanned particle beams and moving targets. *Phys Med Biol.*, 53:2253–2265, 2008.

[45] A. Olafsson and S. J Wright. Efficient schemes for robust IMRT treatment planning. *Phys Med Biol.*, 51:5621–5642, 2006.

[46] B. Schaffner, T. Kanai, Y. Futami, M. Shimbo, and E. Urakabe. Ridge filter design and optimization for the broad-beam three-dimensional irradiation system for heavy-ion radiotherapy. *Med. Phys.*, 27:716–724, 2000.

[47] J. Kouwenberg, J. Penninkhof, S. Habraken, J. Zindler, M. Hoogeman, and B. Heijmen. Model based patient pre-selection for intensity-modulated proton therapy (IMPT) using automated treatment planning and machine learning. *Radiotherapy and Oncology*, 158:224–229, 5 2021.

[48] C. Bert and E. Rietzel. 4D treatment planning for scanned ion beams. *Rad Oncol.*, 2:24, 2007.

[49] J. H. Kang, J. J. Wilkens, and U. Oelfke. Demonstration of scan path optimization in proton therapy. *Med. Phys.*, 34(9):3457–3464, 2007.

[50] M. F. Dias, M. Riboldi, J. Seco, I. Castelhano, A. Pella, A. Mirandola, L. Peralta, M. Ciocca, R. Orecchia, and G. Baroni. Scan path optimization with/without clustering for active beam delivery in charged particle therapy. *Physica Med.*, 31:130–136, 2015.

[51] C. Wu, Y. H. Pu, and X. Zhang. GPU-accelerated scanning path optimization in particle cancer therapy. *Nucl. Sci. Tech.*, 30:56, 2019.

[52] R. T. Haftka and H. M. Adelman. Selection of actuator locations for static shape control of large space structures by heuristic integer programing. *Comput. Struct.*, 20(1-3):575–582, 1985.

[53] Y. Yamaki, Y. Sato, K. Izui, T. Yamada, S. Nishiwaki, Y. Hirai, and O. Tabata. A heuristic approach for actuator layout designs in deformable mirror devices based on current value optimization. *Struct. Multidiscip. O.*, 58:1243–1254, 2018.

[54] M. P. Bendsøe and N. Kikuchi. Generating optimal topologies in structural design using a homogenization method. *Comput. Methods Appl. Mech.*, 71(2):197–224, 1988.

[55] R. Yang and C. Chuang. Optimal topology design using linear programming. *Computers and Structures*, 52(2):265–275, 1994.

[56] H. Mlejnek and R. Schirrmacher. An engineer's approach to optimal material distribution and shape finding. *Comput. Methods Appl. Mech. Engrg.*, 106(1):1–26, 1993.

[57] T. Yamada, K. Izui, S. Nishiwaki, and A. Takezawa. A topology optimization method based on the level set method incorporating a fictitious interface energy. *Comput. Methods Appl. Mech. Engrg.*, 199(2876-2891), 2010.

[58] M. Otomori, T. Yamada, K. Izui, and S. Nishiwaki. Topology optimization based on the level set method using mathematical programming. *Transactions of the Japan Society of Mechanical Engineers Series C*, 77(787):4001–4014, 2011.

[59] O. Sigmund. Morphology-based black and white filters for topology optimization. *Structural and Multidisciplinary Optimization*, 33(4):401–424, 2007.

[60] M. Wang and S. Wang. Bilateral filtering for structural topology optimization. *nt. J. Numer. Meth. Engng.*, 63(13):1911–1938, 2005.

[61] J. Guest, J. Prévost, and T. Belytschko. Achieving minimum length scale in topology optimization using nodal design variavles and projection functions. *Int. J. Numer. Meth. Engng.*, 61(2):238–254, 2004.

[62] A. Kawamoto, T. Matsumori, S. Yamasaki, T. Nomura, T. Kondoh, and S. Nishiwaki. Heaviside projection based topology optimization by a PDE-filtered scalar function. *Struct Multidisc Optim.*, 44:19–24, 2011.

[63] S. Lim, T. Yamada, S. Min, and S. Nishiwaki. Topology optimization of a magnetic actuator based on level set and phase-field approach. *IEEE Trans. Mag.*, 47:1318–1321, 2014.

[64] Y. Hidaka, T. Sato, and H. Igarashi. Topology optimization method based on on-off method and level set approach. *IEEE Trans. Mag.*, 50:617–620, 2014.

[65] H J Herman. The superconducting magnet system for the ATLAS detector at CERN. *IEEE Transactions on Applied Superconductivity*, 10(1):347–352, 2000.

[66] H. Owen, A. Lomax, and S. Jolly. Current and future accelerator technologies for charged particle therapy. *Nuclear Instruments and Methods in Physics Research Section A: Accelerators, Spectrometers, Detectors and Associated Equipment*, 809:96–104, 2016. Advances in detectors and applications for medicine.

[67] M. Altarelli. Application of synchrotron radiation to semiconductor surfaces, interfaces, and heterostructures. In M. Razeghi, Y.-S. Park, and G. L. Witt, editors, *Optoelectronic Integrated Circuit Materials, Physics, and Devices*, volume 2397, pages 556 – 565. International Society for Optics and Photonics, SPIE, 1995.

[68] H. Okuno, H. Sakurai, Y. Mori, R. Fujita, and M. Kawashima. Proposal of a 1-ampere-class deuteron single-cell linac for nuclear transmutation. *Proceedings of the Japan Academy, Series B*, 95(7):430–439, 2019.

[69] K. Takahashi, N. Amemiya, T. Nakamura, T. Ogitsu, T. Kurusu, T. Yoshiyuki, K. Noda, and S. Awaji. Magnetic field design of dipole magnet wound with coated conductor considering its current transport characteristics. *IEEE Trans. Appl. Supercond. (in Japanese)*, 21:1833–1837, 2011.

[70] S. Yamamoto, K. Konii, H. Tanabe, S. Yokoyama, and T. Matsuda. Design and manufacturing of superconducting magnets for magnetic resonance imaging system. In *Proceedings of ICEC 24 and ICMC 2012*, 2012.

[71] B. Parker and J. Escallier. Serpentime coil topology for BNL direct wind superconducting magnets. In *Proceedings of PAC2005*, 2015.

[72] S. Mizutao, N. Amemiya, T. Ogitsu, T. Orihara, T. Kurusu, T. Obana, and K. Noda. Measurement of magnetic field harmonics of superconducting coil wound by surface winding method. In *Proceedings of 84th CSSJ Conference*, 2011.

[73] Q. Wang, G. Xu, Y. Dai, B. Zhao, L. Yan, and K. Kim. Design of open high magnetic field MRI superconducting magnet with continuous current and genetic algorithm method. *IEEE Trans. Appl. Supercond.*, 19:2289–2292, 2009.

[74] S. Noguchi, H. Yamashita, and A. Ishiyama. An optimization method for design of SMES coils using YBCO tape. *IEEE Trans. Appl. Supercond.*, 13:1856–1859, 2003.

[75] K. Svanberg. The method of moving asymptote - a new method for structural optimization. *Int. J. Numer. Meth. Engng.*, 24:359–373, 1987.

[76] Electrotechnical Laboratory. *Researches of the Electrotechnical Laboratory (in Japanese)*. Densoken, 1972.

[77] E. Pedroni R. Bacher, H. Blattmann, T. Böhringer, A. Coray, A. Lomax, S. Lin, G. Munkel, S. Scheib, and U. Schneider. The 200-MeV proton therapy project at the paul scherrer institute: conceptual design and practical realization. *Med. Phys.*, 22(1):37–53, 1995.

[78] S. Mori, J. Wolfgang, H. Lu, R. Schneider, N. C. Choi, and G. T. Y. Chen. Quantitative assessment of range fluctuations in charged particle lung irradiation. *International Journal of Radiation Oncology, Biology, Physics*, 70(1):253–261, 2008.

[79] T. Inaniwa, N. Kanematsu, T. Furukawa, and K. Noda. Optimization algorithm for overlapping-field plans of scanned ion beam therapy with reduced sensitivity to range and setup uncertainties. *Phys. Med. Biol.*, 56:1653–1669, 2011.

[80] T. Akagi, T. Aso, G. Iwai, A. Kimura, S. Kameoka, B. S. Lee, Y. Maeda, N. Matsufuji, T. Nishio, C. Omachi, S. Park, T. Sasaki, T. Toshito, W. Takase, T. Yamashita, and Y. Watase. Geant4-based particle therapy simulation framework for verification of dose distributions in proton therapy facilities. *Progress in Nuclear Science and Technology*, 4:896–900, 2014.

[81] S. M. Zenklusen, E. Pedroni, and D. Meer. Study on repainting strategies for treating moderately moving targets with proton pencil beam scanning at the new gantry 2 at PSI. *Phys. Med. Biol.*, 55:5103–5121, 2010.

[82] T. Inaniwa, N. Kanematsu, T. Furukawa, and A. Hasegawa. A robust algorithm of intensity modulated proton therapy for critical tissue sparing and target coverage. *Phys. Med. Biol.*, 56:4749–4770, 2011.

[83] T. Kanai, K. Kawachi, H. Matsuzawa, and T. Inada. Three-dimensional beam scanning for proton therapy. *Three-dimensional beam scanning for proton therapy.*, 214:491–496, 1983.

[84] G. Meier, D. Leiser, R. Besson, A. Mayor, S. Safai, D. C. Weber, and A. J. Lomax. Contour scanning for penumbra improvement in pencil beam scanned proton therapy. *Phys. Med. Biol.*, 62(6):2398–2416, 2017.

[85] C. Winterhalter, G. Meier, D. Oxley, D. C. Weber, A. J. Lomax, , and S. Safai. Contour scanning, multi-leaf collimation and the combination thereof for proton pencil beam scanning. *Phys. Med. Biol.*, 64(1):015002, 2019.

[86] H. Fukushima, Y. Kamada, and I. Hagiwara. Optimum engine mounting layout using MPOD. *Transactions of the Japan Society of Mechanical Engineers Series C (in Japanese).*, 70:54–61, 2004.

[87] Y. Nishiura, K. Hirata, K. Ohya, Y. Sakaidani, and N. Niguchi. Optimization of the stator pole arrangement of 3-degree of freedom spherical actuator using genetic algorithm. *Journal of the Japan Society of Applied Electromagnetics and Mechanics (in Japanese).*, 23(2):332–337, 2015.

[88] Y. Nishiura, K. Hirata, and K. Ohya. Optimization of the stator pole arrangement for 3-DOF spherical actuator using genetic algorithm. In *IEEE International Magnetics Conference (INTERMAG)*, page 1, 2015.

[89] Y. Matsumoto, K. Tanaka, and M. Nakamura. Placement optimization of solar arrays in photovoltaic power generation facility site. *Transactions of the Japan Society of Mechanical Engineers (in Japanese)*, 87:899, 2021.

[90] S. van de Water, H.M. Kooy, B.J.M. Heijmen, and M.S. Hoogeman. Shortening delivery times of intensity modulated proton therapy by reducing proton energy layers during treatment plan optimization. *Int. J. Radiation Oncol. Biol. Phys.*, 92(2):460–468, 2015.

[91] T. Akagi, T. Aso, B. Faddegon, A. Kimura, N. Matsufuji, T. Nishio, C. Omachi, H. Paganetti, J. Perl, T. Sasaki, D. Sawkey, J. Schümann, J. Shin, T. Toshito, T. Yamashita, and H. Yoshida. The PTSim and TOPAS projects, bringing Geant4 to the particle therapy clinic, 2011.

[92] S. Myers, A. Degiovanni, and J. B. Farr. Future prospects for particle therapy accelerators. *Reviews of Accelerator Science and Technology*, 10(1):49–92, 2019.

List of Publications

Journal Papers

[1] Yusuke Sakamoto, Daisuke Ishizuka, Tetsuya Matsuda, Kazuhiro Izui, Shinji Nishiwaki. Topology optimization of superconducting electromagnets for particle accelerators. (in Japanese) *IEEJ Journal of Industry Applications*, Vol. 139, No. 9, 2019, pp.568-575.

[2] Yusuke Sakamoto, Yoshikazu Maeda, Yukiko Yamada, Masahiro Ikeda, Yuji Tameshige, Makoto Sasaki, Satoshi Shibata, Kazutaka Yamamoto. A robust optimization method for weighted-layer-stacking proton beam therapy. *Physics in Medicine and Biology*, Vol. 65, No. 19, 2020, Page No. 195009.

[3] Yusuke Sakamoto, Takayuki Nagashima, Yuki Sato, Kazuhiro Izui, Shinji Nishiwaki. Layout optimization of the beam spot locations scanned by electromagnets in particle beam therapy. *Mechanical Engineering Journal,* Vol. 9, No. 5, 2022, Page No. 22–00140.

Refereed International Proceedings

[1] AKM Khaled Ahsan Talukder, Bingnan Wang, Yusuke Sakamoto. Electric Machine Two-dimensional Flux Map Prediction with Ensemble Learning. *International Conference on Electrical Machines and Systems (ICEMS),* 2022, pp. 1-4, Chiang Mai, Thailand.

[2] Bingnan Wang, AKM Khaled Ahsan Talukder, Yusuke Sakamoto. Topological Data Analysis for Image-based Machine Learning: Application to Electric Motors. *IEEE International Conference on Electrical Machines (ICEM),* 2022, pp. 1015-1021, Valencia, Spain.

[3] Yihao Xu, Bingnan Wang, Yusuke Sakamoto, Tatsuya Yamamoto, Yuki Nishimura, Toshiaki Koike-Akino, Ye Wang. Tandem Neural Networks for Electric Machine Inverse Design. *IEEE International Electric Machines and Drives Conference (IEMDC),* 2023, pp. 1-7, San Francisco, CA, USA

[4] Yusuke Sakamoto, Yihao Xu, Bingnan Wang, Tatsuya Yamamoto, Yuki Nishimura. Multi-Objective Motor Design Optimization with Physics-Assisted Neural Network Model. *IEEE International Electric Machines and Drives Conference (IEMDC),* 2023, pp. 1-7, San Francisco, CA, USA.

[5] Yihao Xu, Bingnan Wang, Yusuke Sakamoto, Tatsuya Yamamoto, Yuki Nishimura. Comparison of Learning-based Surrogate Models for Electric Motors. *Conference on the Computation of Electromagnetic Fields (COMPUMAG),* 2023, Kyoto, Japan.

[6] Yusuke Sakamoto, Yihao Xu, Bingnan Wang, Tatsuya Yamamoto, Yuki Nishimura. Electric Motor Surrogate Model Combining Subdomain Method and Neural Network,. *Conference on the Computation of Electromagnetic Fields (COMPUMAG),* 2023, Kyoto, Japan.

Non Refereed International Proceedings

[1] Yusuke Sakamoto, Yuehu Pu, Yoshikazu Maeda, Yukiko Yamada, Masahiro Ikeda, Yuji Tameshige, Makoto Sasaki, Kazutaka Yamamoto. "A Robust Algorithm of Weight Optimization in Layer Stacking Proton Beam Therapy. *52nd Annual Conference of Particle Therapy Co-operative Group (PTCOG52),* 2013, Essen, Germany

[2] Nobuyuki Haruna, Yusuke Sakamoto, Tadashi Katayose, Nobuhiro Shigyo and Yukinobu Watanabe. Shielding Design for a Compact Proton Therapy Facility. *52nd Annual Conference of Particle Therapy Co-operative Group (PTCOG52),* 2013, Essen, Germany

[3] Yusuke Sakamoto, Hiroaki Kumada, Toshiyuki Terunuma, Taizo Honda and Takeji Sakae. A simulation study for rapid raster scanning proton irradiation on moving target. *53rd Annual Conference of Particle Therapy Co-operative Group (PTCOG53),* 2014, Shanghai, China

[4] Yusuke Sakamoto, Hisashi Harada, Taizo Honda, Masahiro Ikeda, Yukiko Yamada, Takashi Akagi. Evaluation of penumbra improvement by using multi-leaf collimators in proton beam scanning. *55th Annual Conference of Particle Therapy Co-operative Group (PTCOG55),* 2016, Prague, Czech Republic.

Domestic Conferences

[1] 坂本裕介, 蒲越虎, 前田嘉一, 山田由希子, 池田昌広, 為重雄司, 佐々木誠, 山本和高. 積層原体照射のロバストウェイト最適化第106回日本医学物理学会学術大会, 2013, 大阪, 日本.

[2] 坂本裕介, 熊田博明, 照沼利之, 蒲越虎, 本田泰三, 榮武二. 高速ラスタースキャニング法による呼吸同期照射シミュレーション. 第107回日本医学物理学会学術大会, 2014, 横浜, 日本.

[3] 坂本 裕介, 石塚大介, 松田哲也, 泉井一浩, 西脇眞二. 粒子線加速器コイルのトポロジー最適化. 第13回最適化シンポジウム（OPTIS）, 2018, 京都, 日本.

[4] 山内一輝, 野村航大, 松田哲也, 坂本裕介, 井上啓, 殿岡俊, 佐藤伸治, 井手太星, 藤原康暉, 一柳優子. 磁気粒子イメージングの原理検証装置の開発. 第 42 回日本磁気学会学術講演会, 2018, 東京, 日本.

[5] 中村雄一朗, 坂本裕介, 十時詠吾, 山口信一. 永久磁石モータの 2 段ダミースロット構造に対する磁気回路モデルの検討. 2021 年電気学会全国大会, 2021, オンライン.